NOTE TO USERS

This reproduction is the best copy available.

uOttawa

L'Université canadienne
Canada's university

FACULTÉ DES ÉTUDES SUPÉRIEURES ET POSTOCTORALES

uOttawa

L'Université canadienne
Canada's university

FACULTY OF GRADUATE AND POSDOCTORAL STUDIES

Xiangjun Meng

AUTEUR DE LA THÈSE / AUTHOR OF THESIS

M.A.Sc. (Electrical Engineering)

GRADE / DEGREE

School of Information Technology and Engineering

FACULTÉ, ÉCOLE, DÉPARTEMENT / FACULTY, SCHOOL, DEPARTMENT

A Synthesis Technique for Radial Line Slot Array Antennas with Isoflux Radiation Patterns

TITRE DE LA THÈSE / TITLE OF THESIS

Derek McNamara

DIRECTEUR (DIRECTRICE) DE LA THÈSE / THESIS SUPERVISOR

CO-DIRECTEUR (CO-DIRECTRICE) DE LA THÈSE / THESIS CO-SUPERVISOR

EXAMINATEURS (EXAMINATRICES) DE LA THÈSE / THESIS EXAMINERS

Mustapha Yagoub

Aldo Petosa

Gary W. Slater

Le Doyen de la Faculté des études supérieures et postdoctorales / Dean of the Faculty of Graduate and Postdoctoral Studies

A Synthesis Technique for Radial Line Slot Array Antennas with Isoflux Radiation Patterns

by

Xiangjun Meng

A thesis submitted to the
Faculty of Graduate and Postdoctoral Studies
in partial fulfillment of the requirements for the degree of

Master of Applied Science
in Electrical Engineering

Ottawa-Carleton Institute for Electrical and Computer engineering
School of Information Technology and Engineering
Faculty of Engineering
University of Ottawa

May 2009

Your file Votre référence
ISBN: 978-0-494-61193-7
Our file Notre référence
ISBN: 978-0-494-61193-7

ABSTRACT

In this thesis the possibility of using radial line slot array (RLSA) antennas to provide low profile isoflux radiation patterns suitable for use as circularly-polarized tracking, telemetry & command (TT&C) antennas on low Earth orbit (LEO) satellites is investigated. The RLSA antenna elements are slot pairs located on concentric circles on the top plate of a radial waveguide. Conventional synthesis techniques cannot be used due to the fact that the RLSA antenna is a non-uniformly spaced array, the elements do not all have the same orientation, and the excitation amplitudes and phases are linked to the actual physical location of a particular slot pair. A technique is therefore developed for synthesizing such an RLSA antenna.

Keywords: Antennas, Radial Line Slot Antennas, Isoflux Radiation Patterns

ACKNOWLEDGEMENTS

I would like to thank my supervisor Dr. Derek McNamara for his support, guidance and funding during the research and writing of this thesis. I would also like to thank Dr. Pierre Berini for providing partial financial support during the early stages of my studies.

I also owe thanks to my graduate student colleagues Ms. Xiaowen Liu, Mr. Wei Fang, Mr. Liguo Yang, and Mr. Pradiv Sooriyadevan. Most of all I thank my husband and family members and friends for always being there for me, and for unselfishly supporting me from the very beginning of my graduate studies.

TABLE OF CONTENTS

GLOSSARY

Antenna Array: An assembly of radiating elements in an electrical and geometrical configuration is referred to as an array. The total field of the array is determined by the vector addition of the fields radiated by the individual elements.

Antenna Pattern: A mathematical function or a graphical representation of the radiation properties of the antenna as a function of space coordinates, in most case, the radiation pattern is determined in the far-field region and is represented as a function of the directional coordinates.

Antenna Pattern Synthesis: A method of design that is to find the antenna configuration, geometrical dimensions and its excitation distribution for desired radiation characteristics.

Directivity: the ratio of the radiation intensity in a given direction from the antenna to the radiation intensity averaged over all directions.

Earth-Coverage or Isoflux antennas: Antennas that have a broad pattern (Isoflux patten) that is shaped to provide equal field strength at all points on the Earth within the field of view (FOV) of the satellite.

EOC: The edge of coverage.

FOV: The field of view.

Image Theory: when a current source is located in the vicinity of a conducting ground plane, image theory permits the removal of the ground plane by placing a virtual image source of the other side of the ground plane.

LEO: Low earth orbit.

Polarization: Polarization is the orientation of electromagnetic waves far from the source. There are several types of polarization that apply to antennas. They are Linear, which comprises, Vertical, Horizontal and Oblique, and circular, which comprises, Circular Right Hand (RHCP); Circular Left Hand (LHCP), Elliptical Right Hand and Elliptical Left Hand.

Radiation Intensity: The power radiated from an antenna per unit solid angle.

Radial Line Slot Array Antenna (RLSA): A radial waveguide with radiation elements (which are slot pairs) on the top plate.

Rotating Mode: A propagating mode (TM11) in a radial waveguide with uniform amplitude and linear phase delay along angular direction.

TEM Mode: Transverse electromagnetic mode characterized by the lack of longitudinal field components.

TABLE OF SYMBOLS AND VARIABLES

$\vec{A}$	Vector Potential (Chapter 2)
A	Atmospheric Attenuation (Chapter 1)
A_0	Attenuation when satellite elevation angle is 90 degrees
a	Aperture Radius of Antenna
$\{\hat{c}\}$	Cartesian coordinate system
D	Directivity
D_{des}	Desired Directivity Pattern
$\vec{E}$	Electrical Field
E_0	Amplitude of aperture field
E_R	Co-Polarized Circularly-Polarized Electric Field
E_L	Cross-Polarized Circularly-Polarized Electric Field
F	Field Array factor
f	Least Square Error Function
$\bar{\bar{G}}$	Green Function
$\vec{H}$	Magnetic Field
H	Orbit Height of the Satellite
H_a	Height of Atmosphere
h	Height of radial waveguide or parallel plate waveguide
$\vec{I}$	Current
$\vec{I}_m$	Magnetic Current (Chapter 2)

I_m	Current on radiation element on m-th circle (Chapter 3, Chapter 4)
$\vec{J}$	Current Density
$\vec{J}_m$	Magnetic Current Density
J_n	Bessel Function (Chapter 4)
$\vec{J}_s$	Surface Current Density
K_0, g_0	Aperture Distribution
k	Wave Number
L	Length of Slot
L_a	The Path Length through the Atmosphere (Chapter 1)
M	Number of slots of an array (Chapter 3)
M	Number of circles where radiation elements are located on the aperture of RLSA (Chapter 3, Chapter 4)
m	Circle number (Chapter 4)
N_m	Number of radiation element on m-th circle
P	Radiation Intensity
R	Distance between a satellite and a point on the earth (Chapter 1)
R_e	Radius of the Earth
r_c	Radius of Centre Block
S	Radiation density
$\{\hat{s}\}$	Spherical coordinate system

W	Width of Slot
λ	Wavelength
λ_g	Wavelength in Radial Waveguide
ϕ_0	Minimum acceptable satellite elevation angle with desired FOV
θ_0	Edge of Coverage (EOC)
ρ	Radial distance
γ_{1m}	Roots for First Order Bessel Function
ρ_m	Radius of m-th Circle
μ	Permeability

LIST OF FIGURES

LIST OF TABLES

CHAPTER 1

Introduction

1.1 EARTH COVERAGE ISOFLUX ANTENNAS FOR SATELLITES

Earth-coverage or isoflux antennas (mounted on-board satellites) are those that have a broad pattern that is shaped to provide equal field strength at all points on the Earth within the field of view (FOV) of the satellite. Fig.1.1-1 shows a sketch of a satellite relative to the Earth. The distance between the satellite and a point on the Earth is denoted by $R(\theta)$. Each point on the Earth will have a different distance to the satellite and so we write this distance as $R(\theta)$ to indicate that it is dependent on θ. The latter angle is equal to θ_0 for a point on the Earth at the edge of coverage (EOC), and the Earth-satellite distance is then at its maximum $R_{max} = R(\theta_0)$. If the point on the Earth is directly "below" the satellite (the sub-satellite point or nadir direction) then the Earth-satellite distance is at its minimum $H = R(0)$ with $\theta = 0°$.

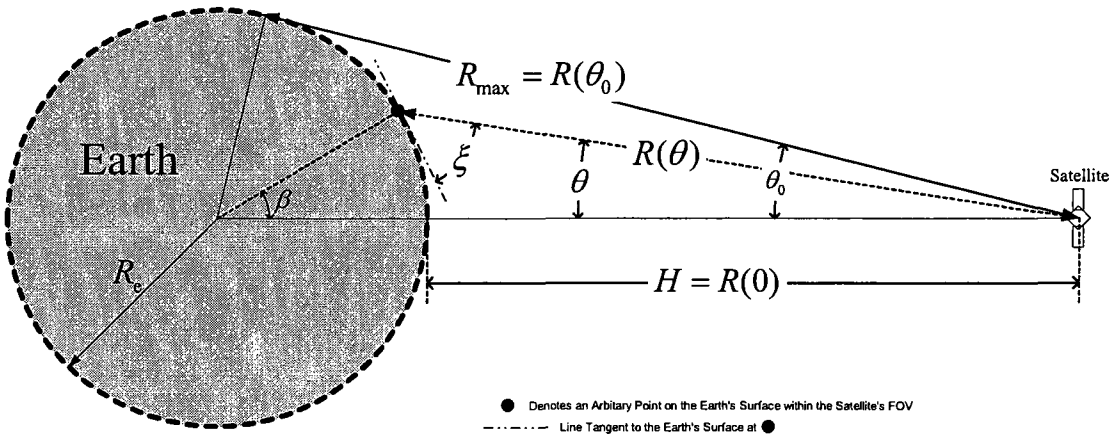

Fig. 1.1-1 Satellite-Earth Characteristics

The quantity H is the orbital height of the satellite. In the case of geostationary (GEO) satellites $H = 35786\,\text{km}$ and hence[1] we have $\theta_0 = 8.7°$. For low-Earth-orbit (LEO) satellites the EOC angle θ_0 can be as large as $65°$.

The quantity $P(\theta)$ depends on the variation in path length R (shown in Fig.1.1-1) from the satellite to the points on the earth's surface that are within the satellite's FOV, and on the atmospheric attenuation A. The desired antenna pattern $P(\theta)$ should provide the same signal strength at its output port (terminal) as a constant-power signal source is moved on the surface of the earth within the satellite's field of view (FOV). $P(\theta)$ is radiation intensity, its relation with radiation power density $S(\theta)$ can be expressed as

$$P(\theta) = R^2 S(\theta) \tag{1.1.1}$$

Quantity R is the distance from the antenna to the observation point on the Earth's surface, and since it depends on θ we write it as $R(\theta)$, we also expect

$$S(\theta) = S(\theta = 0) \tag{1.1.2}$$

If the atmospheric attenuation is neglected, the desired $P(\theta)$ should have the form

$$\frac{P(\theta)}{R(\theta)^2} = \frac{P(\theta = 0)}{H^2} \tag{1.1.3}$$

From (1.1.3) we can say that the desired Earth-coverage antenna pattern $P(\theta)$ satisfies

$$P(\theta) \propto \left(\frac{R(\theta)}{H}\right)^2 \tag{1.1.4}$$

If the atmospheric attenuation is taken into account [1], (1.1.4) must be rewritten as

[1] The radius of the Earth is $R_e = 6378\,km$.

$$P(\theta) \propto \left(\frac{R(\theta)}{H}\right)^2 A(\theta) \qquad (1.1.5)$$

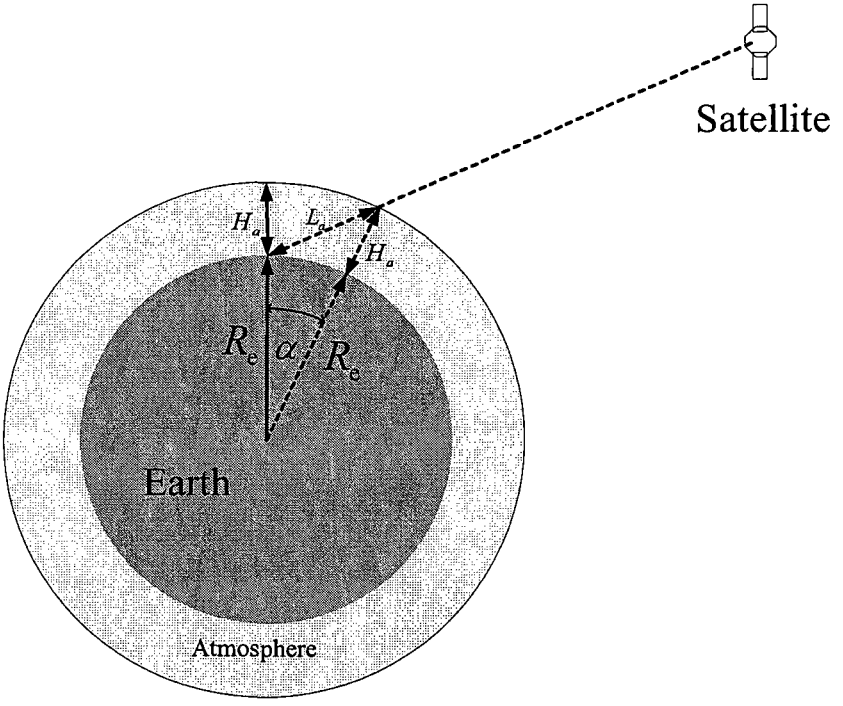

Fig. 1.1-2 Atmospheric Path L_a

To determine $A(\theta)$ refer to Fig.1.1-2 and note that the path length L_a through the earth's atmosphere is given by

$$L_a = \sqrt{(R_e + H_a)^2 + R_e^2 - 2R_e(R_e + H_a)\cos\alpha}$$

It can be written as

$$L_a = H_a\sqrt{(R_e/H_a + 1)^2 + (\frac{R_e}{H_a})^2 - 2(\frac{R_e^2}{H_a{}^2} + \frac{R_e}{H_a})\cos\alpha} = H_a\sqrt{1 + 4(\frac{R_e^2}{H_a{}^2} + \frac{R_e}{H_a})\sin^2(\alpha/2)}$$

If $R_e / H_a >> 1$ is assumed the above expression reduces to

$$L_a \approx H_a \sqrt{1 + 4\frac{R_e^2}{H_a^2}\sin^2(\alpha/2)} \tag{1.1.6}$$

$$\alpha = 90^0 - \phi - \sin^{-1}\left\{\left(\frac{R_e + H}{R_e + H_a}\right)\sin\theta\right\}$$

hence

$$A(\theta) = e^{A_0(1-L_a/H_a)} \tag{1.1.7}$$

where A_0 is the attenuation when $\phi = 90^0$. Referring to Fig.1.1-1, $R(\theta)$ can be determined as

$$R = \sqrt{R_e^2 + (R_e + H)^2 - 2R_e(R_e + H)\cos\beta}$$

which is reduced to

$$R = H\sqrt{1 + 4[(R_e/H)^2 + R_e/H]\sin^2(\beta/2)]} \tag{1.1.8}$$

where

$$\beta = 90 - \theta - \phi \tag{1.1.9}$$

and

$$\phi = \cos^{-1}[(1 + H/R_e)\sin\theta] \tag{1.1.10}$$

The directivity of an antenna with a radiation pattern given by expression (1.1.1) can be calculated from

$$D = \frac{4\pi P(\theta)}{\int_0^{2\pi}\int_0^{\theta_0} P(\theta)\sin\theta\, d\theta\, d\phi} = \frac{4\pi P(\theta)}{2\pi\int_0^{\theta_0} P(\theta)\sin\theta\, d\theta} \tag{1.1.11}$$

where

$$\theta_0 = \sin^{-1}[R_e\cos\phi_0/(R_e + H)] \tag{1.1.12}$$

is the edge of the coverage zone and $P(\theta) = 0$ for θ greater than θ_0. Quantity $P(\theta)$ is identical in all planes containing the $\theta = 0$ axis. Angle ϕ_0 is the minimum acceptable satellite elevation angle within the desired FOV; it is selected from satellite communications systems experience and must generally be less than 20°.

We considered a design of Ka-band antennas for LEO satellites at an altitude of 800km, The coverage regions are where the satellite elevation is more than 15 degrees above the horizon, which means $\phi_0 = 15^0$, the satellite altitude $H = 800km$, the radius of the earth $R_e = 6378km$.

From (1.1.12), we can see, for a low earth orbit satellite, as the satellite altitude decreases, the edge of the coverage zone θ_0 will increase. The desired pattern of (1.1.1) will be a wide beamwidth pattern, shown in Fig.1.1-3. The edge of the coverage zone can be calculated using (1.1.12)

$$\theta_0 = \sin^{-1}[R_e \cos\phi_0 /(R_e + H)] = 59.1^0 \qquad (1.1.13)$$

If the satellite altitude $H = 8000km$, the edge of the coverage zone is only 25.4°.

Substituting $H = 800km$ and $R_e = 6378km$ into (1.1.8), (1.1.9) and (1.1.10), we get

$$\phi = \cos^{-1}[1.125\sin\theta]$$

$$\beta = 90 - \theta - \cos^{-1}(1.125\sin\theta)$$

$$R(\theta) = 800\sqrt{1 + 287.1\sin^2(\beta/2)} \qquad (1.1.14)$$

Using (1.1.1) and (1.1.14), we can obtain the expression of $P(\theta)$

$$P(\theta) \propto (R(\theta)/800)^2 \qquad (1.1.15)$$

the desired directivity pattern is obtained by substituting (1.1.13), (1.1.15) into (1.1.11). The profile of the desired rotationally symmetric directivity pattern with $A_0 = 0\,\text{dB}$ is also illustrated in Fig.1.1-3, compared with the pattern for $H = 8000\,\text{km}$.

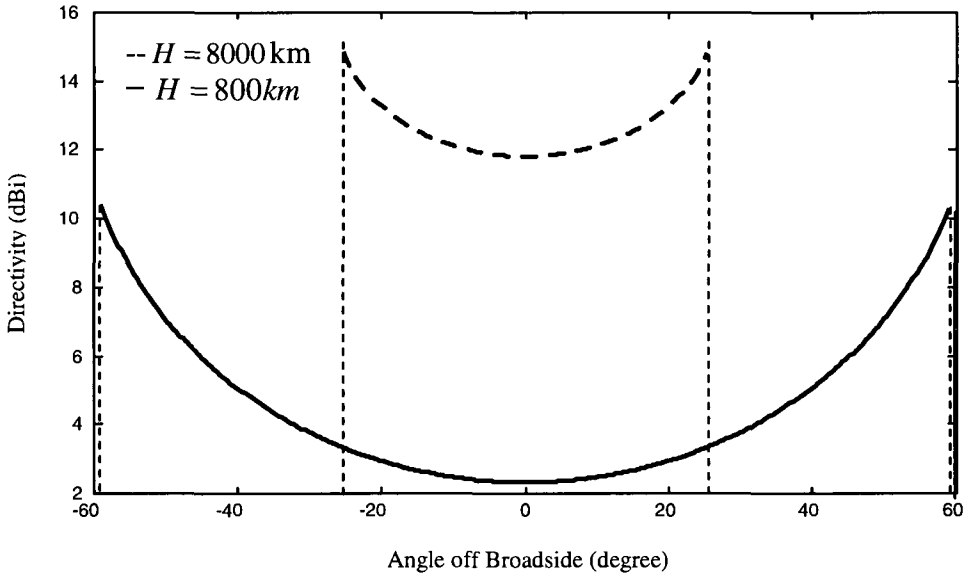

Fig. 1.1-3 Profile of Desired Rotationally Symmetric Directivity Patterns for Satellite Altitudes of (a) 8000km and (b) 800km, $\phi_0 = 15^\circ$

The atmospheric attenuation wasn't taken into account in the Fig.1.1-3, because the height of the atmosphere and atmospheric attenuation are not constants, but they won't make much difference in our case. From the analysis in (1.1.5) and (1.1.7), we can plot the desired directivity pattern with the atmospheric attenuation accounted for (A_0=1dB with $L_a = 122km$). Fig.1.1-4 shows the profile of this pattern compared with the one with $A_0 = 0\,\text{dB}$ (no atmospheric attenuation).

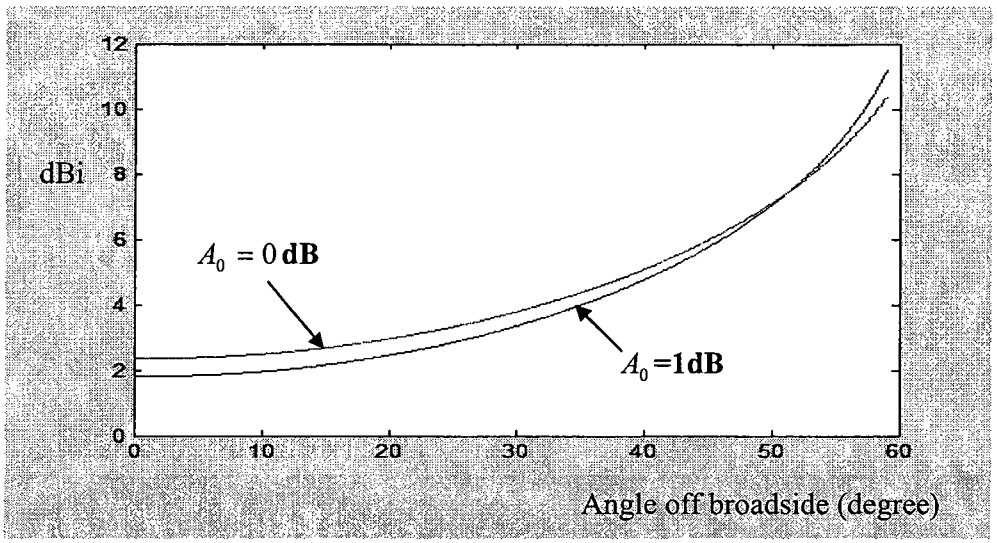

Fig. 1.1-4 Desired Directivity Pattern with (a) $L_a = 122km$, A_0=**1dB (b)** $A_0 = 0$ **dB**

From Fig.1.1-4, we can see, the difference between these two curves is very small, less than 0.5dB, so it is valid assuming $A_0 = 0$ dB in our later analysis.

1.2 LIMITATIONS OF EXISTING ISOFLUX ANTENNAS

Many configurations have been employed to obtain antennas with isoflux radiation patterns for both GEO and LEO satellites. However, it is in LEO applications, with the much larger EOC[2] angle that represents a challenging antenna design problem, that we are here solely interested. Horn antennas with rings at the aperture, such as that shown in Fig.1.2-1, have been described in several publications [2,3,4,5,6,7]. As the satellite altitude decreases it becomes increasingly difficult to obtain the desired wide beam width using such horn antennas; it is difficult to excite an increasing number of outer rings. For instance, for the Globalstar satellites which had H = 1400

[2] The angle of maximum radiation from the antenna's pattern point of view.

km, the EOC angle is 52.4°. However, the horns used for TT&C antennas had a radiation pattern shown in Fig.1.2-2, and so only "*near isoflux* type pattern performance is achieved from nadir to 40° off of nadir" [6]. Other authors who have used ringed horns also considered cases for which the EOC was between 40° and 45° [3,4,7]. EOC angles larger than this require alternative antenna configurations.

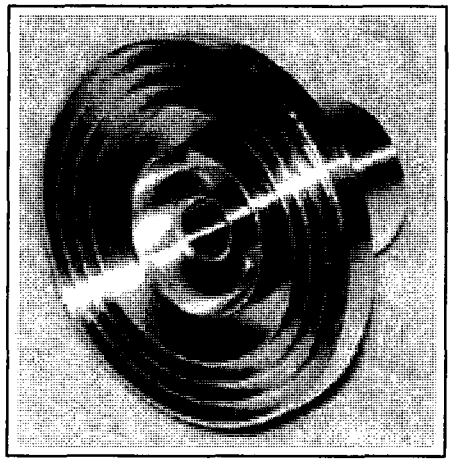

Fig. 1.2-1 Ringed Horn TT&C Antenna (After [2,3])

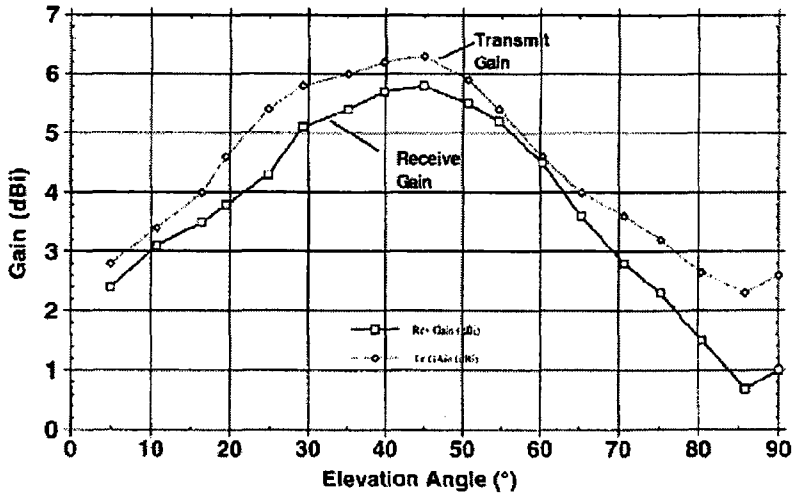

Fig. 1.2-2 Measured Radiation Pattern of C-Band Ringed-Horn TT&C Antenna (After [6])

One antenna geometry that can achieve EOC angles as large 65° is that consisting of a shaped reflector with a rear-radiating feed [3,8]. These configurations and their associated radiation patterns are shown in Figs. 1.2-3 through Fig.1.2-7. They have excellent performance out to wide EOC angles, although near boresight they depart from the ideal isoflux pattern.

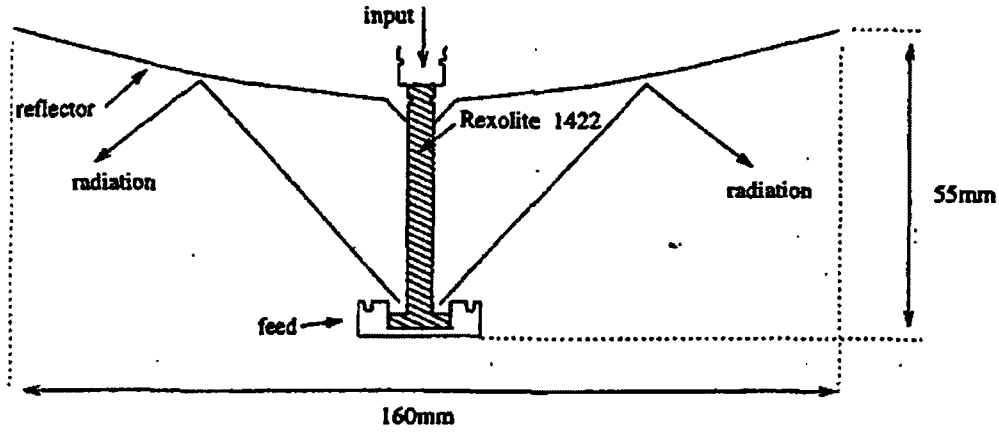

Fig. 1.2-3 Isoflux Antenna Consisting of A Shaped Reflector with a Rear-Radiating Feed (After [3])

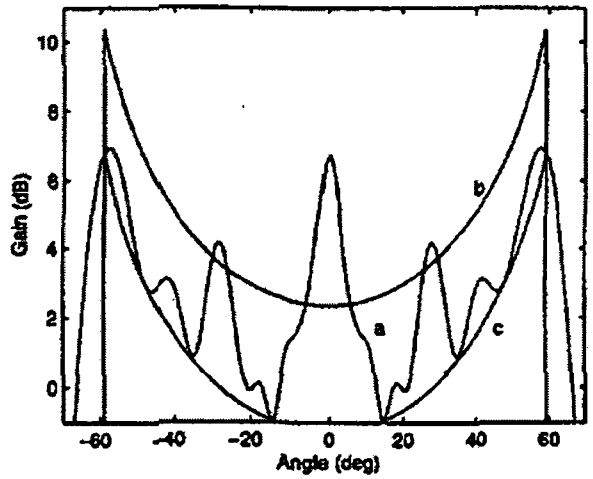

Fig. 1.2-4 Radiation Pattern of The Isoflux Antenna In Fig.1.2-3 at 20.86 GHz (After[3])

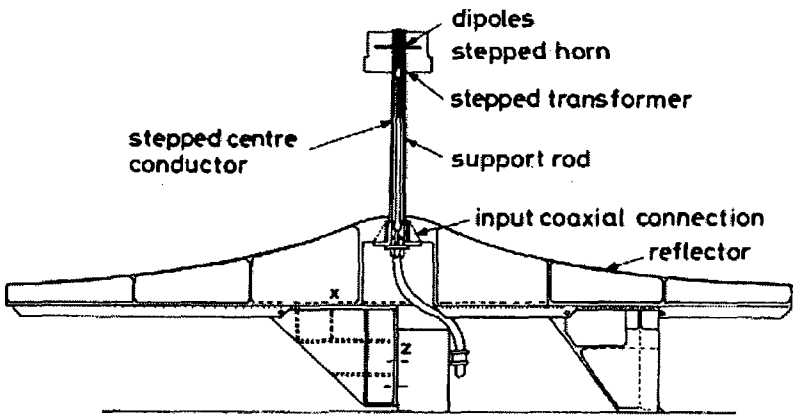

Fig. 1.2-5 Isoflux Antenna Consisting of A Shaped Reflector with a Rear-Radiating Crossed-Dipole Feed (After [8])

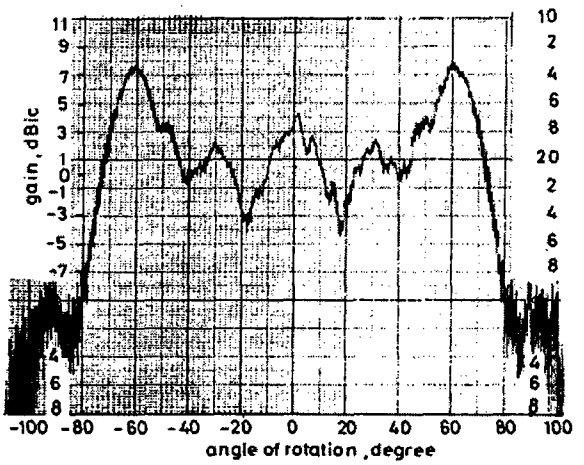

Fig. 1.2-6 Measured Co-Polarised Radiation Pattern of the Isoflux Antenna in Fig.1.2-5 at 8.1 GHz (After [8])

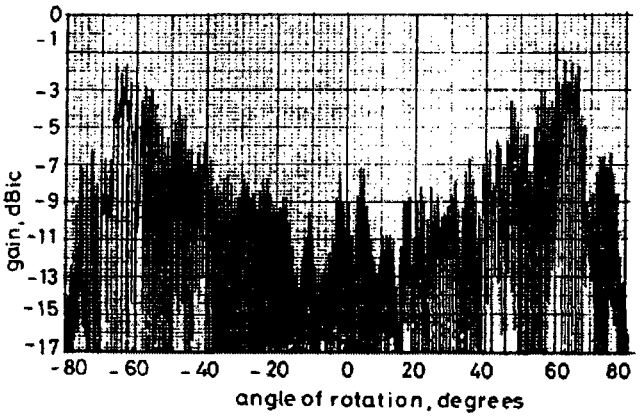

Fig. 1.2-7 Measured Cross-Polarised Radiation Pattern of the Isoflux Antenna in Fig.1.2-5 at 8.1 GHz (After [8])

A third configuration that has been used in an attempt to satisfy wide EOC requirements is the slot-fed biconical type antenna, identified by the acronym SOPERA in [9,10,11]. It is shown in Fig.1.2-8, and its pattern performance in Fig.1.2-9.

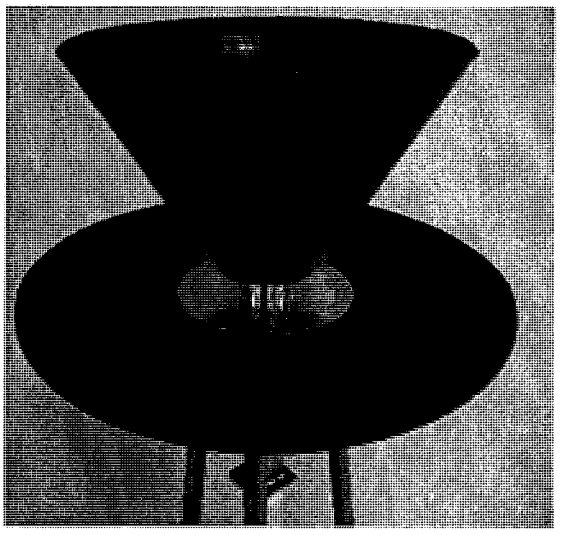

Fig. 1.2-8 Isoflux Antenna Consisting of a Biconical Antenna Fed by an Array of Slots on a Circular Waveguide (After [11])

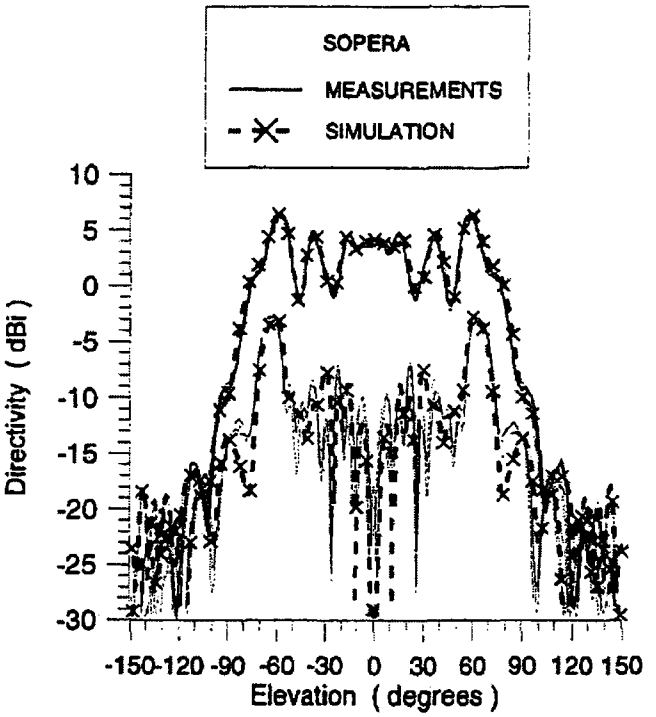

Fig. 1.2-9 Measured Radiation Pattern of the Isoflux Antenna in Fig.1.2-8 at 7.8 GHz (After [10])

The disadvantage of the rear-fed reflector and slot-fed antenna configurations is that they are not low-profile. Considering the advantages of the radial line slot array (RLSA) antenna configuration [13], with high efficiency and low-profile (and entirely metal) structure, it might be an attractive candidate for LEO satellites. Thus far most research on such antennas has concentrated those with uniform aperture illumination to provide pencil beams with linear and circular polarization. The idea here is that shaped pattern radiated by an RLSA antenna should be investigated for isoflux purposes.

In the next section we will briefly describe what an RLSA is. This will be followed by Section 1.4 that will serve to indicate why existing array synthesis techniques are not directly suitable for RLSA design. This leads naturally to Section 1.5, where we provide an overview of the remainder of the thesis.

1.3 BASIC DESCRIPTION OF A RADIAL LINE SLOT ARRAY (RLSA) ANTENNA

The radial line slot array (RLSA) antenna is a radial waveguide with radiating elements (which are slot pairs) on the top plate, as shown in Fig. 1.3-1. The RLSA, which will be described in more detail in Chapters 2 and 3, is an attractive candidate for microwave and millimeter-wave applications, since its advantages include high radiation efficiency[3], low-profile, low cost compared to other non-printed antenna arrays, and a rear-mounted feed-point.

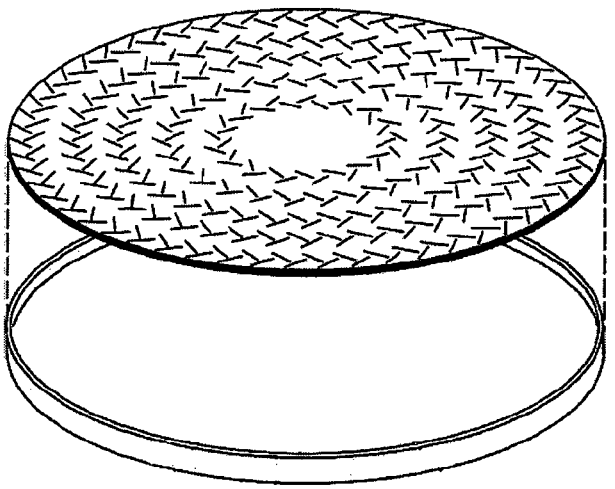

Fig. 1.3-1 RLSA Antenna Lid Showing Slot Pairs (After [13])

RLSA antennas can be divided into two classes: those that use a *non-rotating field* in the radial waveguide to excite the slots, and those that use *rotating fields*. The non-rotating mode of operation is achieved by exciting the RLSA at the centre of its base-plate using a coaxial probe, as shown in Fig.1.3-2. If the radiating slot-pairs are located on concentric circles (as in Fig.1.3-1) then linearly polarized radiation is obtained; if they are located on a spiral locus (as in Fig.1.3-3)

[3] Compared to beamforming networks realized in microstrip line the transmission losses in the radial-waveguide beamforming are very small.

then circular polarization results. The rotating mode of operation is obtained by feeding the RLSA at the centre of its base-plate with a single pair of crossed-slots which are in phase-quadrature, as illustrated in Fig.1.3-4. If the radiating slot-pairs are located on concentric circles then circularly polarized radiation is obtained.

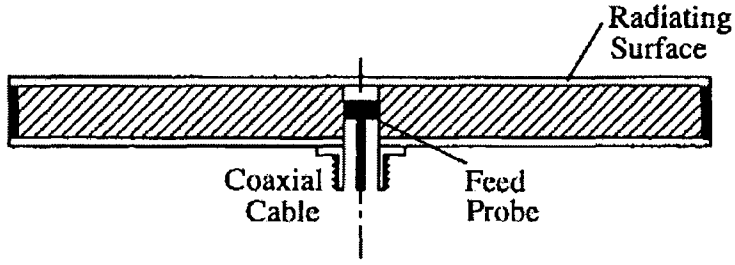

Fig. 1.3-2 RLSA Antenna with Coaxial Probe Feed (After [14])

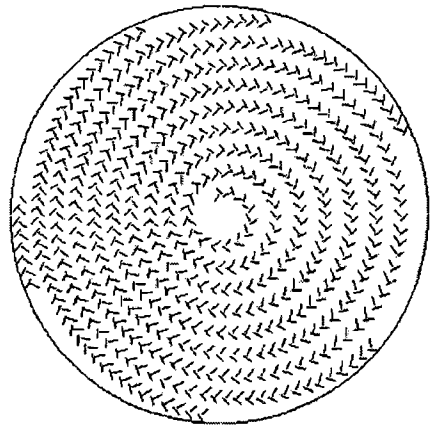

Fig. 1.3-3 RLSA Antenna Slot-Pairs Located on a Spiral Locus (After [15])

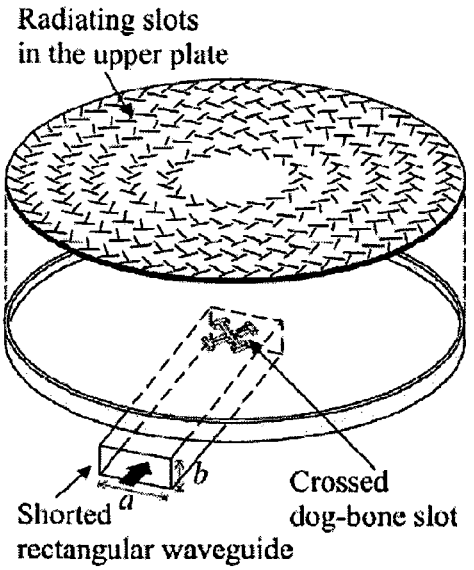

Fig. 1.3-4 RLSA Antenna with Crossed-Slot Feed (After [16])

1.4 RELEVANCE OF EXISTING ARRAY PATTERN SYNTHESIS TECHNQUES

Many techniques have been developed for performing a radiation pattern synthesis[4] for array antennas. However, almost all of these assume that the radiating elements have the same orientation, and that they are located on a regular linear or rectangular grid. Neither of these is true for the RLSA antenna. A literature search has not revealed any pattern synthesis methods developed and used for RLSA antennas. Most RLSA designs have simply striven to provide uniform amplitude and phase distributions. Thus we will in this thesis develop a synthesis method that is specifically suited to RLSA antenna synthesis.

1.5 OVERVIEW OF THE THESIS

The aim of this thesis is to explore the suitability of the RLSA configuration as a low-profile antenna capable of providing isoflux radiation patterns with large EOC angles. Chapter 2

[4] That is, determining the relative excitation amplitude and phase of each of the array elements.

discusses the form of the fields inside the RLSA radial waveguide section. In particular, it shows the dependence of the field (and hence the lid currents) on the form of the excitation, and demonstrates the difference between the rotating and non-rotating modes. A clear examination of this kind has not yet appeared elsewhere. This is followed by a brief review of the quite vast literature on RLSA antennas. Chapter 3 provides a detailed analysis of the vector radiation patterns of the RLSA configuration that is proposed for use as an isoflux antenna. This is needed before any synthesis procedure can be performed, and is also not available elsewhere. Chapter 4 presents a new synthesis procedure for RLSA antennas. It is applied to the synthesis of RLSA antennas with isoflux patterns in Chapter 5, and a discussion of the suitability of the RLSA configuration for isoflux antennas is discussed. Chapter 6 provides some general conclusions.

1.6 REFERENCES FOR CHAPTER 1

[1] L. J. Ricardi, "Satellite Antennas", Chapter 36 in: R.C. Johnson, *Antenna Engineering Handbook* (3rd Edition), McGraw-Hill, 1993.

[2] D. G. Bateman, S.G. Hay, T.S. Bird & F.R. Cooray, "Simple Ka-band Earth-coverage antennas for LEO satellites", *Proc. Australian Symposium on Antennas*, Feb. 1999.

[3] S. G. Hay, D. G. Bateman, T. S. Bird and F. R. Cooray, "Simple Ka-band earth-coverage antennas for LEO satellites", *IEEE AP-S Int. Symp. Digest,* vol.1, pp. 708-711, 1999.

[4] P. Brachat, "Sectoral patern synthesis with primary feeds", *IEEE Trans. Antennas Propagat.*, vol.42, no. 4, pp. 484-491, Apr.1994.

[5] P. Metzen, "Satellite communications antennaas for Globalstar", *Proc. Int. Antenas Symp. (JINA), Nice, France*, pp.574-583, Nov. 1996.

[6] F. J. Dietrich, P. Metzen & P. Monte, "The Globalstar cellular satellite system", *IEEE Trans. Antennas Propagat.*, vol.46, no. 6, pp. 935-942, Jun. 1998.

[7] L. T. Hildebrand, D. A. McNamara & G. Arbery, "Low-cost physically-small TT&C antennas for LEO satellite applications", *Proc. 11th CASI Conference on Astronautics (ASTRO'2000)*, Ottawa, Canada, 7-9 Nov. 2000.

[8] A. Kumar, "Highly shaped beam telemetry antenna for the ERS-1 satellite", *IEE Proc.*, Vol.134, Pt.H, No.1, pp.106-108, Feb.1987.

[9] J. E. Fernández Del Rio, A. Nubla, L. Bustamante and K. van't Klooster, "SOPERA: A new antenna concept for low earth orbit satellites," *IEEE AP-S Int. Symp. Digest*, Vol. 1, pp. 688-691, Jun. 1999.

[10] J. E. Fernández Del Rio, A. Nubla, L. Bustamante, F.Vila, K. van't Klooster and A.Frandsen, "Novel isoflux antenna alternative for LEO satellites downlink", *Proc. 29th European Microwave Conference,* pp.154-157, Munich, Germany, 1999.

[11] *RYMSA*, Ctra. Campo Real, Km 2, 100– 28500 Arganda del Rey, Madrid, Spain (www.rymsa.com).

[12] G. van Dooren & R. Cahill, "Design, analysis and optimisation of quadrifilar helix antennas on the European Metop spacecraft", *Proc. Int. Conf. Antennas & Propagation*, pp. 1.536-1.542, Edinburgh, United Kingdom, 1997.

[13] K. Sudo, T. Oizumi, J. Hirokawa & M. Ando, "Reduction of azimuthal ripple in the rotating-mode feed to a radial waveguide by using a crossed dog-bone slot", *IEEE Trans. Antennas Propagat.*, vol.55, no. 9, pp.2618-2622, Sept. 2007.

[14] P. W. Davis and M. E. Bialkowski, "Experimental investigations into a linearly polarized radial slot antenna for DBS TV in Australia," in *IEEE Trans. Antennas Propagat.*, vol. 45, no. 7, pp. 1123-1129, Jul. 1997.

[15] M. Vera-Isasa, M. Sierra-Castañer and M. Sierra-Pérez, "Slot antenna with a tilted beam for satellite reception", *Microwave and Optical Technology Lett.*, vol. 36, no. 5, pp. 392-394, Mar. 2003.

[16] K. Sudo, T. Oizumi, J. Hirokawa and M. Ando, "Reduction of azimuthal amplitude ripple in the rotating-mode feed to a radial waveguide by using a crossed dog-bone slot", *IEEE Trans. Antennas Propagat.*, vol. 55, no. 9, pp. 2618-2622, Sept. 2007.

CHAPTER 2

Radial Line Slot Antennas

2.1 INTRODUCTION

This chapter will serve three purposes. Firstly, it will in Section 2.2 and Section 2.3 consider the form of the fields in a radial waveguide of infinite extent for two types of excitation that give rise to so-called non-rotating and rotating mode fields, respectively. A clear understanding of this aspect is a key to appreciating the various types of RLSA antennas that are in use. This allows us to proceed more easily to Section 2.4, where a concise review of the abundant literature on RLSA antennas is given. Section 2.5 will provide some concluding remarks to the chapter.

2.2 FIELD EXCITATION OF RADIAL WAVEGUIDE: NON-ROTATING MODE

2.2.1 Preliminary Remarks

RLSA antennas use one of two modes in radial waveguide, namely the TEM mode (non-rotating mode) or the TM11 mode (rotating mode), and hence the radiating slot structure, on the top plate of the radial waveguide depends on which mode is used. In the next section the fields in a radial waveguide are examined using image theory and vector potential analysis.

2.2.2 Non-Rotating Mode Fields

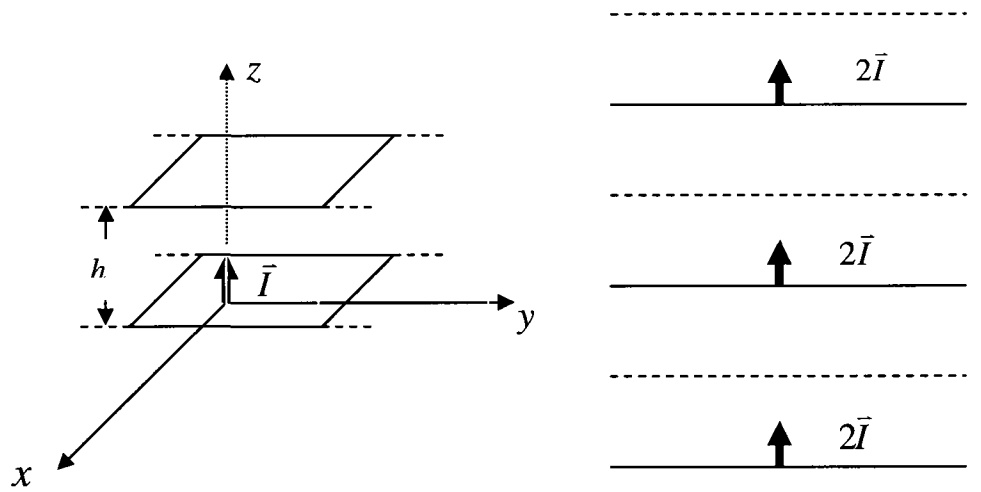

(a) (b)

Fig. 2.2-1: (a). Infinitesimal Electric Current Element Between Two Parallel Conducting Planes; (b). Application of Image Theory to the Physical Problem in (a).

The infinite parallel plate waveguide geometry (that is, radial waveguide geometry) under consideration is shown in Fig. 2.2-1. Quantity h is the height of the infinite parallel plate waveguide. The coordinate origin is at the centre of the bottom plate. There is an infinitesimal z-directed electric current element at the origin. If the current element were in free space we would have $\vec{I}dl = \hat{z}\, I_0 dl$, and the magnetic vector potential would be

$$\vec{A} = \frac{\mu}{4\pi} \iiint_{V'} \vec{J} \frac{e^{-jkR}}{R} dV' = \frac{\mu}{4\pi} \iiint_{V'} I_0 \frac{e^{-jkR}}{R} dl\, \hat{z} = \hat{z} \frac{\mu I_0 dl}{4\pi} \frac{e^{-jkR}}{R} \qquad (2.2.1)$$

where R is the distance between source and field points, and V' is the volume occupied by the sources.

With the current element located inside the parallel plate waveguide, its vector potential can be found by superposition of (2.1.1) due to the original electrical dipole and its infinity of images shown in Fig. 2.2-1(b). The vector potential in the waveguide is therefore

$$\vec{A}_{tot} = \hat{z}2\frac{\mu I_0 dl}{4\pi}\sum_{n=-\infty}^{+\infty}\frac{e^{-jkR_n}}{R_n} = \hat{z}\frac{\mu I_0 dl}{2\pi}\sum_{n=-\infty}^{+\infty}\frac{e^{-jkR_n}}{R_n} = \hat{z}A_z \qquad (2.2.2)$$

where

$$R_n = \sqrt{x^2 + y^2 + (z+2nh)^2} \qquad (2.2.3)$$

and

$$A_z = \frac{\mu I_0 dl}{2\pi}\sum_{n=-\infty}^{+\infty}\frac{e^{-jkR_n}}{R_n} \qquad (2.2.4)$$

The magnetic field excited by this dipole in the radial waveguide can then be determined using $\vec{H} = (1/\mu)\nabla \times \vec{A}_{tot}$ as

$$H_x = \frac{1}{\mu}\frac{\partial A_z}{\partial y} = -\frac{yI_0 dl}{2\pi}\sum_{n=-\infty}^{+\infty}(1+jkR_n)\frac{e^{-jkR_n}}{R^3{}_n} \qquad (2.2.5)$$

$$H_y = -\frac{1}{\mu}\frac{\partial A_z}{\partial x} = \frac{xI_0 dl}{2\pi}\sum_{n=-\infty}^{+\infty}(1+jkR_n)\frac{e^{-jkR_n}}{R^3{}_n} \qquad (2.2.6)$$

Numerical evaluation of (2.2.5) and (2.2.6) shows that $H_\rho = 0$ and that the amplitude and phased variation of $H_\varphi(\varphi, \rho)$ is as shown in Fig. 2.2-2[5]. This reveals that the fields in the radial

[5] The cylindrical components of the field in the radial waveguide can of course be found from $H_\rho = H_x\cos\varphi + H_y\sin\varphi$, $H_\varphi = -H_x\sin\varphi + H_y\cos\varphi$ and $\vec{H} = \hat{\rho}H_\rho + \hat{\varphi}H_\varphi$.

waveguide, with the type of excitation assumed here (that is, a vertical electric current element), is a TEM non-rotating mode. In practice this type excitation is realized in the manner shown in Fig. 1.3-2.

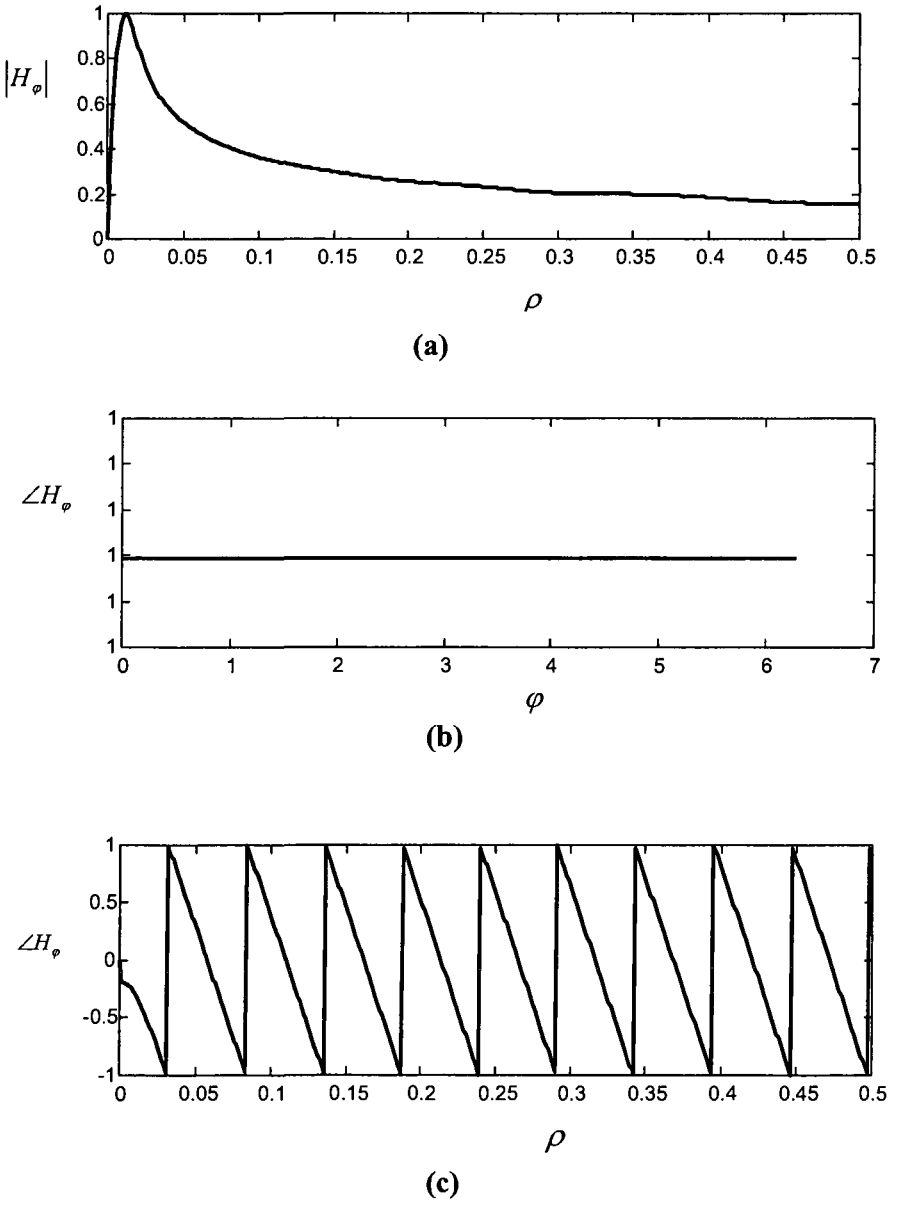

Fig. 2.2-2 : Magnetic Fields of a Non-Rotating Mode (TEM) in Radial Waveguide.

2.3 FIELD EXCITATION OF RADIAL WAVEGUIDE : ROTATING MODE

We next assume an excitation consisting of two spatially-orthogonal infinitesimal magnetic current elements, with a 90 degree phase difference between them, located on the bottom plate of the radial waveguide, as shown in Fig. 2.3-1.

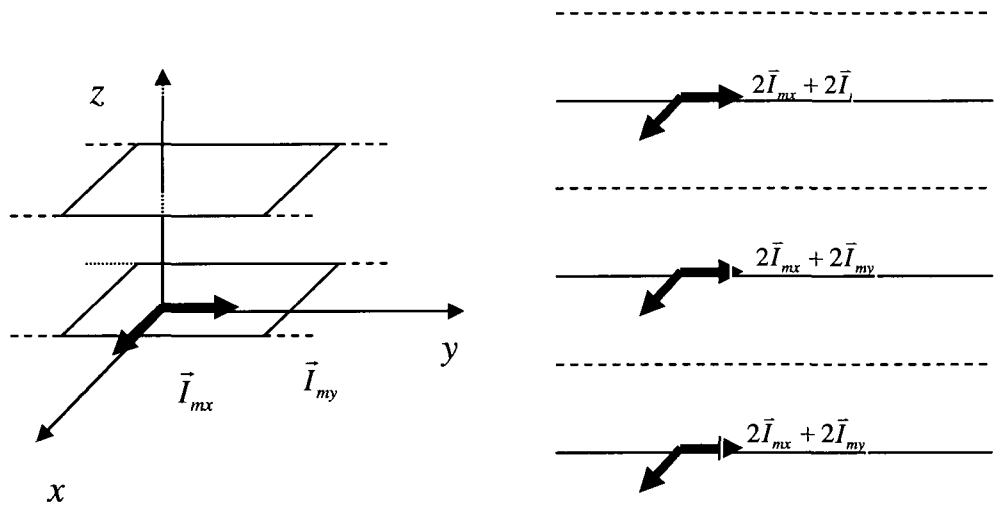

(a) **(b)**

Fig. 2.3-1 : (a). Infinitesimal Magnetic Current Elements Between Two Parallel Conducting Planes; (b). Application of Image Theory to the Physical Problem in (a).

Expressions for these current elements are

$$\vec{I}_{mx} = \vec{x}\, I_{mx} dl \qquad \text{with} \qquad I_{mx} = I_{m0} e^{j\omega t} \tag{2.3.1}$$

$$\vec{I}_{my} = \vec{y}\, I_{my} dl \qquad \text{with} \qquad I_{my} = I_{m0} e^{j(\omega t - \pi/2)} \tag{2.3.2}$$

so that

$$\vec{J}_m ds = \vec{I}_m dl = \vec{x} I_{mx} dl + \vec{y} I_{my} dl \qquad (2.3.3)$$

Known Green's function theory, along with image theory, can be used to find the magnetic field in the radial waveguide as

$$H_x = \bar{\bar{G}}_{xx} I_{mx} dl\,(-j\omega\varepsilon_0) + \bar{\bar{G}}_{xy} I_{my} dl\,(-j\omega\varepsilon_0) \qquad (2.3.4)$$

$$H_y = \bar{\bar{G}}_{yx} I_{mx} dl\,(-j\omega\varepsilon_0) + \bar{\bar{G}}_{yy} I_{my} dl\,(-j\omega\varepsilon_0) \qquad (2.3.5)$$

and

$$H_z = \bar{\bar{G}}_{zx} I_{mx} dl\,(-j\omega\varepsilon_0) + \bar{\bar{G}}_{zy} I_{my} dl\,(-j\omega\varepsilon_0) \qquad (2.3.6)$$

where the Green's function components (with the contributions of the infinity of images already included) are

$$\bar{\bar{G}}_{xx} = G_0^a - \frac{\partial^2 G_0^a}{k^2 \partial x^2}, \quad \bar{\bar{G}}_{yx} = \frac{\partial^2 G_0^a}{k^2 \partial y \partial x}, \quad \bar{\bar{G}}_{zx} = \frac{\partial^2 G_0^a}{k^2 \partial z \partial x}, \qquad (2.3.7)$$

$$\bar{\bar{G}}_{yy} = G_0^a - \frac{\partial^2 G_0^a}{k^2 \partial y^2}, \quad \bar{\bar{G}}_{zy} = \frac{\partial^2 G_0^a}{k^2 \partial z \partial y} \qquad (2.3.8)$$

$$G_0^a = \sum_{n=-\infty}^{+\infty} \frac{e^{-jkR_n}}{2\pi R_n} \qquad (2.3.9)$$

$$\bar{\bar{G}}_{xx} = \sum_{n=-\infty}^{+\infty} \frac{e^{-jkR_n}}{R_n} - \frac{1}{2\pi k^2} \sum_{n=-\infty}^{+\infty} \frac{e^{-jkTR_n}}{R_n^5} (R_n^2 + jkR_n^3 - 3jkR_n x^2 - 3x^2 + R_n^2 k^2 x^2) \qquad (2.3.10)$$

$$\bar{\bar{G}}_{yy} = \sum_{n=-\infty}^{+\infty} \frac{e^{-jkR_n}}{R_n} - \frac{1}{2\pi k^2} \sum_{n=-\infty}^{+\infty} \frac{e^{-jkR_n}}{R_n^5} (R_n^2 + jkR_n^3 - 3jkR_n y^2 - 3y^2 + R_n^2 k^2 y^2) \qquad (2.3.11)$$

$$\bar{\bar{G}}_{yx} = \frac{xy}{2\pi k^2} \sum_{n=-\infty}^{+\infty} \frac{e^{-jkR_n}}{R_n^5} (-3 - 3jkR_n + R_n^2 k^2) \qquad (2.3.12)$$

$$\bar{\bar{G}}_{zx} = -\frac{x}{2\pi k^2}\sum_{n=-\infty}^{+\infty}\frac{(z+2nh)\cdot e^{-jkR_n}}{R_n^5}(-3-3jkR_n+R_n^2k^2) \qquad (2.3.13)$$

and

$$\bar{\bar{G}}_{zy} = -\frac{y}{2\pi k^2}\sum_{n=-\infty}^{+\infty}\frac{(z+2nh)\cdot e^{-jkR_n}}{R_n^5}(-3-3jkR_n+R_n^2k^2) \qquad (2.3.14)$$

The electric current on the top plate is

$$\vec{J}_s = -\hat{z}\times\vec{H} = -\hat{z}\times(\hat{\rho}H_\rho + \hat{\varphi}H_\varphi) = -\hat{\varphi}H_\rho + \hat{\rho}H_\varphi \qquad (2.3.15)$$

Field H_ρ decays along the radial direction very quickly, so that J_φ is small, and we principally have a radially directed surface current density

$$\vec{J}_s = \hat{\rho}H_\varphi \qquad (2.3.16)$$

Numerical evaluation of (2.3.4) and (2.3.5) provide the plots in Fig. 2.3-2. These reveal that we have a rotating mode in the radial waveguide for the type of excitation (that is, crossed slots in phase quadrature) assumed here. This can be realized in practice using two spatially orthogonal slots (of slightly different lengths to obtain the phase quadrature) in the bottom plate, as illustrated in Fig.1.3-4.

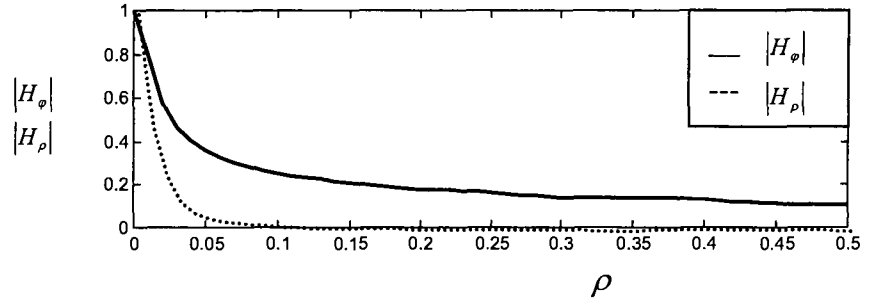

(a)

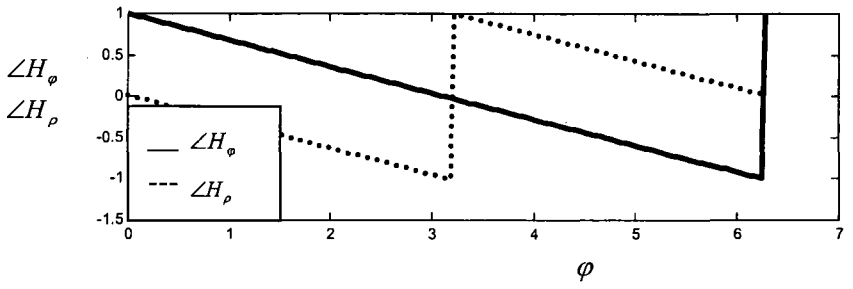

(b)

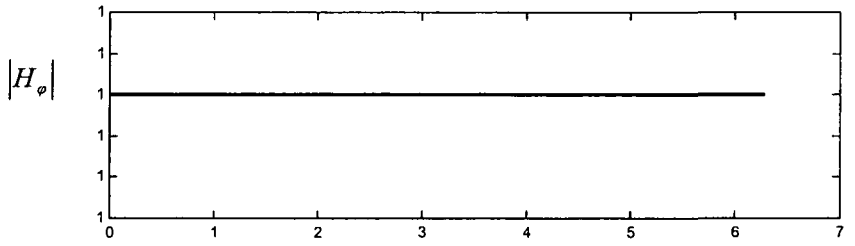

(c)

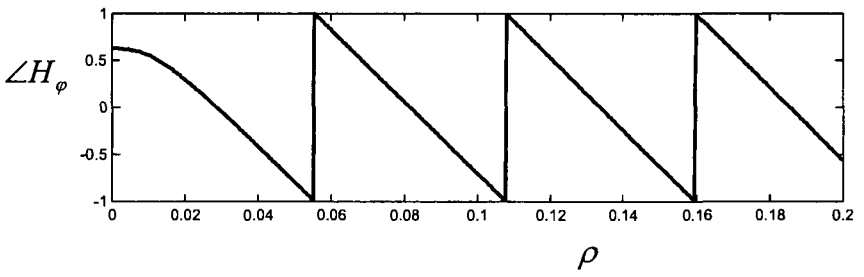

(d)

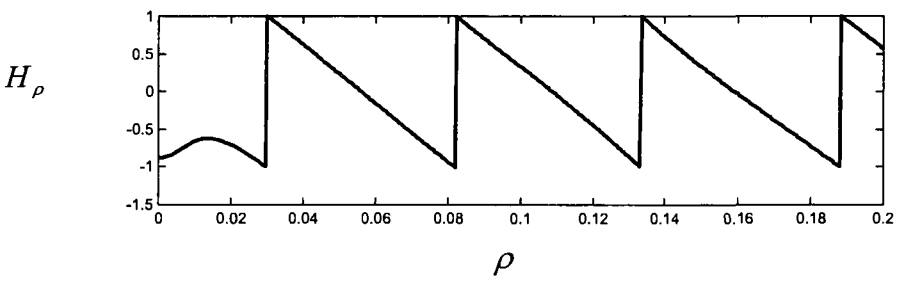

(e)

Fig. 2.3-2 : Magnetic Fields of a Rotating Mode in Radial Waveguide.

2.4 REVIEW OF RADIAL LINE SLOT ARRAY ANTENNAS

The concept of an RLSA antenna was introduced at the end of the 1950s [1], and an X-band planar antenna using a radial waveguide with annular slots was demonstrated by Goebels and Kelly in the early of 1960s. It consisted of a set of slots arranged on the upper plate of a radial waveguide with a coaxial feeding element at the center of the antenna; further modification was made to receive and transmit signals according to their polarization [2,3,4].

Goto and Yamamoto [5] were the first to propose the commercial use of an RLSA antenna operating with a travelling TEM wave excitation for the 12 GHz band in 1980. They suggested a novel high gain planar antenna with a circularly polarized broadside beam RLSA antenna for the application of receiving direct broadcast from a satellite (DBS). The efficiency is reported to be no less than 70%. The aperture layout and radiation unit (slot-pair) arrangement as first presented in [5] is used by later RLSA antenna designs. Slot pairs act as a radiation unit for circular polarization, and they are arranged perpendicular to each other and separated a quarter wavelength along the radial direction to establish a 90 degree phase difference between them. The slot pairs on the aperture are arranged spirally to obtain the same amount of electrical advance as the slot pairs geometrically rotated by an angle to produce a circularly polarization. By re-arranging the aperture arrangement of the slot-pairs a linear polarized RLSA was demonstrated in 1988 [6].

If the radial waveguide is folded and is fed at the centre of the lower waveguide to realize a radially inward travelling TEM mode, one has what is called double-layered RLSA. The drawback of the double-layered RLSA is the relatively complicated waveguide structure and the high cost of fabrication. This problem was solved by Takahashi [7] in 1989 by recommending a single layered RLSA antenna structure to excite a radially outward-travelling TEM wave. Another problem appears for small-sized RLSA antenna because the spiral aperture arrangement disturbs

an axial symmetry of aperture distribution and increases termination losses at the end of radial waveguide. This shortcoming has been overcome by using the rotating mode RLSA antenna first proposed by Hosono et al. in 1994 [8]. With a rotating mode excited in the radial waveguide, the slots are arranged concentrically over the antenna aperture for a circular polarization requirement. A uniform aperture distribution is used in [8] to give a pencil beam in the broadside direction. The feeding circuit for the rotating mode in [8] consists of a cavity resonator excited by a feeding pin. However, the crossed slot waveguide feed designed by Sudo et al. [9] in 2001 is more convenient and more widely used.

Currently RLSA antennas are not only used for DBS reception at 12 GHz in Japan, but have also been found to be a good candidate in many other applications requiring a high gain antenna because of its high efficiency and simple structure. Akiyama et al. [10] proposed a millimetre wave RLSA antenna with conical beam for the 60 GHz band wireless LAN. An elevational and azimuthal multibeam RLSA antenna is presented by Takada et al. [11] for mobile satellite communication and broadcasting service. Plasma production using a rotating mode RLSA antenna is reported by Yamamoto et al. [12]. RLSA antennas for indoor WLAN at 2.4/5.2 GHz are demonstrated by Bialkowski and Zagriatski [13].

A uniform aperture distribution is required for the RLSA antennas designed to produce a high gain broadside pencil beam or conical beam. Under the assumption of weak slot coupling, the analysis model of rectangular waveguide with periodic wall is used by Ando et al. [14], and combined with the method moments (MoM) and an optimization procedure in [15], in order to determine the precise slot parameters (length and width) and locations to realize the uniform aperture distribution. The limitation of this model is that the aperture structure has to be uniform, but is sufficiently rapid to be used with arrays of large numbers of slots. Other analysis models

have also been proposed to determine the above the slot parameters[6]. The network model is used by M. S. Pérez et al. [16], and is fast enough to be used in an optimization process for small and medium sized RLSA antennas. Boryssenko [17] set up an alternative equivalent circuit model which is used for small aperture RLSA antennas. An efficient full-wave MoM analysis method introduced by Albani et al. [18] can analyze an entire RLSA antenna with a large number of slot-pairs. When an RLSA antenna is considered for isoflux pattern applications a uniform aperture distribution will of course not suffice.

2.5 CONCLUSIONS

Although not a key contribution, we have presented a quantitative analysis which clearly demonstrates how to produce non-rotating or rotating mode fields in the radial waveguide. Although perhaps not new, such a concise explanation of how elementary sources produce such modes does not appear to be available elsewhere in the literature.

2.6 REFERENCES FOR CHAPTER 2

[1] K. C. Kelly, "Recent annular slot array experiments", *IRE International Convention Record,* vol. 5, pp. 144-152, 1957.

[2] F. J. Goebels and K. C. Kelly, "Arbitrary polarization from annular planar antenna", *IRE Trans.On Antennas and Propagation,* Vol. AP-9, pp. 342-349.94, 1961.

[3] K. C. Kelly and F. J. Geobels, "Annular slot monopulse antennas", *IRE Trans. Antennas Propagat.*, vol. 12, no. 4, pp. 391-403, Jul. 1964.

[4] F. J. Geobels and K. C. Kelly, "Arbitrary polarization from annular slot planar antennas", *IRE Trans. Antennas Propagat.*, vol. AP-9, pp. 342-349, Jul.1969.

[6] That is, to complete the array design once the required array element excitations have been determined from the pattern synthesis procedure. As far as we have been able to determine, only uniform aperture distributions have been used thus far in the literature.

[5] N. Goto and M. Yamamoto, "Circularly polarized radial-line slot Antennas", *IECE Tech. Rep.*, AP 89-54, Aug.1980.

[6] M. Ando, J. Takada, T. Numata and N. Goto, "A linearly polarized radial line slot antenna", *IEEE Trans. Antennas Propagat.*, vol. 36, issue 12, pp.1675-1680, 1988.

[7] M.Takahashi, J. Takada, M. Ando and N. Goto, "A single-layered radial slot line slot antenna", *IEEE Technical Report*, AP89-54, Oct.1989.

[8] S. Hosono, J. Hirokawa, M. Ando, N. Goto and H. Arai, "A rotating mode radial line slot antenna fed by a cavity resonator", *IEEE AP-S Int. Symp. Digest*, vol. 3, pp. 2200-2203, 1994.

[9] K. Sudo, A. Akiyama, J. Hirokawa and M. Ando, "A Millimeter-wave radial line slot antenna fed by a rectangular waveguide through a ring slot", *IEEE AP-S Int. Symp. Digest,* vol. 2, pp.254-257, 2001.

[10] A. Akiyama, T. Yamamoto, M. Ando and E. Takeda, "Conical beam radial line slot antennas for 60GHz band wireless LAN", *IEEE AP-S Int. Symp. Digest*, vol. 3, pp. 1421-1424, 1998.

[11] J. Takada, T. Yamamoto, M. Ando and N. Goto, "Circularly polarized multibeam radial line slot antennas for moblie satellite communication", *IEEE AP-S Int. Symp. Digest*, vol. 3, pp. 1430-1433, 1995.

[12] T. Yamamoto, M. Ono, M. Ando, N. Goto and N. Ishii, "Near field distributions of in radial line slot antennas for surface wave coupled plasma Generation", *IEEE AP-S Int. Symp. Digest*, vol. 2, pp. 986-989, 1999.

[13] K. S. Bialkowski and S. Zagriatski, "A dual band 2.4/5.2GHz antenna including a radial line slot array and a patch", *IEEE AP-S Int. Symp. Digest*, vol. 3, pp. 3095-3098, 2004.

[14] J. Hirokawa, M. Ando, and N. Goto, "Analysis of slot coupling in a radial line slot antenna for DBS reception", *IEE Proc.*, vol. 137, pt. H, no. 5, pp. 249-254, Oct. 1990.

[15] A. Akiyama, T. Yamamoto, M. Ando and N. Goto, "Numerical optimization of slot parameters for a concentric array radial line slot antenna", *IEE Proc. Microwave Antennas Propag.*, vol. 145, no. 2, pp. 141-145, Apr. 1998.

[16] M. S. Pérez, M. Vera-Isasa, A. G. Pino and M. Sierra-Castaner, "Analysis of slot antennas on a radial transmission line", *Int. J. Microwave Millimeter-Wave Computer-Aided Eng.*, vol. 6, no. 2, pp. 115-127, Feb. 1996.

[17] A. Boryssenko, "Millimeter-waves radial-line slot array antenna", *Proc. of 1999 Antenna Applications Symp.*, Monticello, Illinois, pp. 349-373, Sept. 1999.

[18] M. Albani, G. La Cono, R. Gardelli and A. Freni, "An efficient full-wave method of moments analysis for RLSA antennas", *IEEE Trans. Antennas Propagat.*, vol. 54, no. 8, pp. 2326-2336, Aug. 2006.

CHAPTER 3

The Radiation Pattern Analysis of Radial Line Slot Antennas

3.1 INTRODUCTION

Despite the myriad of references available on RLSA antennas the details of an analysis that will provide the complete vector radiation patterns (with full polarization properties) is not provided anywhere. Formulating such an analysis is the sole purpose of the present chapter. Since the radiating slots all have different orientations and locations the pattern cannot be expressed using the "pattern multiplication" principle normally used for array antennas of identical elements. We must instead find the pattern of a single slot of some arbitrary location and orientation, and then add up the contribution due to each slot. We will find it useful to use a number of local coordinate systems and their relations to a global coordinate system. These are defined in Section 3.2. The subsequent Sections 3.3, 3.4, 3.5 and 3.6 then work through the individual steps and superposition mentioned previously in order to arrive at an expression for the vector patterns of an RLSA antenna. Section 3.7 concludes the chapter and points the way to the next.

3.2 COORDINATE SYSTEM FOR RADIAL LINE SLOT ARRAY ANTENNA ANALYSIS

We introduce six coordinate systems and the relationship between their spatial variables, as well as the relationship between vector field components expressed in terms of these coordinates:

A. Coordinate Systems $\{\hat{c}\}$ And $\{\hat{s}\}$

$\{\hat{c}\}$: Cartesian coordinate system - The origin is located at the centre of the array antenna aperture and the z axis perpendicular to the antenna aperture. The location of the observation point P is expressed as (x, y, z), as shown in Fig.3.2.1.

$\{\hat{s}\}$: Spherical coordinate system - The origin is located at the centre of the array antenna aperture. The location of the observation point P is expressed as (r, θ, ϕ), shown in Fig.3.2-1. The relation between (x, y, z) and $\{r, \theta, \phi)$ can be written as

$$x = r\sin\theta\cos\phi, \qquad y = r\sin\theta\sin\phi, \qquad z = r\cos\theta \tag{3.2.1}$$

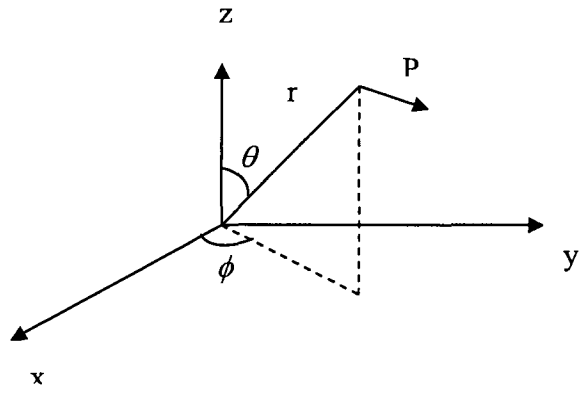

Fig.3.2-1 Cartesian Coordinate System $\{\hat{c}\}$ and Spherical Coordinate System $\{\hat{s}\}$

B. Coordinate Systems $\{\hat{c}'\}$ And $\{\hat{s}'\}$

$\{\hat{c}'\}$ and $\{\hat{s}'\}$ are Cartesian and spherical coordinate systems, respectively. The origin is located at the centre of the n-th slot. The x axis is along the length of the slot. The location of the observation point P can be described in $\{\hat{c}'\}$ and $\{\hat{s}'\}$ as (x', y', z') and (r', θ', ϕ'), respectively, as shown in Fig.3.2-2

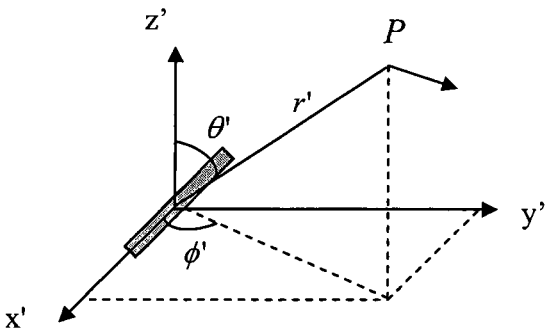

Fig.3.2-2 Cartesian Coordinate System $\{\hat{c}'\}$ and Spherical Coordinate System $\{\hat{s}'\}$

C. Coordinate Systems $\{\hat{c}''\}$ And $\{\hat{s}''\}$

$\{\hat{c}''\}$ and $\{\hat{s}''\}$ are Cartesian and spherical coordinate systems. The origin is at the centre of the n-th slot. The x'' axis is parallel to x. The location of point P in $\{\hat{c}''\}$ and $\{\hat{s}''\}$ are expressed as (x'', y'', z'') and (r'', θ'', ϕ'') in the two coordinate systems. Figs.3.2-3 and 3.2-4 summarize how the three Cartesian coordinate systems $\{\hat{c}\}$, $\{\hat{c}'\}$ and $\{\hat{c}''\}$ are related.

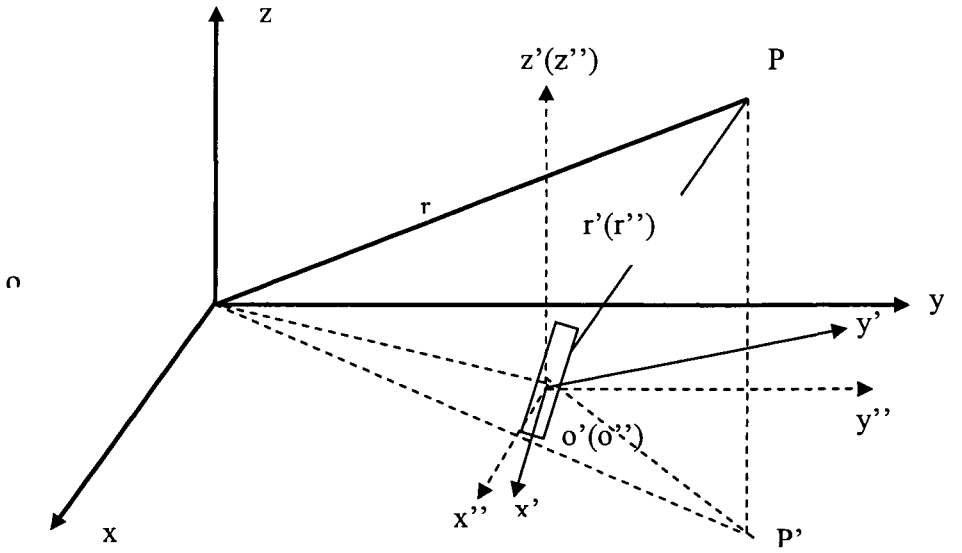

Fig.3.2-3 Cartesian Coordinate System $\{\hat{c}'\}$ and Spherical Coordinate System - 3D View

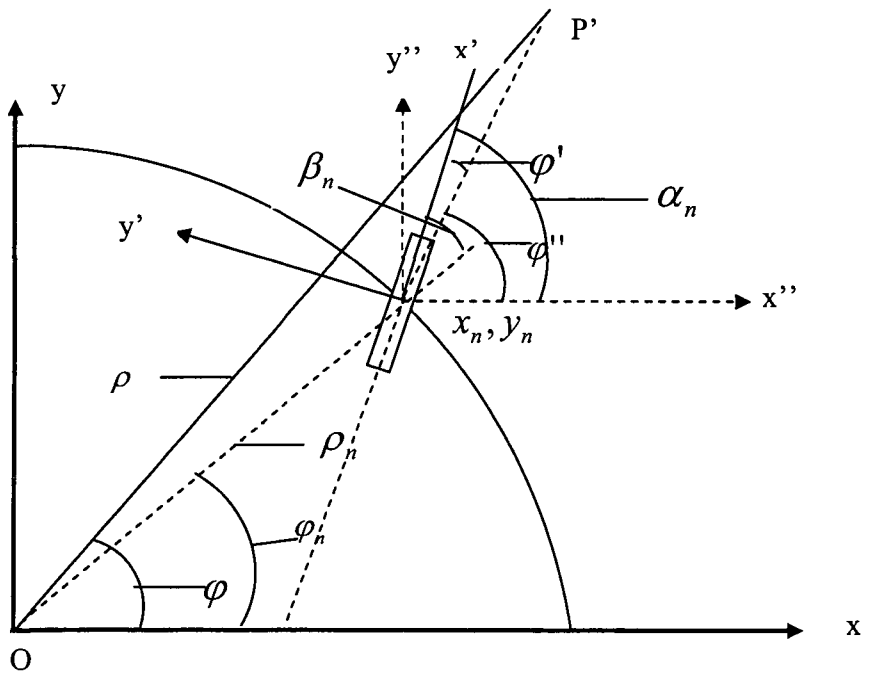

Fig.3.2-4 Cartesian Coordinate System $\{\hat{c}'\}$ and Spherical Coordinate System - 2D Projection Onto The xy-Plane

D. Relationships Between The Various Coordinate Systems

Point P' is the projection of the observation point P. Point (x_n, y_n) is the location of the n-th slot in $\{\hat{c}\}$. The same location is denoted (ρ_n, φ_n) in $\{\hat{s}\}$. Quantity α_n is the angle between the x' axis and the x'' axis, measured from x'' to x'. Quantity β_n is the tilt angle of the n-th slot measured between the x' axis and the radial direction.

Inspection of From Fig.3.2-3 and Fig.3.2-4 shows that

$$x'' = x - x_n \tag{3.2.2}$$

$$y'' = y - y_n \tag{3.2.3}$$

$$z'' = z - z_n \tag{3.2.4}$$

$$r'' = r' \tag{3.2.5}$$

$$z' = z \tag{3.2.6}$$

$$x_n = \rho_n \cos\varphi_n \tag{3.2.7}$$

$$y_n = \rho_n \sin\varphi_n \tag{3.2.8}$$

and so

$$\begin{aligned} r' = r'' &= \sqrt{(x-x_n)^2 + (y-y_n)^2 + (z-z_n)^2} \\ &= \sqrt{(r\sin\theta\cos\varphi - \rho_n\cos\varphi_n)^2 + (r\sin\theta\sin\varphi - \rho_n\sin\varphi_n)^2 + r^2\cos^2\theta} \end{aligned} \tag{3.2.9}$$

From Fig.3.2-4 we see that $\alpha_n = \varphi'' - \varphi'$. Now

$$tg\varphi'' = \frac{y''}{x''} = \frac{r\sin\theta\sin\varphi - \rho_n\sin\varphi_n}{r\sin\theta\cos\varphi - \rho_n\cos\varphi_n},$$

and so

$$\varphi' = tg^{-1}\left(\frac{r\sin\theta\sin\varphi - \rho_n\sin\varphi_n}{r\sin\theta\cos\varphi - \rho_n\cos\varphi_n}\right) - \alpha_n \tag{3.2.10}$$

Therefore α_n can be expressed by β_n and φ_n, which are determined by the location of the n-th slot in Fig(3.2-4), as

$$\alpha_n = \varphi_n + \beta_n \tag{3.2.11}$$

In our specific design the value of β_n will be the same for all slots. Using (3.2.10) and (3.2.11) we can obtain an expression for φ' in terms of r, θ, ϕ, φ_n *and* β_n as

$$\varphi' = tg^{-1}\left(\frac{r\sin\theta\sin\varphi - \rho_n\sin\varphi_n}{r\sin\theta\cos\varphi - \rho_n\cos\varphi_n}\right) - \varphi_n - \beta_n \tag{3.2.12}$$

We can also obtain θ' in terms of r, θ, ϕ. We recognize that

$$\cos\theta' = \frac{z'}{r'} = \frac{r\cos\theta}{\sqrt{(r\sin\theta\cos\varphi - \rho_n\cos\varphi_n)^2 + (r\sin\theta\sin\varphi - \rho_n\sin\varphi_n)^2 + r^2\cos^2\theta}} \tag{3.2.13}$$

and hence have

$$\theta' = \cos^{-1}\left(\frac{r\cos\theta}{\sqrt{(r\sin\theta\cos\varphi - \rho_n\cos\varphi_n)^2 + (r\sin\theta\sin\varphi - \rho_n\sin\varphi_n)^2 + r^2\cos^2\theta}}\right) \tag{3.2.14}$$

If $\vec{E}(r, \theta, \phi)$ is the electric field of the n-th slot with its components expressed in the $\{\hat{s}\}$ coordinate system, and $\vec{E}'(r', \theta', \phi')$ the same field with its components expressed in the $\{\hat{s}'\}$ coordinate system, we can use the transformation method in [1] to find the relation between $\vec{E}(r, \theta, \phi)$ and $\vec{E}'(r', \theta', \phi')$. This gives

$$\begin{Bmatrix} E_r(r,\theta,\varphi) \\ E_\theta(r,\theta,\varphi) \\ E_\varphi(r,\theta,\varphi) \end{Bmatrix} = [{}^{S}T^{C}][{}^{C}A^{C'}][{}^{C'}T^{S'}] \begin{Bmatrix} E'_{r'}(r',\theta',\varphi') \\ E'_{\theta'}(r',\theta',\varphi') \\ E'_{\varphi'}(r',\theta',\varphi') \end{Bmatrix} = [K] \begin{Bmatrix} E'_{r'}(r',\theta',\varphi') \\ E'_{\theta'}(r',\theta',\varphi') \\ E'_{\varphi'}(r',\theta',\varphi') \end{Bmatrix} \tag{3.2.15}$$

where $E_r(r,\theta,\phi)$, $E_\theta(r,\theta,\phi)$ are $E_\varphi(r,\theta,\phi)$ are the three components of $\vec{E}(r,\theta,\phi)$ in $\{\hat{s}\}$, and $E'_{r'}(r',\theta',\phi')$, $E'_{\theta'}(r',\theta',\phi')$, $E'_{\varphi'}(r',\theta',\phi')$ are the three components of $\vec{E}'(r',\theta',\phi')$ in $\{\hat{s}'\}$. The composite transformation matrix $[K]$ is given by

$$[K]=[{}^{S}T^{C}][{}^{C}A^{C'}][{}^{C'}T^{S'}] \tag{3.2.16}$$

with $[{}^{S}T^{C}]$, $[{}^{C}A^{C'}]$ and $[{}^{C'}T^{S'}]$ the partial transformation matrices [1]

$$[{}^{S}T^{C}]=\begin{Bmatrix}\sin\theta\cos\varphi & \sin\theta\sin\varphi & \cos\theta\\ \cos\theta\cos\varphi & \cos\theta\sin\varphi & -\sin\theta\\ -\sin\varphi & \cos\varphi & 0\end{Bmatrix} \tag{3.2.17}$$

$$[{}^{C'}T^{S'}]=\begin{Bmatrix}\sin\theta'\cos\varphi' & \cos\theta'\cos\varphi' & -\sin\varphi'\\ \sin\theta'\sin\varphi' & \cos\theta'\sin\varphi' & \cos\varphi'\\ \cos\theta' & -\sin\theta' & 0\end{Bmatrix} \tag{3.2.18}$$

and

$$[{}^{C'}A^{C}]=\begin{Bmatrix}\cos\gamma & \sin\gamma & 0\\ -\sin\gamma & \cos\gamma & 0\\ 0 & 0 & 1\end{Bmatrix}\begin{Bmatrix}1 & 0 & 0\\ 0 & \cos\beta & \sin\beta\\ 0 & -\sin\beta & \cos\beta\end{Bmatrix}\begin{Bmatrix}\cos\alpha & \sin\alpha & 0\\ -\sin\alpha & \cos\alpha & 0\\ 0 & 0 & 1\end{Bmatrix} \tag{3.2.19}$$

In (3.2.19) the α, β and γ are the Eulerian angles [1]. In our case, all the slots lie in the xy-plane, and ones finds that as a result we have $\alpha=\alpha_n$, $\beta=0$, $\gamma=0$, so that $[{}^{C'}A^{C}]$ simplifies to

$$[{}^{C'}A^{C}]=\begin{Bmatrix}\cos\alpha_n & \sin\alpha_n & 0\\ -\sin\alpha_n & \cos\alpha_n & 0\\ 0 & 0 & 1\end{Bmatrix} \tag{3.2.20}$$

It follows that

$$[{}^{C}A^{C'}]=[{}^{C'}A^{C}]^{-1}=[{}^{C'}A^{C}]^{t} \tag{3.2.21}$$

Using (3.2.20) and (3.2.21), we can express $[{}^{C}A^{C'}]$ as

$$[{}^{C}A^{C'}] = \begin{Bmatrix} \cos\alpha_n & -\sin\alpha_n & 0 \\ \sin\alpha_n & \cos\alpha_n & 0 \\ 0 & 0 & 1 \end{Bmatrix} \tag{3.2.22}$$

3.3 FAR-ZONE FIELDS OF AN ARBITARILY LOCATED AND ORIENTED SINGLE SLOT

Next we consider one of the slots (the n-th slot) in the array antenna. The length of this slot L_n and its width W_n. Since $W_n << L_n$ the aperture distribution over the slot can to a good approximation be expressed as

$$\vec{E}_{an} = \hat{a}_{y'} E_{0n} \cos\left(\frac{\pi}{L_n} x_n'\right) \tag{3.3.1}$$

where x'_n is a variable, $-L_n/2 \le x'_n \le L_n/2$, and E_{0n} is the amplitude of the aperture field at the n-th slot. The slot is located in a conducting groundplane, and so its far-zone radiation pattern can be written (excluding the distance-dependent terms) in coordinate system $\{\hat{s}'\}$ as [2,3]

$$E'^{n}_{r'} = 0 \tag{3.3.2}$$

$$E'^{n}_{\theta'} = -\frac{\pi}{2} C_n \sin\varphi' \frac{\cos X_n}{(X_n)^2 - (\frac{\pi}{2})^2} \frac{\sin Y_n}{Y_n} \tag{3.3.3}$$

$$E'^{n}_{\varphi'} = -\frac{\pi}{2} C_n \cos\theta' \cos\varphi' \frac{\cos X_n}{(X_n)^2 - (\frac{\pi}{2})^2} \frac{\sin Y_n}{Y_n} \tag{3.3.4}$$

where

$$X_n = \frac{kL_n}{2} \sin\theta' \cos\varphi' \tag{3.3.5}$$

$$Y_n = \frac{kW_n}{2}\sin\theta'\sin\varphi' \tag{3.3.6}$$

and

$$C_n = j\frac{L_n W_n k E_{0n} e^{-jkr'}}{2\pi r'} \tag{3.3.7}$$

In the far-zone of the slot $r >> \rho_n$, and so [90] we use the simplification

$$r' = r \qquad \text{for amplitude variations} \tag{3.3.8}$$

$$r' = r - \rho_n \sin\theta\cos(\varphi - \varphi_n) \qquad \text{for phase variations} \tag{3.3.9}$$

If we apply (3.3.8) and (3.3.9) we obtain

$$\theta' = \theta \tag{3.3.10}$$

and

$$\varphi' = \varphi - \alpha_n = \varphi - \varphi_n - \beta_n \tag{3.3.11}$$

Substitution of (3.3.10) and (3.3.11) into (3.2.18) gives

$$[{}^{C'}T^{S'}] = \begin{Bmatrix} \sin\theta\cos(\varphi-\alpha_n) & \cos\theta\cos(\varphi-\alpha_n) & -\sin(\varphi-\alpha_n) \\ \sin\theta\sin(\varphi-\alpha_n) & \cos\theta'\sin(\varphi-\alpha_n) & \cos(\varphi-\alpha_n) \\ \cos\theta & -\sin\theta & 0 \end{Bmatrix} \tag{3.3.12}$$

After the multiplication of the three matrices $[{}^{S}T^{C}]$, $[{}^{C}A^{C'}]$, and $[{}^{C'}T^{S'}]$ we find that

$$[K] = [{}^{S}T^{C}][{}^{C}A^{C'}][{}^{C'}T^{S'}] = 1 \tag{3.3.13}$$

Thus (3.2.15) simplifies to

$$\begin{Bmatrix} E_r(r,\theta,\varphi) \\ E_\theta(r,\theta,\varphi) \\ E_\varphi(r,\theta,\varphi) \end{Bmatrix} = \begin{Bmatrix} E'_{r'}(r',\theta',\varphi') \\ E'_{\theta'}(r',\theta',\varphi') \\ E'_{\varphi'}(r',\theta',\varphi') \end{Bmatrix} \tag{3.3.14}$$

What (3.2.22) shows is that after we use the far field assumption (3.3.8) and (3.3.9), the field expressed in $\{\hat{s}\}$ will be the same as in $\{\hat{s}'\}$. Thus (3.3.3) and (3.3.4) expressed in coordinate system $\{\hat{s}\}$, once more with the distance terms suppressed, are

$$E^n{}_\theta(\theta,\varphi) = -\frac{1}{2}C_n \sin(\varphi - \varphi_n - \beta_n)\frac{\cos X_n}{(X_n)^2 - (\frac{\pi}{2})^2}\frac{\sin Y_n}{Y_n} \tag{3.3.15}$$

and

$$E^n{}_\varphi(\theta,\varphi) = -\frac{1}{2}C_n \cos\theta\cos(\varphi - \varphi_n - \beta_n)\frac{\cos X_n}{(X_n)^2 - (\frac{\pi}{2})^2}\frac{\sin Y_n}{Y_n} \tag{3.3.16}$$

where

$$X_n = \frac{kL_n}{2}\sin\theta\cos(\varphi - \varphi_n - \beta_n) \tag{3.3.17}$$

$$Y_n = \frac{kW_n}{2}\sin\theta\sin(\varphi - \varphi_n - \beta_n) \tag{3.3.18}$$

and

$$C_n = j\frac{L_n W_n k E_{0n} e^{-jk(r-\rho_n \sin\theta\cos(\varphi-\varphi_n))}}{2\pi r} \tag{3.3.19}$$

3.4 FAR-ZONE FIELDS OF AN M-SLOT ARRAY OF ARBITARILY LOCATED AND ORIENTED SLOTS

Since we have the far-field expressions for n-th slot in (3.3.15) and (3.3.16), we can write the radiation pattern for a complete array of M arbitrarily oriented and located slots, in the coordinate system $\{\hat{s}\}$, as

$$E_\theta(r,\theta,\varphi)=\sum_{n=1}^{M}E_\theta^n(r,\theta,\varphi)=\frac{e^{-jkr}}{r}\sum_{n=1}^{M}E_\theta^n(\theta,\varphi)=\frac{e^{-jkr}}{r}E_{F\theta}(\theta,\varphi) \tag{3.4.1}$$

and

$$E_\varphi(r,\theta,\varphi)=\sum_{n=1}^{M}E_\varphi^n(r,\theta,\varphi)=\frac{e^{-jkr}}{r}\sum_{n=1}^{M}E_\varphi^n(\theta,\varphi)=\frac{e^{-jkr}}{r}E_{F\varphi}(\theta,\varphi) \tag{3.4.2}$$

where

$$E_{F\theta}(\theta,\varphi)=-\frac{1}{2}jk\sum_{n=1}^{M}L_nW_nE_{0n}e^{jk\rho_n\sin\theta\cos(\varphi-\varphi_n)}\sin(\varphi-\varphi_n-\beta_n)\frac{\cos X_n}{(X_n)^2-(\frac{\pi}{2})^2}\frac{\sin Y_n}{Y_n} \tag{3.4.3}$$

and

$$E_{F\varphi}(\theta,\varphi)=-\frac{1}{2}jk\sum_{n=1}^{M}L_nW_nE_{0n}e^{jk\rho_n\sin\theta\cos(\varphi-\varphi_n)}\cos\theta\cos(\varphi-\varphi_n-\beta_n)\frac{\cos X_n}{(X_n)^2-(\frac{\pi}{2})^2}\frac{\sin Y_n}{Y_n} \tag{3.4.4}$$

3.5 SLOT LAYOUTS FOR RLSA ANTENNAS

3.5.1 Slot-Pair Arrangement

In the case of the RLSA antenna the radiating element unit is a slot-pair. The relative orientation, and distance between, each member of a specific slot-pair, as well as the location and orientation of the slot-pairs relative to all other such slot-pairs, determines the polarization of the

RLSA antenna. There are three kinds of slot-pair arrangements that are used. We discuss these here; it complements the statements made in Section 1.3.

3.5.2 Circularly Polarized RLSA Antennas

A. Circular Polarization Requirement #1

In order to obtain circularly polarized radiation (observed on boresight) from a slot-pair the electric fields over the individual slot apertures should be spatially orthogonal to each other, and have the same amplitude but relative phase of 90°. This is achieved by placing the constituent slots of a slot-pair spatially orthogonal to each other, separating them by one quarter of wavelength measured along the radial direction to get the 90 degree phase difference, and tilting both slots so that each is at $\pm 45^{\circ}$ to the incident wave in the radial waveguide so that they will have the same excitation.

B. Circular Polarization Requirement #2

In order for the complete RLSA antenna to produce a circularly polarized pattern, slot-pairs geometrically rotated by φ should obtain the same amount of electrical phase advance [4]. This is achieved by using one of two kinds of aperture arrangement, depending on which type of traveling wave[7] is extant in the in radial waveguide :

(a).**Spiral aperture arrangement with TEM mode excitation** [4] : The necessary arrangement with TEM mode excitation is determined in the following discussion. The magnetic field of the TEM mode in the radial waveguide can be written as

[7] As discussed in Sections 2.2 and 2.3.

$$H_{\varphi} = H_1^{(1)}(k\rho) \tag{3.5.1}$$

where $H_1^{(1)}(k\rho)$ is the Hankel function, $k = 2\pi / \lambda_g$, λ_g is the wavelength in the radial waveguide, and ρ is radial distance. Assuming that slot pair#1 and slot pair#2 are two adjacent slot pairs of the RLSA antenna, (ρ_1, φ_1) is the polar coordinate for the centre of slot pair#1 and (ρ_2, φ_2) is the polar coordinate for the centre of slot pair#2, as shown in Fig. 3.5-1.

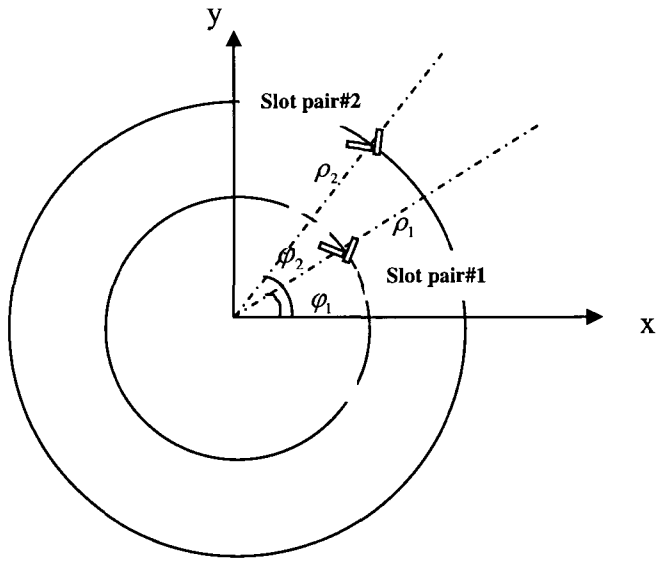

Fig. 3.5-1 : Slot Arrangement For Circular Polarization (After [4])

To satisfy requirement#2, the phase difference between any two adjacent slot pairs must be equal to $\varphi_2 - \varphi_1$, which condition can be expressed as

$$\varphi_2 - \varphi_1 = \arg(H_1^{(1)}(k\rho_2)) - \arg(H_1^{(1)}(k\rho_1)) \tag{3.5.2}$$

If $k\rho >> 1$, the large argument form of the Hankel function allows us to use (3.5.2) to obtain the relation between ρ_1 and ρ_2 as

$$\rho_2 = (\varphi_2 - \varphi_1) \cdot \lambda_g / 2\pi + \rho_1 \tag{3.5.3}$$

This result indicates that the trace on which slot pairs are located is a kind of spiral. This aperture arrangement is shown is Fig.3.5-2

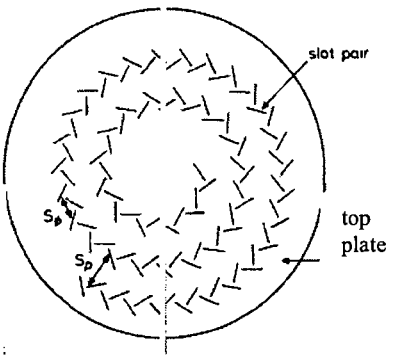

Fig.3.5-2 : Spiral Arrangement of Slots (After [4])

(b). Concentric aperture arrangement with rotating mode excitation : Using a rotating mode in the radial waveguide, we obtain a field with uniform amplitude along φ direction and linear phase change along φ direction. So the Requirement#2 will be satisfied by arranging the slot-pairs concentrically. One advantage is that the symmetry of the field in radial waveguide won't be disturbed by the slots arranged on the top plate.

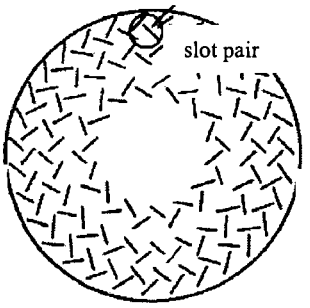

Fig.3.5-3 : Concentric Arrangement of Slots (After [5])

3.5.3 Linearly Polarized RLSA Antennas [5]

If we have a radially inward-propagating TEM traveling wave (which has rotational symmetry within the radial waveguide) that excites the radiating slots, the slot-pairs on the same ring will all be in phase. The excitation of the slot-pair will be proportional to

$$g = e^{jk_g\rho} \cdot \sin\theta \tag{3.5.4}$$

where θ is the angle between the slot line and the current flow line. Thus in Fig.3.5-4,

$$\beta_1 = e^{jk_g\rho_1} \cdot \sin\theta_1 \tag{3.5.5}$$

$$\beta_2 = e^{jk_g\rho_2} \cdot \sin\theta_2 \tag{3.5.6}$$

with β_1 and β_2 the excitation coefficients of slots #1 and #2.

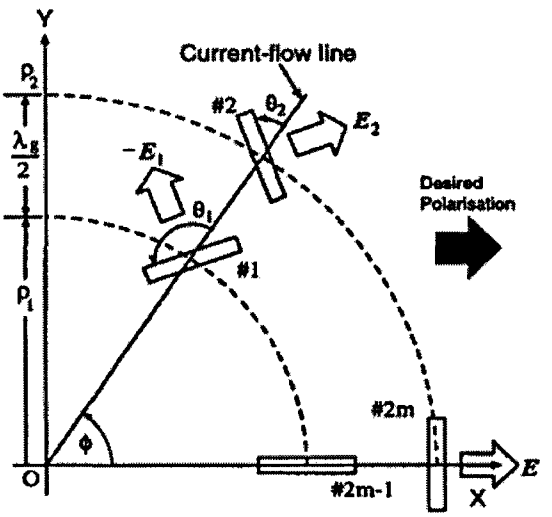

Fig. 3.5-4 Slot Arrangement for Linear Polarization

The radiation polarization is along x direction, so the co-polarization from #1 and #2 is

$$\beta_1 \sin(\theta_1 + \varphi) \text{ and } \beta_2 \sin(\theta_2 + \varphi) \tag{3.5.7}$$

The cross-polarization from #1 and #2 is

$$-\beta_1 \cos(\theta_1 + \varphi) \text{ and } -\beta_2 \cos(\theta_2 + \varphi) \tag{3.5.8}$$

For the amplitude, (3.5.5) and (3.5.6) can be normalized by $e^{jk_g\rho_1}$. The total radiation from the slot pair is polarized as

$$\sin\theta_1 \cdot \sin(\theta_1+\varphi)+\sin\theta_2 \sin(\theta_2+\varphi)=1 \qquad \text{for co-polarization} \qquad (3.5.9)$$

and

$$-\sin\theta_1 \cdot \cos(\theta_1+\varphi) \ -\sin\theta_2 \cos(\theta_2+\varphi)=0 \quad \text{for cross-polarization} \qquad (3.5.10)$$

Solving (3.5.9) and (3.5.10) simultaneously yields

$$\theta_1=\pi/2-\varphi/2 \qquad (3.5.11)$$

$$\theta_2=\pi-\varphi/2 \qquad (3.5.12)$$

These results indicate the following:

(1). A unit radiator consists of two slots radially spaced by a half-guide wavelength and perpendicular to each other.

(2). The slot at φ should be rotated by the angle $\varphi/2$ around its centre compared with its orientation at $\varphi=0$.

So for the arrangement in Fig.3.5-5, a uniform amplitude, uniform phase and x-polarized radiation will be obtained.

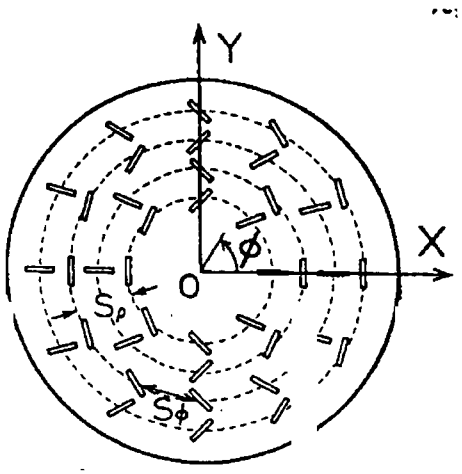

Fig. 3.5-5 : Aperture Arrangement With Linear Polarization Radiation

3.6 FAR-ZONE FIELDS OF AN RLSA ANTENNA

The radiating elements of most arrays are identical; the elements can be "made congruent" by a simple translation operation. The pattern multiplication principle applies and we can find the radiation patterns using expressions of the form

$$E_\theta(\theta,\varphi) = E_{\theta e}(\theta,\varphi) \times F(\theta,\varphi) \qquad (3.6.1)$$

$$E_\varphi(\theta,\varphi) = E_{\varphi e}(\theta,\varphi) \times F(\theta,\varphi) \qquad (3.6.2)$$

where $F(\theta,\varphi)$ is the scalar array factor. The polarization of the field pattern comes from the element factors $E_{\theta e}(\theta,\varphi)$ and $E_{\theta\varphi}(\theta,\varphi)$. In most practical applications, the elements are small, perhaps a half-wavelength long in their maximum dimension, in which case $E_{\theta e}(\theta,\varphi)$ and $E_{\theta\varphi}(\theta,\varphi)$ are broad patterns, and the fine structure in far-field pattern comes from the array factor $F(\theta,\varphi)$. In the case of the RLSA antenna the elements are not identical and the pattern multiplication principle unfortunately does not apply. However, we recognize that the RLSA

antenna elements can be made congruent by a translation plus a rotation. We will utilize this fact in what follows.

First consider radiating slot-pairs that are circularly polarized, at least in the boresight direction. Each slot-pair can be modelled as two ideal magnetic currents Ix and Iy which have the same amplitude but a 90 degree phase difference between them. Next consider the case where all the elements over the aperture are congruent by a simple translation, as shown in Fig.3.6-1. The total E -field will be the form in (3.6.1) and (3.6.2). The element of the far fields $E_{\theta e}(\theta,\varphi)$ and $E_{\theta\varphi}(\theta,\varphi)$ will be circularly polarized patterns that determine the polarization of the complete antenna.

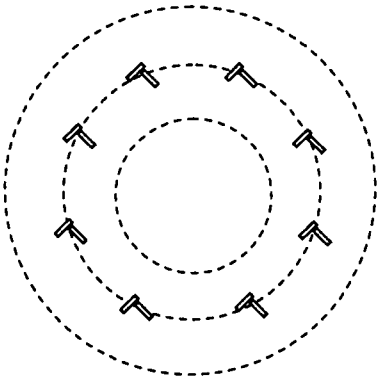

Fig.3.6-1 Arrangement of Antenna Array with Similarly Oriented Radiation Elements

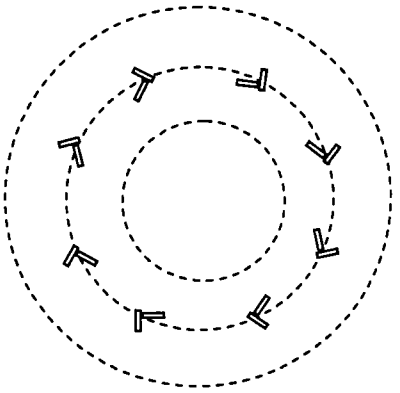

Fig. 3.6-2 Concentric Arrangement of RLSA Antenna

Next consider the aperture layout shown in Fig.3.6-2. Each slot-pair has the same angle with respect to the radial line that passes through that slot-pair. In order to find the resulting pattern of the complete array of eight slot-pairs in Fig.3.6-2 we consider a radiating slot-pair whose magnetic currents are denoted by $I^a_{mn}\,\hat{x}_n$ and $I^b_{mn}\,\hat{y}_n$, as indicated in Fig.3.6-3.

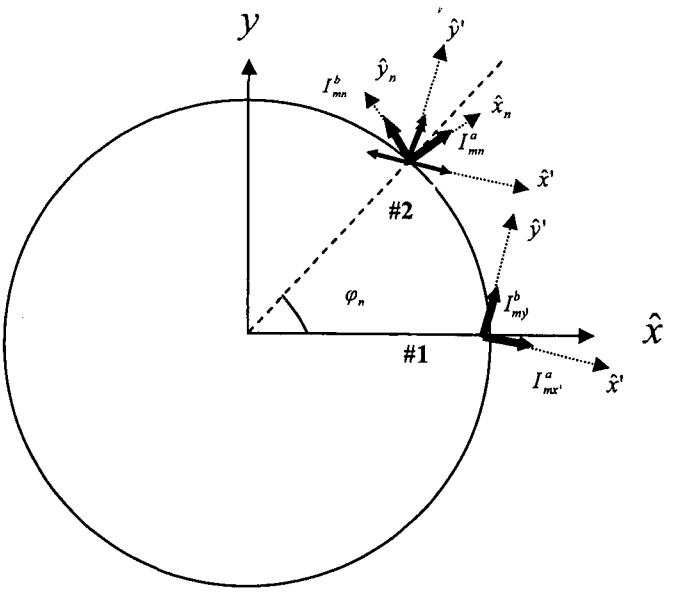

Fig.3.6-3 Arrangement Relationship of Two Slot Pairs on m-th Ring of RLSA Antenna

Here n and m indicate the location of element#2 on the aperture, namely the n-th element on the m-th ring. The centre of this element is at (ρ_m, φ_n). For simplification, there is an imaginary element#1on the x-axis; its centre is on the m-th ring, and its location is $(\rho_m, 0)$. Each element has the same angle with respect to its own radial direction. Element#2 can be obtained by rotating element#1 an angle φ_n. Quantities x' and y' are local coordinate axes on element#1. The

magnetic currents of this slot-pair are $I_m^a\ \hat{x}'$ and $I_m^b\ \hat{y}'$. Element#1 has a φ_n phase delay relative to element#2. The relation between I_m^a, I_{mn}^a, I_m^b and I_{mn}^b can be written as

$$I_{mn}^a = I_m^a e^{-j\varphi_n} \tag{3.6.3}$$

$$I_{mn}^b = jI_{mn}^a \tag{3.6.4}$$

and

$$I_m^b = jI_m^a \tag{3.6.5}$$

The components of $I_{mn}^a\ \hat{x}_n$ and $I_{mn}^b\ \hat{y}_n$ on x' and y' are

$$I_{mnx'}^a = I_{mn}^a \cos\varphi_n \qquad I_{mny'}^a = -I_{mn}^a \sin\varphi_n \tag{3.6.6}$$

$$I_{mnx'}^b = I_{mn}^b \sin\varphi_n \qquad I_{mny'}^b = I_{mn}^b \cos\varphi_n \tag{3.6.7}$$

The currents $I_{mn}^a\ \hat{x}_n$ and $I_{mn}^b\ \hat{y}_n$ in the x'y' coordinate system are

$$I_{mn}^a\ \hat{x}_n = I_{mnx'}^a \hat{x}' + I_{mny'}^a \hat{y} = I_{mn}^a \cos\varphi_n \hat{x}' - I_{mn}^a \sin\varphi_n \hat{y}' \tag{3.6.8}$$

$$I_{mn}^b\ \hat{y}_n = I_{mnx'}^b \hat{x}' + I_{mny'}^b \hat{y} = jI_{mn}^a \sin\varphi_n \hat{x}' + jI_{mn}^a \cos\varphi_n \hat{y}' \tag{3.6.9}$$

and

$$I_{mn}^a\ \hat{x}_n + I_{mn}^b\ \hat{y}_n = I_{mn}^a[(\cos\varphi_n + j\sin\varphi_n)\hat{x}'_n + j(\cos\varphi_n + j\sin\varphi_n)\hat{y}'_n] \tag{3.6.10}$$

Expression (3.6.10) can be rewritten using $e^{j\varphi_n} = \cos\varphi_n + j\sin\varphi_n$ and (3.6.7) as

$$I_{mn}^a\ \hat{x}_n + I_{mn}^b\ \hat{y}_n = I_{mn}^a e^{j\varphi_n}(\hat{x}'_n + j\hat{y}'_n) = I_m^a e^{-j\varphi_n} e^{j\varphi_n}(\hat{x}'_n + j\hat{y}'_n) = I_m^a(\hat{x}'_n + j\hat{y}'_n) \tag{3.6.11}$$

which is the same as the total magnetic current of the imaginary slot-pair located on the x-axis. Yet the n-th unit is an arbitrary unit on m-th ring. Thus (3.6.11) tells us that the magnetic currents on each slot-pair on the m-th ring have the same magnetic current (amplitude, phase and direction) as the imaginary slot-pair, and so each slot-pair on m-th ring can be considered as the

imaginary slot-pair translated to its specific location. Thus for the aperture layout shown in Fig.3.6-2 can write the field radiated by the collection of slot-pairs in the form (3.6.1) and (3.6.2) after all. In fact, although we considered just a single ring, because of the slot-pair orientations, we can use the "pattern multiplication form" (3.6.1) and (3.6.2) for the complete array of several rings.

The question remains as to what element pattern we must use for the slot-pair. In (3.6.1) and (3.6.2) the element pattern is that is for an element located at the centre of the antenna, as shown in Fig.3.6.4.

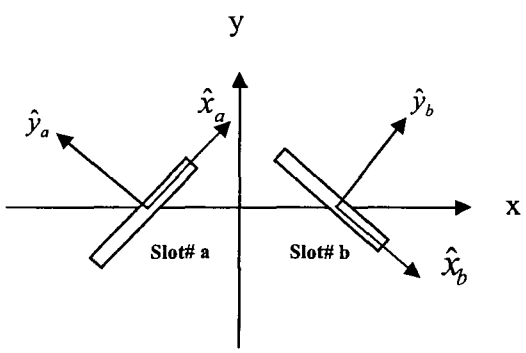

Fig.3.6.4 : Radiation Unit Located at the Centre of Antenna

The centre positions of slot#a and slot#b are $(-\lambda_g/8, 0)$ and $(\lambda_g/8, 0)$. The element pattern of the slot-pair is then

$$E_{\theta e} = -\frac{\pi}{2}C^a \sin(\varphi - \frac{\pi}{4})\frac{\cos X^a}{(X^a)^2 - (\frac{\pi}{2})^2}\frac{\sin Y^a}{Y^a} - j\frac{\pi}{2}C^b \sin(\varphi + \frac{\pi}{4})\frac{\cos X^b}{(X^b)^2 - (\frac{\pi}{2})^2}\frac{\sin Y^b}{Y^b} \qquad (3.6.12)$$

and

$$E_{\varphi e} = -\frac{\pi}{2} C^a \cos\theta \cos(\varphi - \frac{\pi}{4}) \frac{\cos X^a}{(X^a)^2 - (\frac{\pi}{2})^2} \frac{\sin Y^a}{Y^a} - j\frac{\pi}{2} C^b \cos\theta \cos(\varphi + \frac{\pi}{4}) \frac{\cos X^b}{(X^b)^2 - (\frac{\pi}{2})^2} \frac{\sin Y^b}{Y^b} \quad (3.6.13)$$

where

$$X^a = \frac{kL}{2} \sin\theta \cos(\varphi - \frac{\pi}{4}) \quad (3.6.14)$$

$$Y^a = \frac{kW}{2} \sin\theta \sin(\varphi - \frac{\pi}{4}) \quad (3.6.15)$$

$$X^b = \frac{kL}{2} \sin\theta \cos(\varphi + \frac{\pi}{4}) \quad (3.6.16)$$

$$Y^b = \frac{kW}{2} \sin\theta \sin(\varphi + \frac{\pi}{4}) \quad (3.6.17)$$

$$C^a = j\frac{LWkE_{0a} e^{-jkr} e^{jk\rho_0 \sin\theta \cos(\varphi - \pi)}}{2\pi r} \quad (3.6.18)$$

$$C^b = j\frac{LWkE_{0b} e^{-jkr} e^{jk\rho_0 \sin\theta \cos(\varphi - 0)}}{2\pi r} \quad (3.6.19)$$

and

$$\rho_0 = \frac{\lambda_g}{8} \quad (3.6.20)$$

$$E_{0a} = jE_{0b} \quad (3.6.21)$$

Superscripts "a" and "b" identify the slot "a" and slot "b" of the radiating element pair. The far-zone fields of the entire RLSA antenna are then

$$E_\theta(\theta,\varphi) = E^m{}_{\theta e}(\theta,\varphi) \sum_{m=1}^{M} \sum_{n=1}^{N_m} I_m \cos(k\rho_m \cos\frac{(2n-1)\pi}{N_m} \sin\theta\cos\phi) \times \cos(k\rho_m \cos\frac{(2n-1)\pi}{N_m} \sin\theta\sin\phi) \quad (3.6.22)$$

and

$$E_{\varphi}(\theta,\varphi) = E^{m}{}_{\varphi e}(\theta,\varphi)\sum_{m=1}^{M}\sum_{n=1}^{N_m} I_m \cos(k\rho_m \cos\frac{(2n-1)\pi}{N_m}\sin\theta\cos\phi) \times \cos(k\rho_m \cos\frac{(2n-1)\pi}{N_m}\sin\theta\sin\phi) \tag{3.6.23}$$

The co-polarized and cross-polarized circularly-polarized fields are then obtained using (3.6.22) and (3.6.23) as

$$E_R(\theta,\varphi) = \frac{1}{\sqrt{2}}(E_\theta(\theta,\varphi) + jE_\varphi(\theta,\varphi)) \tag{3.6.24}$$

and

$$E_L(\theta,\varphi) = \frac{1}{\sqrt{2}}(E_\theta(\theta,\varphi) - jE_\varphi(\theta,\varphi)) \tag{3.6.25}$$

3.7 CONCLUSIONS

This chapter has determined the detailed expressions needed to compute the vector radiation patterns of an RLSA. It was shown that, although the elements of an RLSA antenna are not identical, it is still possible to use a pattern multiplication principle to find the radiation pattern due to the fact that the radiating slot-pairs all have the same angle with respect to the local radial line. Although this is probably known by those working in the area of RLSA antennas, it is not actually stated anywhere. Now that we are able to compute the radiation pattern of the RLSA antenna we can proceed to the development of a synthesis procedure in Chapter 4.

3.8 REFERENCES FOR CHAPTER 3

[1] Y. Rahmat-Samii, "Useful Coordinate Transformation for antenna applications", *IEEE Trans. Antennas Propagat.*, vol. AP-27, no. 4, Jul. 1979.

[2] R. S. Elliott, *Antenna Theory and Design* (Prentice-Hall, 1981).

[3] C. A. Balanis, *Antenna Theory, Analysis and Design* (Wiley, 1997) 2nd Edition.

[4] M. Ando, K. Sakurai, N. Goto, K. Arimura and Y. Ito, "A Radial Line Slot Antenna for 12 GHz Satellite TV Reception" , *IEEE Trans. Antennas Propagat.*, vol. AP-33, no. 12, pp. 1347-1353, Dec.1985.

[5] M. Ando, T. Numata, J. Takada, and N. Goto, "A linearly polarized radial line slot antenna", *IEEE Trans. Antennas Propagat.*, vol. 36, no. 12, pp. 1675-1680, Dec. 1988.

CHAPTER 4

Radiation Pattern Synthesis Technique for Radial Line Slot Antennas

4.1 INTRODUCTION

In order to design an RLSA antenna with the desired radiation pattern we must first perform a synthesis to determine the required aperture distribution. The unsuitability of existing synthesis techniques was briefly discussed in Section 1.4. In this chapter we therefore develop a hybrid synthesis method that can be used for RLSA antennas, and in particular for RLSA antennas with isoflux radiation patterns. It is a "hybrid" synthesis method in that it consists of the following steps :

Step#1 - Find a continuous scalar circular aperture distribution which can give the desired relative power pattern. This is covered in Section 4.2.

Step#2 - Use conventional sampling to yield the complex excitations of a circular-aperture planar array of isotropic elements that will approximate the desired pattern. This is the subject of Section 4.3.

Step#3 - Using the results from Step#2, optimize the location[8] and the excitation of the elements to obtain the desired pattern with the smallest ripples. Section 4.4 outlines this part of the overall synthesis procedure.

Step#4 - Using the results from Step#3, optimize the full vector radiation pattern. This final step is discussed in Section 4.5.

[8] The reason for altering the locations of the radiating elements is discussed in Section 4.4.1.

In Sections 4.2 through 4.5 the synthesis procedure that has been developed is described via a specific example, namely an isoflux pattern[9] with an EOC angle of roughly 59°. In Section 4.6 we show that the synthesis approach can be applied to other radiation pattern requirements as well. Section 4.7 concludes the chapter.

4.2 STEP#1 – SYNTHESIS OF A CONTINUOUS CIRCULAR APERTURE DISTRIBUTION SATISFYING THE PATTERN REQUIREMENTS

4.2.1 Radiation Pattern Specifications

The hybrid synthesis method that has been developed in this thesis is best demonstrated by means of an example. The example chosen is that of the isoflux pattern shown in Fig. 1.1-3 for the 800km altitude satellite, at 19 GHz and with circular polarization.

4.2.2 Circular Taylor Pattern

We treat the RLSA antenna as an aperture antenna, and extend Taylor's circular aperture synthesis technique to a pattern exhibiting our desired shape (in this case that in Fig.1.1-3) with controlled ripple surrounded by ring side lobes with controlled heights [1].

Let us first consider the circular Taylor pattern. A planar aperture with a circular boundary of radius a is sketched in Fig.4.2-1.

[9] This is simply meant to illustrate the use of the synthesis method at this stage. RLSA antennas with isoflux patterns will be discussed more generally in Chapter 5.

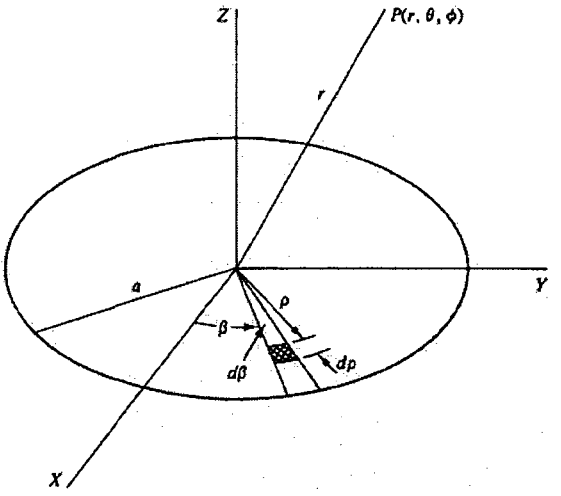

Fig.4.2-1 Circular Aperture Antenna

If $K(\rho,\beta)$ is the aperture distribution, the pattern is [1]

$$F(\theta,\phi) = \int_0^{2\pi} \int_0^a K(\rho,\beta) e^{jk\rho\sin\theta\cos(\phi-\beta)} \rho d\rho d\beta \qquad (4.2.1)$$

where $k = 2\pi/\lambda$. The aperture distribution can be represented by a Fourier series, and the term $e^{jk\rho\sin\theta\cos(\phi-\beta)}$ in (4.2.1) can be represented as a Bessel function expansion. Thus we can write

$$e^{jk\rho\sin\theta\cos(\phi-\beta)} = \sum_{m=-\infty}^{\infty} (j)^m J_m(k\rho\sin\theta) e^{jm(\phi-\beta)} \qquad (4.2.2)$$

and

$$K(\rho,\beta) = \sum_{n=-\infty}^{\infty} K_n(\rho) e^{jn\beta} \qquad (4.2.3)$$

So (4.2.1) can be rewritten as

$$F(\theta,\phi) = \sum_{m=-\infty}^{\infty} \sum_{n=-\infty}^{\infty} \int_0^{2\pi} \int_0^a K_n(\rho)(j)^m J_m(k\rho\sin\theta) e^{jm\phi} e^{j(n-m)\beta} \rho d\rho d\beta \qquad (4.2.4)$$

The β-integration in (4.2.4) only has a nonzero value when m = n, so that (4.2.4) simplifies to

$$F(\theta,\phi) = 2\pi \sum_{n=-\infty}^{\infty} \int_0^{2\pi} \int_0^a K_n(\rho)(j)^n J_n(k\rho\sin\theta) e^{jn\phi} \rho d\rho \qquad (4.2.5)$$

From (4.2.5), it can be deduced that if a ϕ-independent pattern is desired (as we wish to have for the isoflux pattern), n should be restricted to the value zero. In such a case (4.2.3) then shows that the aperture distribution has to be β-independent, of the form $K_0(\rho)$. The pattern is then given by

$$F(\theta) = 2\pi \int_0^a K_0(\rho) J_0(k\rho\sin\theta) \rho d\rho \qquad (4.2.6)$$

Expression (4.2.6) can be re-written as

$$F(u) = 2\pi \int_0^{\pi} p g_0(p) J_0(up) dp \qquad (4.2.7)$$

if we let

$$u = \frac{2a}{\lambda}\sin\theta \qquad (4.2.8a)$$

$$p = \frac{\pi}{a}\rho \qquad (4.2.8b)$$

and

$$g_0(p) = \frac{2a^2}{\pi} K_0(\rho) \qquad (4.2.8c)$$

If the circular aperture is uniformly excited, a condition that can be represented by $g_0(p) = 1$, (4.2.7) gives the sum pattern

$$F(u) = \frac{J_1(\pi u)}{\pi u} \qquad (4.2.9)$$

If the roots γ_{1m} of $J_1(u)$ are defined by

$$J_1(\pi\gamma_{1m}) = 0, m = 0,1,2,\ldots \tag{4.2.10}$$

then a modification of (4.2.9) can be written as

$$F(u) = \frac{J_1(\pi u)}{\pi u}) \frac{\prod_{n=1}^{\bar{n}-1} (1-u^2/u_n^2)}{\prod_{n=1}^{\bar{n}-1} (1-u^2/\gamma_{1n}^2)} \tag{4.2.11}$$

One can see from (4.2.11), the pattern can be modified by removing the first $\bar{n}-1$ roots of (4.2.10) and replace them by $\bar{n}-1$ roots at the new positions u_n.

To find the aperture distribution $g_0(p)$ that will produce the Taylor circular pattern, it is helpful to express $g_0(p)$ as a series in the form

$$g_0(p) = \sum_{m=0}^{\infty} B_m J_0(\gamma_{1m} p) \tag{4.2.12}$$

Substitution of (4.2.12) into (4.2.7) gives

$$B_m = \frac{2}{\pi^2} \frac{F(\gamma_{1m})}{J_0^2(\gamma_{1m}\pi)} \tag{4.2.13}$$

then we can write

$$g_0(p) = \frac{2}{\pi^2} \sum_{m=0}^{\infty} \frac{F(\gamma_{1m})}{J_0^2(\gamma_{1m}\pi)} J_0(\gamma_{1m} p) \tag{4.2.14}$$

$F(\gamma_{1m})$ is computed by (4.2.11).

From (4.2.14), if the roots u_m, m=1,2,...for some desired pattern (eg. isoflux in the present example) can be found, the aperture distribution can be obtained. The question is how to find the roots u_m, m=1,2,...for the desired pattern. Reference [1] gives a method to do this, which will be

discussed in what follows. A perturbation procedure is employed to transform the starting pattern (Taylor sum pattern) to the desired pattern.

4.2.3 Perturbation Procedure to Obtain a Desired Pattern

Elliott and Stern [1] give a perturbation procedure to find the roots u_m, m=1,2,...for a desired pattern. They first considered the special case of, $g_0(p) = 2$ for which case (4.2.7) yields

$$F_0(u) = \frac{2J_1(\pi u)}{\pi u} \tag{4.2.15}$$

Expression (4.2.15) gives a familiar pattern that is depicted in Fig.4.2-2, which is used as a starting pattern.

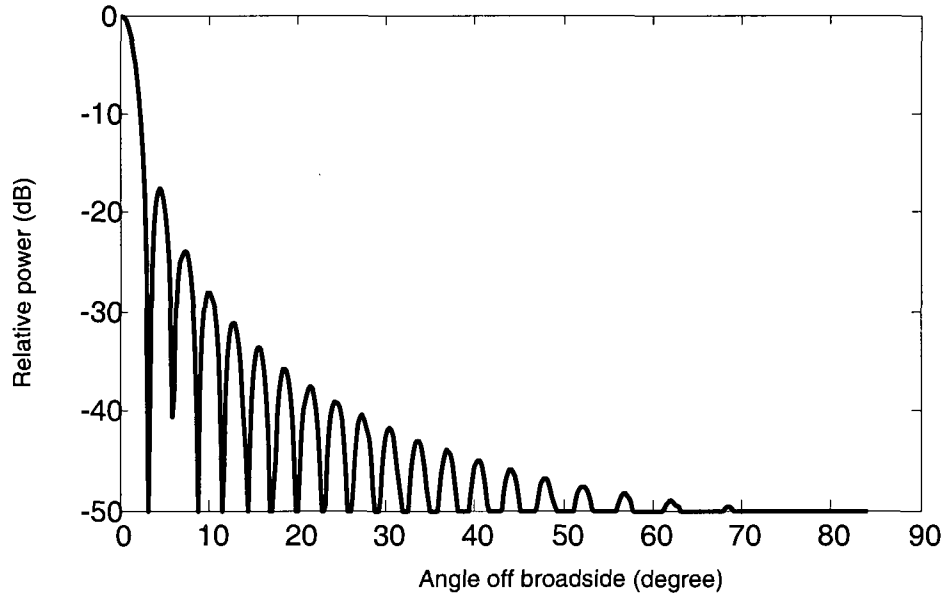

Fig.4.2-2 Array Factor Pattern for Uniformly Excited Circular Aperture

The pattern in Fig. 4.2.2 consists of a main beam plus a family of ring side lobes (the pattern is rotationally symmetric). The nulls in this pattern are given by $J_1(\pi\gamma_{1n}) = 0, n = 1,2,\ldots$. Next all

the roots $u_n = \gamma_{1n}$ for $n \geq \bar{n}$ are anchored, whereas the inner roots for $n = 1,2,\cdots,\bar{n}-1$ are moved to the new complex positions $u_n + j\upsilon_n \neq \gamma_{1n}$. The pattern in (4.2.11) then becomes

$$F(u) = f(u)\prod_{n=1}^{\bar{n}-1}\left[1-\frac{u^2}{(u_n+j\upsilon_n)^2}\right] \tag{4.2.16}$$

where

$$f(u) = 2\frac{J_1(\pi u)}{\pi u}\frac{1}{\prod_{n=1}^{\bar{n}-1}\left(1-\frac{u^2}{\gamma^2_{1n}}\right)} \tag{4.2.17}$$

We are usually interested in the relative power pattern. The power pattern expression with the new roots $u_n + j\upsilon_n \neq \gamma_{1n}$, $n = 1,2,\cdots,\bar{n}-1$ will be [1]

$$\begin{aligned} F(u)F^*(u) &= f^2(u)\prod_{n=1}^{\bar{n}-1}\left[1-\frac{u^2}{(u_n+j\upsilon_n)^2}\right]\times\left[1-\frac{u^2}{(u_n-j\upsilon_n)^2}\right] \\ &= f^2(u)\prod_{n=1}^{\bar{n}-1}\frac{u_n^4+\upsilon_n^4+u^4+2u_n^4\upsilon_n^2-2u^2u_n^2+2u^2\upsilon_n^2}{(u_n^{\ 2}+\upsilon_n^{\ 2})^2} \end{aligned} \tag{4.2.18}$$

As a consequence of this, the power pattern $G(u)$, expressed in dB, is given by

$$\begin{aligned} G(u) &= 10\log 10(F(u)F^*(u)) \\ &= \frac{10}{\ln 10}\left\{\ln f^2(u)+\sum_{n=1}^{\bar{n}-1}\ln(u_n^4+\upsilon_n^4+u^4+2u_n^4\upsilon_n^2-2u^2u_n^2+2u^2\upsilon_n^2)-2\sum_{n=1}^{\bar{n}-1}\ln(u_n^2+\upsilon_n^2)\right\} \end{aligned} \tag{4.2.19}$$

We will denote the starting pattern by $G(u)$ and the desired pattern by $S(u)$. There are known starting values $u'_n + j\upsilon'_n$ for the inner roots, which are $u'_n = \gamma_{1n}$, $\upsilon'_n = 0$, $n = 1,2,\cdots,\bar{n}-1$. Quantity $S(u) - G(u)$ is the difference between what the power pattern one desires and what one has. Small changes, δu_n and $\delta\upsilon_n$ are sought to bring $G(u)$ closer to $S(u)$. The total differential gives

$$d(S-G)=\sum_{n=1}^{\bar{n}-1}\frac{\partial G}{\partial u_n}\delta u_n+\frac{\partial G}{\partial \upsilon_n}\delta \upsilon_n \tag{4.2.20}$$

where the partial derivatives on the right side of (4.2.17) are to be evaluated at the points

$$P_m = P(u'_1, \upsilon'_1, \cdots u'_{\bar{n}-1}, \upsilon'_{\bar{n}-1}, u = u_m)$$

Quantities u_m are the peak and null locations, $m = 1,2,\cdots 2(\bar{n}-1)$. The partial derivatives in (4.2.20) are given by

$$\frac{\partial G}{\partial u_n}=\frac{40}{\ln 10}\left\{\frac{u'_n(D_2-u_m^2)}{D_1}-\frac{u'_n}{D_2}\right\} \tag{4.2.21}$$

and

$$\frac{\partial G}{\partial \upsilon_n}=\frac{40}{\ln 10}\left\{\frac{\upsilon'_n(D_2+u_m^2)}{D_1}-\frac{\upsilon'_n}{D_2}\right\} \tag{4.2.22}$$

where

$$D_1 = u'^4_n+\upsilon'^4_n+u_m{}^4+2u'^4_n\upsilon'^2_n-2u_m{}^2u'^2_n+2u_m{}^2\upsilon'^2_n \tag{4.2.23}$$

and

$$D_2 = u'^2_n+\upsilon'^2_n \tag{4.2.24}$$

For computational convenience, we can rewrite (4.2.20) in a matrix form as

$$d(S-G) = A\cdot dG \tag{4.2.25}$$

with

$$dG = (\delta u_1, \delta u_2 \cdots \delta u_n, \delta \upsilon_1\ \delta \upsilon_2 \cdots \delta \upsilon_n)^T \tag{4.2.26}$$

$$S_m = S(u_m) \tag{4.2.27}$$

$$G_m = G(P_m) \tag{4.2.28}$$

$$A_{mn}=\frac{\partial G_m}{\partial u_n}=\frac{40}{\ln 10}\left\{\frac{u'_n(D_2-u_m^2)}{D_1}-\frac{u'_n}{D_2}\right\} \quad \text{for } n\le \bar{n}-1 \tag{4.2.29}$$

and

$$A_{mn} = \frac{\partial G_m}{\partial v_n} = \frac{40}{\ln 10}\left\{\frac{v'_n (D_2 + u_m^2)}{D_1} - \frac{v'_n}{D_2}\right\} \text{ for } \bar{n} - 1 < n \le 2(\bar{n} - 1) \qquad (4.2.30)$$

We need to select values for u_m that correspond to key directions in the pattern, usually the positions of side lobe peaks in the unshaped region and the positions of ripple maxima and minima in the shaped region.

4.2.4 Radius Limit of the RLSA Antenna

When using the approach mentioned in Section 4.2.2, we have to know how many peaks and nulls need to be perturbed. For the isoflux pattern being used to illustrate the hybrid synthesis method that has been developed, the EOC angle is $\theta_0 = 59.1^0$. So at least one peak is needed in the starting pattern in the angular range $59.1^0 < \theta < 90^0$ so that the pattern in that range can be controlled (the ideal isoflux pattern being zero there). The number of peaks changes with u defined in (4.2.8). If $\theta = \theta_0 = 59.1^0$, then

$$u = \frac{2a}{\lambda}\sin\theta_0 \qquad (4.2.31)$$

The operation frequency of our antenna is 19GHz, which gives $\lambda = 15.79mm$ in free space. The number of the peaks at the range $59.1^0 < \theta < 90^0$ only depends on aperture radius a. Fig.4.2-3 illustrates three patterns - starting patterns from (4.2.15) - for three different values of aperture radius a (namely $a = 5\lambda$, $a = 8\lambda$ and $a = 10\lambda$). From these patterns we can see that the aperture radius needs to be more than 8λ. If the radius is too large there are more peaks in the range $0^0 < \theta < 59.1^0$, which will cause physical difficulty in shaping the pattern. We prefer two peaks in the range $59.1^0 < \theta < 90^0$, and hence a good choice for the radius is $a = 10\lambda$. In this case, we

have 16 peaks in the range $0^0 < \theta < 59.1^0$ and 2 peaks in the range $59.1^0 < \theta < 90^0$, as shown in Fig.4.2-3 (c).

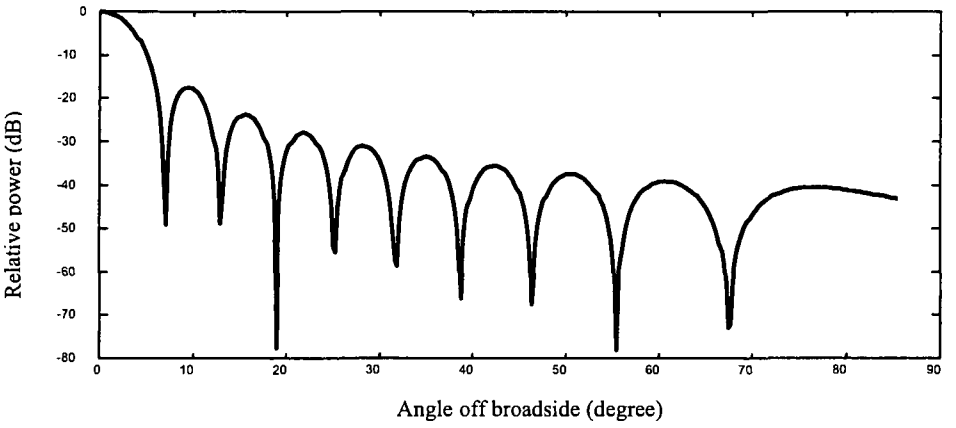

Fig.4.2-3 (a) Radiation Pattern for Uniformly Excited Circular Aperture with $a = 5\lambda$

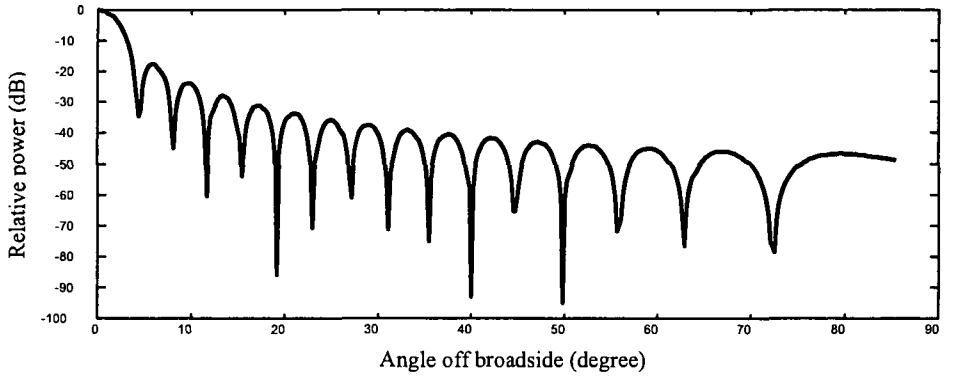

Fig.4.2-3 (b) Radiation Pattern for Uniformly Excited Circular Aperture with $a = 8\lambda$

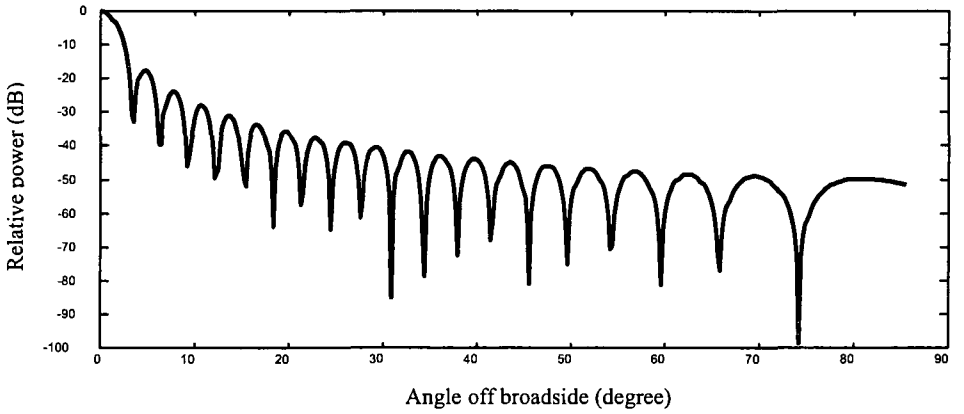

Fig.4.2-3 (c) Radiation Pattern for Uniformly Excited Circular Aperture with $a = 10\lambda$

4.2.4 Structured Perturbation of the Continuous Aperture Distribution to Obtain the Desired Pattern Shape

We here apply the method outlined in Section 4.2.3. First we shape all the peaks to the desired value at each peak location. We wrote a MATLAB program to reveal the 18 peak values $G(1)$, $G(2),\cdots G(18)$ and their locations $u_1^p, u_2^p, \cdots u_{18}^p$ which are listed in Table4.2.1. Fig.4.2-2 is used as the starting pattern which means $u_n = \gamma_{1n}$, for $n = 1,2,\cdots,\bar{n}-1$, $\bar{n} = 19$. At this step, no null filling is done, and so the imaginary parts $\upsilon_n \equiv 0$ and we do not seek values for $\delta\upsilon_n$. Matrix A can be calculated from (4.2.29). Perturbation δu_n is determined from (4.2.25) as

$$dG = A^{-1}(S - G) \tag{4.2.32}$$

New u'_n values arise from $u'_n = \gamma_{1n} + \delta u_n$, and a new $G(u)$ pattern can be computed from (4.2.19). It is found to be closer to what is desired than Fig.4.2-1 is, but is not yet adequate. It therefore becomes the new starting pattern for a second iteration. Repetition of this process 20 times finally leads to the pattern shown in Fig.4.2-4; all the peak values are exactly same as the desired pattern at the peak locations.

After each iteration the peak locations will shift. Some locations will shift a lot. So the directions used to sample the desired pattern S(u) have to be changed according to these new peak locations. We see in Fig.1.1-3 that at $\theta = 0^0$ we have $D = 2.34dB$. However, we cannot shape the peak at $\theta = 0^0$ using the method of Section 4.2.3. So we move the curve in Fig.1.1-3 down by 2.34dB and use this as our desired pattern. This won't cause any problems because shaped pattern mentioned [1] is relative power pattern, and at $\theta = 0^0$ we have $G(0) = 0$.

The desired values at each peak location, peak positions of starting pattern and the peak values of starting pattern are listed in Table 4.2-1. In Table4.2.2 are the real root values for the starting pattern and the shaped pattern with nulls.

Table 4.2.1: Desired Values, Starting Pattern Peak Values And Peak Locations

Number of Peak n	*Desired Peak Values S*	*Starting Peak Values G*	*Peak Locations Up*
1	0.0127	-17.57	1.0206
2	0.0510	-23.81	2.0385
3	0.1150	-27.9571	3.1287
4	0.2054	-31.0857	4.1326
5	0.3228	-33.5957	5.2017
6	0.4807	-35.7005	6.1803
7	0.6726	-37.5076	7.2162
8	0.9006	-39.0938	8.3018
9	1.1880	-40.5107	9.2891
10	1.5239	-41.7840	10.2484
11	1.9136	-42.9463	11.3712
12	2.4302	-44.0106	12.4435
13	3.0697	-44.9956	13.5182
14	3.9454	-45.9115	14.6330
15	15.8031	-46.7683	15.8031
16	7.8839	-47.5703	17.1344
17	-40	-48.3258	18.7089
18	-40	-49.0407	19.0691

Table 4.2.2: Root Values for Starting Pattern and Shaped Pattern After First Step

Root Number n	*Starting Pattern* γ_{1n}	*Shapted Pattern with Nulls* u_n
1	1.2197	0.5149
2	2.2331	1.544
3	3.2383	2.5755
4	4.2415	3.6085
5	5.2425	4.6415
6	6.2435	5.6753
7	7.2445	6.7085
8	8.2455	7.7426
9	9.2455	8.7846
10	10.2465	9.8400
11	11.2465	10.8648
12	12.2465	11.9277
13	13.2475	12.9958
14	14.2475	14.0775
15	15.2475	15.1881
16	16.2475	16.3753
17	17.2475	18.5749
18	18.2475	18.8750

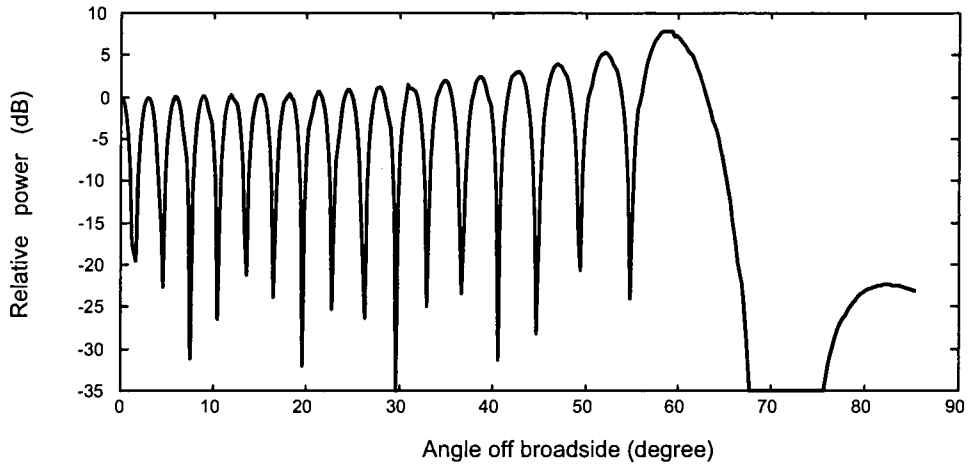

Fig.4.2-4 Shaped Pattern with Nulls after 20 Iterations

After we obtain the shaped pattern with nulls shown in Fig.4.2-4, we use complex roots to fill these nulls. We can set the starting values for the imaginary part of complex roots like

$$\upsilon_n = 0.1,\ n = 1,2,\cdots,16,\ \upsilon_{17} = 0,\ \upsilon_{18} = 0$$

We don't fill the two nulls in the range $59.1^0 < \theta < 90^0$, but just control the two peak values in this range with $S(17) = -40$, $S(18) = -40$. The u_n are obtained from Table 4.2-1. The starting pattern is now that shown in Fig.4.2-5.

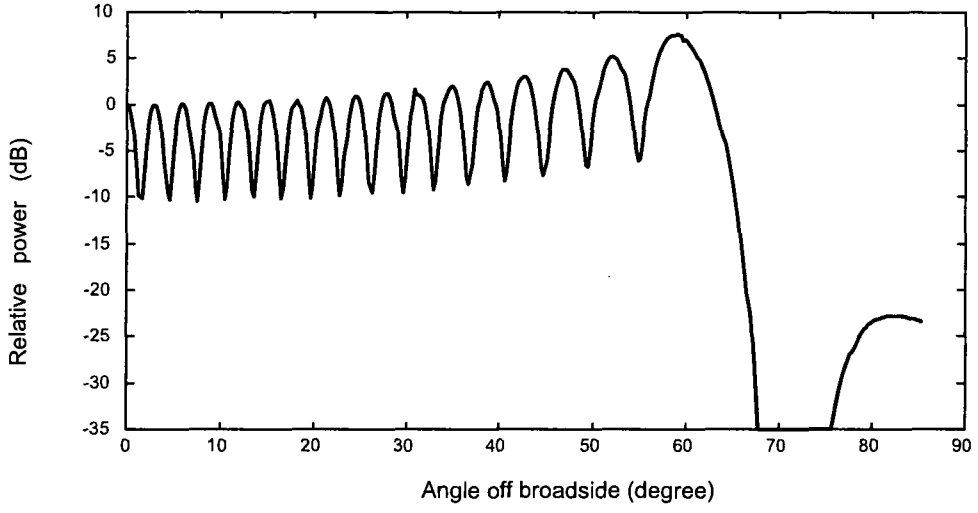

Fig.4.2-5 : Starting Pattern for Null Filling Obtained by Adding Imaginary Parts to Some of the Roots

After 3 iterations, we obtain a pattern with small ripples, as shown in Fig.4.2-6. It is closest to the desired one obtained thus far. The desired peak $S(17) = -40$ and $S(18) = -40$ has to be moved to $S(17) = -30$ and $S(18) = -31$ because of physical limitations. The final complex root values (at least for this Step#1 that is being described here in Section 4.2) are shown in Table 4.2.3.

Table 4.2.3: Complex Roots for Desired Pattern

Root Number n	u_n	υ_n
1	0.5134	0.5600
2	1.5428	0.5567
3	2.5775	0.5539
4	3.6189	0.5568
5	4.6703	0.5631
6	5.7458	0.6042
7	6.6582	0.8604
8	7.6056	0.5902
9	8.7153	0.5835
10	9.7922	0.6420
11	10.6856	0.6688
12	11.7304	0.5937
13	12.8049	0.5890
14	13.8663	0.5827
15	14.9399	0.5913
16	15.9972	0.6084
17	18.2122	0
18	18.6771	0

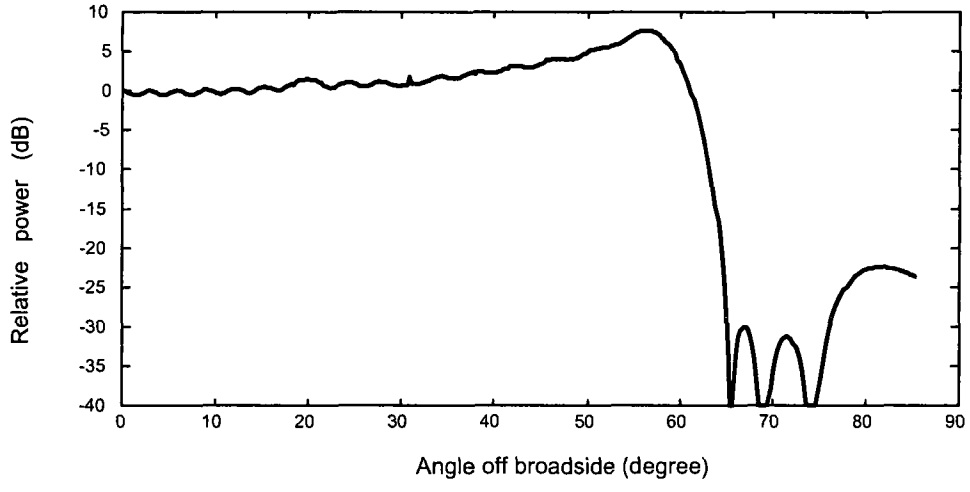

Fig.4.2-6 : φ - Symmetric Shaped Pattern

4.2.6 Continuous Aperture Distribution

Now that we have the complex roots of the desired pattern u_n and υ_n (n=1, 2 ,...18) from Table 4.2-4, we can use (4.2.14) to determine the continuous aperture distribution. When computing $F(\gamma_{1m})$ from (4.2.16), we have first to calculate $f(\gamma_{1m})$ from (4.2.17) as

$$f(\gamma_{1m}) = 2\frac{J_1(\pi\gamma_{1m})}{\pi\gamma_{1m}} \frac{1}{\prod_{n=1}^{\bar{n}-1} (1-\frac{\gamma_{1m}^2}{\gamma^2_{1n}})} \tag{4.2.33}$$

At $u = \gamma_{1m} = 0$,

$$f(0) = 1; \tag{4.2.34}$$

At $u = \gamma_{1m} \neq 0$, $J_1(\pi\gamma_{1m}) = 0$, and $\prod_{n=1}^{\bar{n}-1} (1-\frac{\gamma_{1m}^2}{\gamma^2_{1n}})$=0. Thus $f(\gamma_{1m})$ takes the "0/0" form, whose value needs to be determined using l'Hospital's rule. So we let

$$g_1(\pi u) = J_1(\pi u)$$

and

$$g_2(u) = \prod_{n=1}^{\bar{n}-1} (1-\frac{u^2}{\gamma^2_n})$$

The derivative of $J_1(u)$ can be expressed as

$$\frac{d(J_1(u))}{du} = \frac{uJ_0(u) - J_1(u)}{u} \tag{4.2.35}$$

Substituting $u = \gamma_{1m}$ and $J_1(\gamma_{1m}) = 0$ into (4.2.35) yields

$$\frac{d(J_1(u))}{du}\Big|_{u=\gamma_{1m}} = J_0(\gamma_{1m}) \tag{4.2.36}$$

The derivative of $g_1(\pi u)$ can be expressed as

$$\frac{dg_1}{du} = \frac{d(J_1(\pi u))}{d(\pi u)} \frac{d(\pi u)}{du} = \frac{d(J_1(\pi u))}{d(\pi u)} \pi \qquad (4.2.37)$$

At $u = \gamma_{1m}$,

$$\frac{dg_1}{du} = \pi J_0(\gamma_{1m}) \qquad (4.2.38)$$

The derivative of $g_2(u)$ is

$$\frac{d(g_2(u))}{du} = \sum_{m=1}^{\bar{n}-1} \left(\frac{-2u}{\gamma^2_{1n}}\right) \prod_{\substack{n=1 \\ n \neq m}}^{\bar{n}-1} \left(1 - \frac{u^2}{\gamma^2_{1n}}\right) \qquad (4.2.39)$$

At $u = \gamma_{1m}$

$$\frac{d(g_2(u))}{du}\Big|_{u=\gamma_{1m}} = \left(\frac{-2}{\gamma_{1m}}\right) \prod_{\substack{n=1 \\ n \neq m}}^{\bar{n}-1} \left(1 - \frac{\gamma_{1m}^2}{\gamma^2_n}\right) \qquad (4.2.40)$$

Hence (4.2.34) , (4.2.38) and (4.2.40) give the values for $f(\gamma_{1m})$ as

$$f(\gamma_m) = \begin{cases} f(u) = 1, & u = \gamma_{1m} = 0 \\ -\dfrac{J_0(\pi\gamma_{1m})}{\prod\limits_{\substack{n=1 \\ n \neq m}}^{\bar{n}-1} \left(1 - \dfrac{\gamma_{1m}^2}{\gamma^2_n}\right)}, & u = \gamma_{1m} \neq 0 \end{cases} \qquad (4.2.41)$$

$F(\gamma_{1m})$ in (4.2.14) can be obtained from

$$F(\gamma_{1m}) = f(\gamma_{1m}) \prod_{n=1}^{\bar{n}-1} \left[1 - \frac{\gamma_{1m}^2}{(u_n + j\upsilon_n)^2}\right] \qquad (4.2.42)$$

Fig.4.2-7 shows the aperture distribution (amplitude and phase). A study of (4.2.19) reveals that the power pattern is insensitive to the sign attached to υ_n. There are 2^{18} combinations of u and υ so there are 2^{18} different aperture distributions that will give the same patterns. We can choose some aperture distributions that are easy or possible to be excited in practice. In this thesis, the aperture distributions are calculated using positive υ_n.

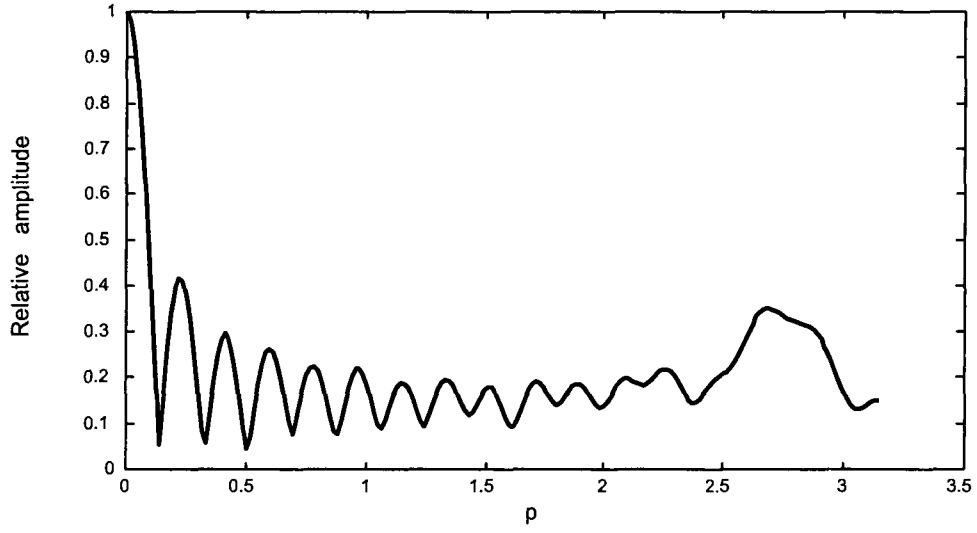

Fig.4.2-7 (a). Relative Amplitude of the Continuous Aperture Distribution for the Rotationally Symmetric Pattern Plotted Versus the Quantity $p = (\pi / a)\rho$.

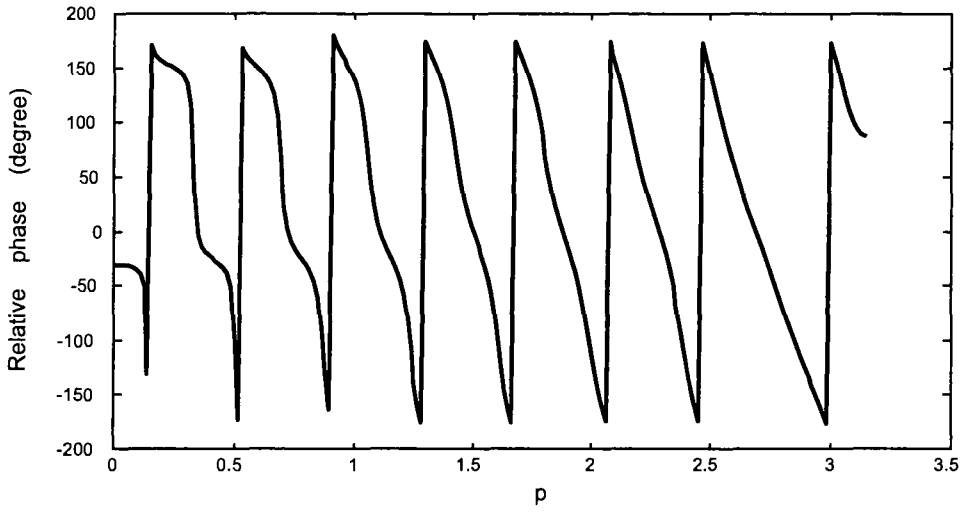

Fig.4.2-7 (b). Relative Phase of the Continuous Aperture Distribution for the Rotationally Symmetric Pattern Plotted Versus the Quantity $p = (\pi / a)\rho$.

4.3 STEP#2 – SAMPLING OF THE CONTINUOUS CIRCULAR APERTURE DISTRIBUTION TO OBTAIN A DISCRETE ARRAY

4.3.1 Circular Grid Array Sampling [1,2]

We have the aperture distribution for the continuous circular aperture in Fig.4.2-7. What we need for our RLSA antenna is a discrete aperture distribution (that is, a complex excitation for each slot pair). Some sort of sampling will have to be used to generate the discrete aperture distribution from the continuous one. The radius of the RLSA antenna was selected in Section 4.2.4 to be $a = 10\lambda$. It will be sampled on a family of concentric circles of radii ρ_m with $m = 1, 2, \cdots, M$, with integer M the total number of circles. Integer N_m is the total elements on the m th circle; it will be chosen to be divisible by four (namely $N_m = 4m$) so that there is quadrantal symmetry. All the elements are similarly oriented radiators of a common type, are

uniformly spaced along the m th circle, and are also equispaced along the ϕ direction. Fig.4.3-1 and Fig.4.3-2 show the described layout.

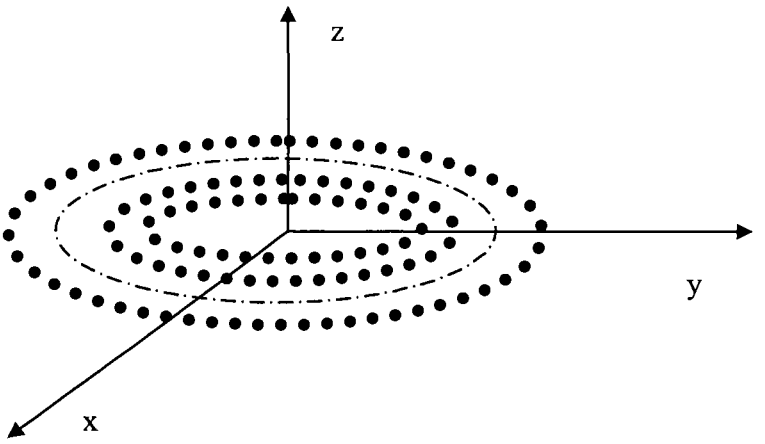

Fig.4.3-1 Discrete Radiating Elements in a Circular Grid Arrangement

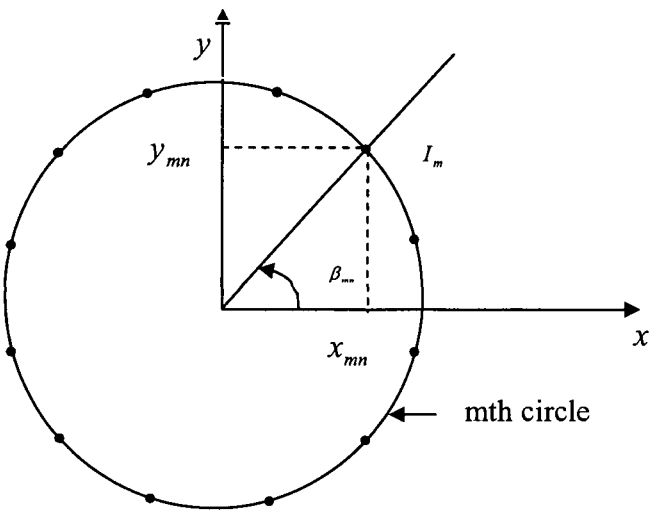

Fig.4.3-2 Discrete Radiating Elements in a Circular Grid Arrangement (Plane View)

The angular position of the n th radiator on the m th circle (written as mn th radiator) is

$$\beta_{nm} = (2n-1)\pi / N_m, \quad 1 \le n \le N_m \tag{4.3.1}$$

It therefore follows that in Cartesian co-ordinates the position of the mn th element is given by

$$x_{mn} = \rho_m \cos\frac{(2n-1)\pi}{N_m}, \quad y_{mn} = \rho_m \sin\frac{(2n-1)\pi}{N_m} \tag{4.3.2}$$

where the ρ_m of m th circle can be expressed as

$$\rho_m = \frac{2m-1}{2M}a \tag{4.3.3}$$

The radial distance between two adjacent rings is

$$\Delta\rho_m = \frac{a}{M} \tag{4.3.4}$$

All the elements on a common circular grid line are excited equally and in phase with an excitation I_m. We use the conventional sampling method to obtain

$$I_m = g_0(\rho_m) \tag{4.3.5}$$

The pattern[10] is given by

$$\begin{aligned} F(\theta,\phi) &= 4\sum_{m=1}^{M}\sum_{n=1}^{m} I_m \cos(kx_{mn}\sin\theta\cos\phi)\cos(ky_{mn}\sin\theta\sin\phi) \\ &= 4\sum_{m=1}^{M}\sum_{n=1}^{m} I_m \cos(k\rho_m \cos\frac{(2n-1)\pi}{N_m}\sin\theta\cos\phi) \\ &\quad \times\cos(k\rho_m \cos\frac{(2n-1)\pi}{N_m}\sin\theta\sin\phi) \end{aligned} \tag{4.3.6}$$

The directivity for an array with array factor $F(\theta,\phi)$ can be written as

$$D(\theta,\phi) = \frac{4\pi[F(\theta,\phi)\cdot F^*(\theta,\phi)]}{\int_0^{2\pi}\int_0^{\pi}[F(\theta,\phi)\cdot F^*(\theta,\phi)]\sin\theta\, d\theta\, d\phi} \tag{4.3.7}$$

[10] Recall in this present step (Step#2) we are still working with isotropic radiating elements (at whose positions we will eventually place slot-pairs). The full vector patterns of the RLSA antenna are dealt with in synthesis Step#4 in Section 4.5.

Expression (4.3.10) is evaluated by approximating the integral in the denominator by

$$\int_0^{2\pi}\int_0^{\theta_1} [F(\theta,\phi)\cdot F^*(\theta,\phi)]\sin\theta\, d\theta\, d\phi \approx \sum_0^{2\pi}\sum_0^{\theta_1} [F(\theta,\phi)\cdot F^*(\theta,\phi)]\sin\theta\,\Delta\theta\,\Delta\phi$$

with $\Delta\theta = \frac{\pi}{2}/100$, $\Delta\phi = 2\pi/100$. It is easy to check the accuracy of the expression by simply recomputing it using smaller values of $\Delta\theta$ *and* $\Delta\phi$ until convergence is achieved.

4.3.2 Determination of the Number of Rings (M) of the RLSA Antenna

How many rings in our RLSA design has to be determined first. Then we can use (4.3.6) and (4.3.7) to calculate the pattern. The distance between two adjacent rings cannot be too small because intended radiators are slot-pairs; the distance between the members of a slot-pair is a quarter wavelength, and each slot itself has a certain finite length. There must be sufficient space between the rings to accommodate these radiating elements. But if the distance is too great, the pattern obtained from the sampled distribution will be so different from that obtained from the continuous distribution that we will not be able to adjust (optimize) the discrete excitations to achieve the desired pattern. Fig.4.3-3 gives the patterns obtained from the sampled aperture distributions for different ring spacings.

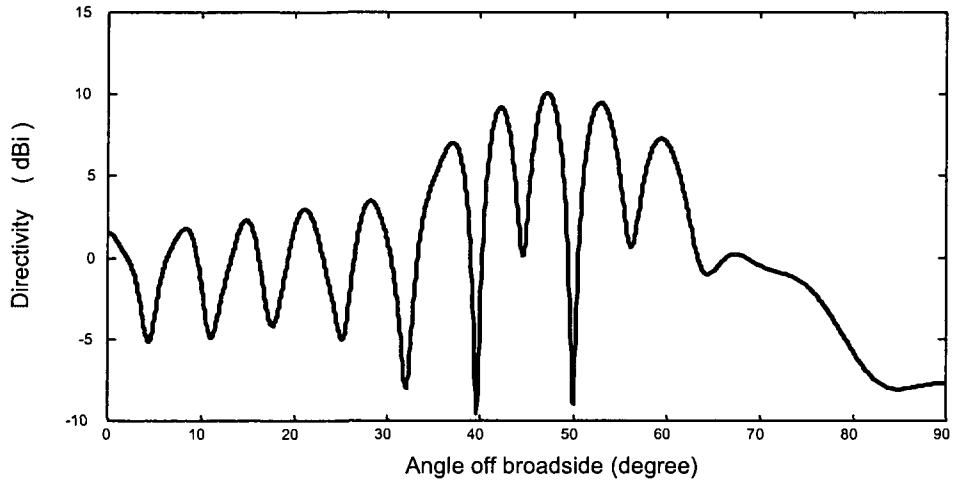

Fig.4.3-3 (a) Circular Grid Array Pattern With M=15

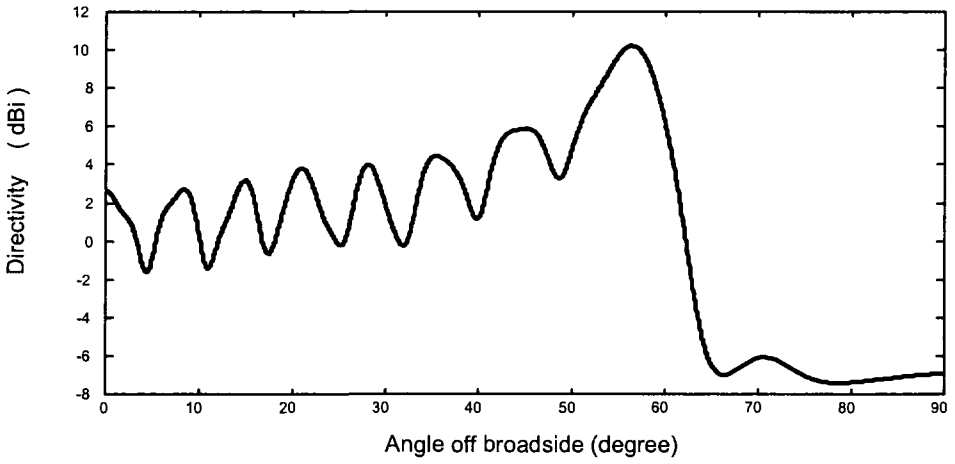

Fig.4.3-3 (b) Circular Grid Array Pattern With M=20

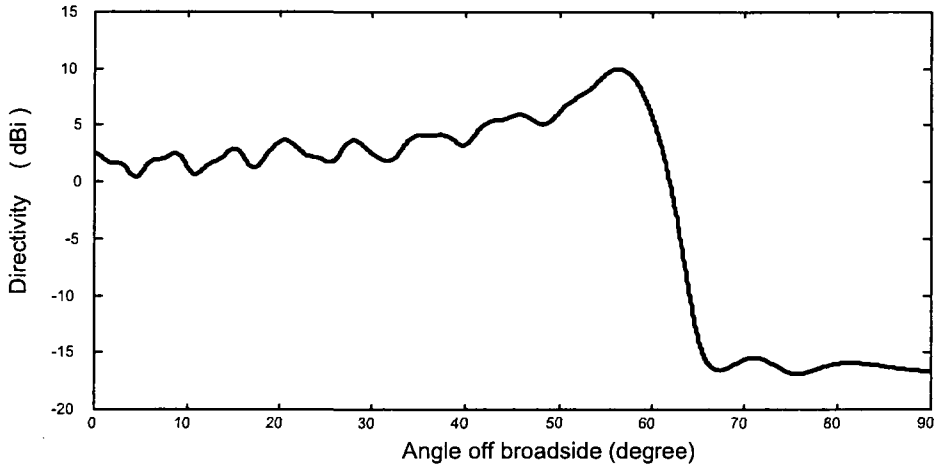

Fig.4.3-3 (c) Circular Grid Array Pattern With M=40

As expected the pattern in Fig.4.3-3(c) most closely approximates the desired pattern, but $\Delta\rho_m = 0.25\lambda$ is (layout-wise) impossible to implement using slot-pairs. The pattern in Fig.4.3-3(a) is not at all similar to the desired pattern and so is unacceptable. So we chose $M = 20$ and $\Delta\rho_m = 0.5\lambda$, for which case the pattern is that Fig.4.3-3 (b). The ripples in Fig.4.3-3 (b) are still relatively large and so the excitations are perturbed using an optimisation scheme in Step#3 that is discussed in Section 4.4.

For the RLSA antenna the aperture distribution will be implemented by slot-pairs in the top plate of a radial waveguide. The field in the radial waveguide is excited using mechanisms located at the centre of the radial waveguide (as described in Chapter 2), and so the field at the centre is large. If radiating slot-pairs are located around the centre of the radial waveguide, coupling to these slots will disturb the inner field significantly [4]. So slot-pairs are excluded from the central portion of the aperture. This constitutes blockage of the central portion of the

RLSA antenna aperture. Thus only 19 rings will be used, resulting in a central blocking radius of $r_c = 0.25\lambda$. The resulting pattern with this central blockage is shown in Fig.4.3-4

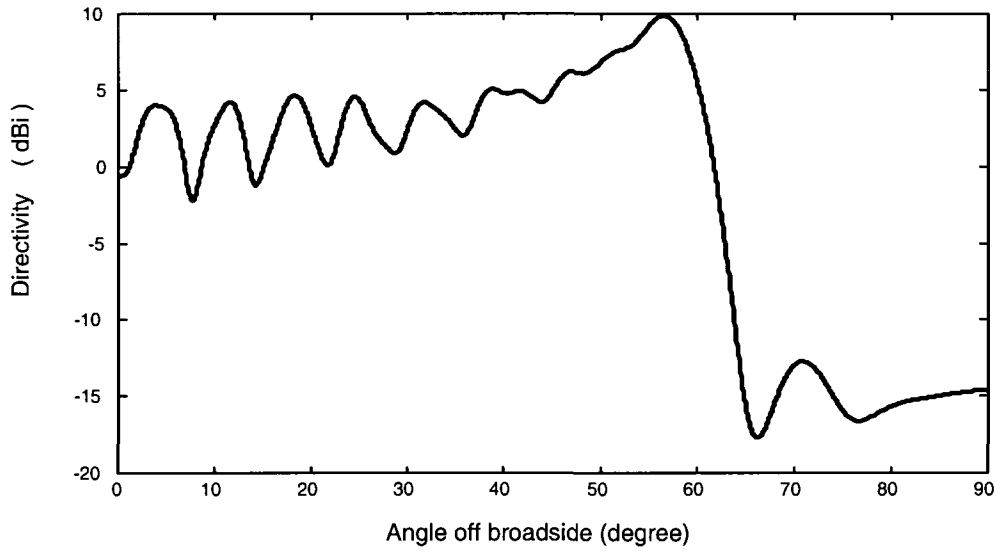

Fig.4.3-4 : Pattern of Circular Grid Array Antenna Taking into the Central Blockage

4.4 STEP#3 – OPTIMIZATION OF THE EXCITATIONS OBTAINED BY SAMPLING THE CONTINUOUS APERTURE

The pattern in Fig.4.3-4 is not as good as we would like, since the ripples are about 6dB peak-to-peak. In order to improve it we will first adjust the location of each ring using a least-squares optimisation method, and then adjust the excitation on each ring using the same method. Details of the least-squares approach are provided in Section 4.4.1.

4.4.1 Location Optimization

The starting pattern is shown in Fig.4.3.4, the m th ring location or the radial location of the mn th element is given by (4.3.3) as $\rho_m = \frac{2(m+1)-1}{40}a$, with $m = 1, 2, \cdots 19$ and $a = 10\lambda$ in the present illustrative being considered. We will call ρ_m the "nominal radius" of the m th ring. We can move the rings radially around their nominal radius to find the optimized locations; the elements on a given ring will move with the ring and the angular location β_{nm} of each element in (4.3.1) won't be changed .This moving won't destroy the φ-symmetry of the pattern. Fig.4.4.1 shows the nominal radius of m th ring and its possible optimized location.

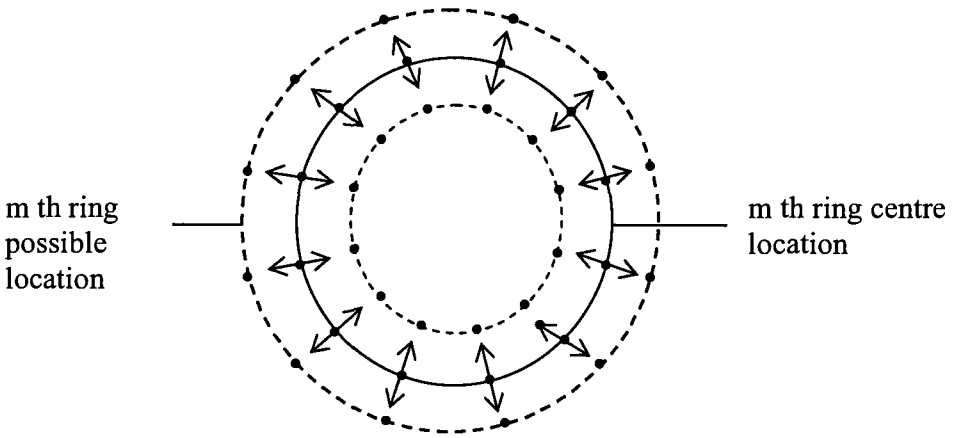

Fig.4.4-1 : Determining the Best Location of the *m* th Ring

We chose $M_s = 1280$ sample rings along the radius of the circular aperture with equal spacing. Each sample ring is a possible optimized location for our rings. The distance between two adjacent sample rings is

$$d_s = \frac{a}{1280} = 7.8125 \times 10^{-3} \lambda = 7.9mm$$

The complex excitation of each sample ring can be found using conventional sampling as in (4.3.5). In the case of the m_s th sample ring the excitation is

$$I_{ms} = g_0(\rho_{m_s}) \tag{4.4.1}$$

$$\rho_{m_s} = \frac{a}{1280} m_s, \quad m_s = 1, 2, \cdots, 1280$$

The relation between the sample ring number m_s and the ring number m where our radiation elements are located can be expressed as

$$m_s = 32 + 64m$$

There are 63 possible sample rings between two adjacent rings at their nominal radii. For the m th ring the possible sample rings can move from the ring $m_s - 32$ to $m_s + 32$, whereas for the for the first ring ($m = 1$) the possible sample rings are from $m_s = 64$ to $m_s = 128$.

In the ring location adjustment (optimization) procedure we first execute a loop (that is, let the ring move from the sample ring 64 to 128) for the first ring with the other 18 rings kept fixed at their nominal radii. Each time we move the ring from one sample ring to another sample ring a new pattern is calculated, and the value of the least square error function related to this new pattern is also calculated by (4.4.2)

$$f = \int_0^{\theta_1} [D_{des}(\theta) - D(\theta]^2 d\theta \tag{4.4.2}$$

where $D_{des}(\theta)$ is the desired directivity pattern and $D(\theta)$ is the pattern we are optimizing. Expression (4.4.2) is evaluated by approximating the integral in the denominator by $\int_0^{\theta_1} [D_{des}(\theta) - D(\theta]^2 d\theta \approx \sum_0^{\theta} \left(D_{des}(\theta) - D(\theta)\right)^2 \Delta\theta$, and $\Delta\theta = \frac{\pi}{2}/100$. After the loop is executed, the minimum value of f is found. The pattern corresponding to the minimum f is the closest

one to $D_{des}(\theta)$ in this loop, and the ring location corresponding to the minimum f is the best one for the first ring.

Then we repeat the procedure for each ring in turn, each time keeping the other rings fixed. Sometimes a particular ring radius adjusts very little or not at all. We then repeat the complete procedure (starting at the first ring again) since we adjusted things one ring at a time.

The optimized radii for the first four rings are

$$\rho_1 = 15.4mm$$

$$\rho_2 = 22.0mm$$

$$\rho_3 = 27.9mm$$

$$\rho_4 = 35.5mm$$

We performed the optimization to the 5th ring to 19th ring and found the radii of the 5th through 19th rings didn't change, they are still at their centre locations shown in Table 4.4.1. We can see from the Table 4.4.1 that the first ring moved from its nominal radius. The space between the first ring and the second ring is $d1 = 6.6mm$, the space between the second and third ring is $d2 = 5.9mm$ and the space between the third ring and fourth ring is $d3 = 7.6mm$. The excitations for the elements on these four rings are

$$I_1 = g_0(\rho_1) = -2.8805 + 3.5817i$$

$$I_2 = g_0(\rho_2) = 9.0506 - 5.0838i$$

$$I_3 = g_0(\rho_3) = -7.2422 + 2.7062i$$

and

$$I_4 = g_0(\rho_4) = 3.2932 + 1.4978i$$

4.4.2 Aperture Distribution Optimization

We next fix the ring radii at the adjusted values determined above. The excitation on each ring is determined from the conventional sampling of the continuous aperture distribution as in expression (4.3.7). Next we alter the locations of each element excitation (keeping the ring radii fixed) to minimize the error function in (4.4.2). In the present example being used to illustrate use of the synthesis method we found that only the excitations on the first and second rings changed noticeably, and are now

$$I_1 = -5.4106 + 4.7105i$$

$$I_2 = 8.8318 - 5.0519i$$

The excitations on each ring are at this stage shown in Table 4.4.1

Table 4.4-1: Excitations at the End of Step#4

Ring Number	*Radius of Ring (m)*	*Excitation of Ring*	
		Phase	*Amplitude*
1	0.0154	138.9567	0.5541
2	0.0220	-29.7700	0.7859
3	0.0279	159.5110	0.5971
4	0.0355	24.4564	0.2794
5	0.0434	-88.5799	0.2444
6	0.0513	128.8932	0.4646
7	0.0592	-35.6591	0.5189
8	0.0671	157.6910	0.5841
9	0.0750	5.3848	0.5122
10	0.0829	-161.8282	0.3916
11	0.0908	68.9771	0.4171
12	0.0987	-70.5713	0.4195
13	0.1066	137.7082	0.5747
14	0.1145	2.5892	0.6387
15	0.1224	-159.6444	0.5257
16	0.1303	62.1832	0.8417
17	0.1382	-37.5856	0.9999
18	0.1461	-133.9189	0.8433
19	0.1539	118.4785	0.3884

The directivity pattern is now that shown in Fig.4.4-2(a), which shows a ripple of 1.5dB. The curve compared with the desired pattern was plotted in Fig 4.4.2b, we can find that our optimized the pattern is 3.5dB under the desired one, this can be solved by mounting the array antenna on an infinity ground plane which will be discussed in the next chapter. Fig.4.4.2c shows the comparison of the two curves if the desired curve is moved down 3.5dB, Fig.4.4.2d shows the curves in Fig.4.4.2c at our interested range $0^0 < \theta < 59.1^0$.

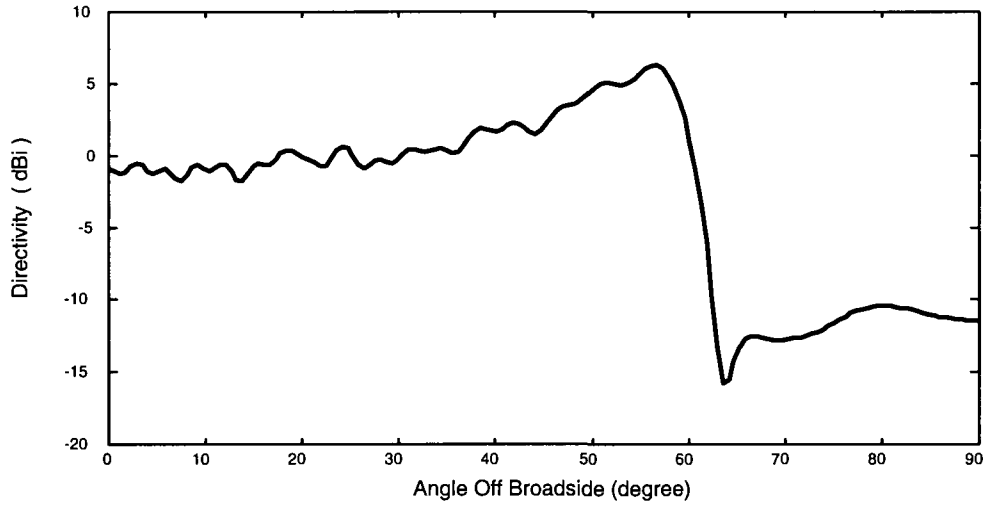

Fig.4.4-2(a) : Directivity pattern at the end of Step#3

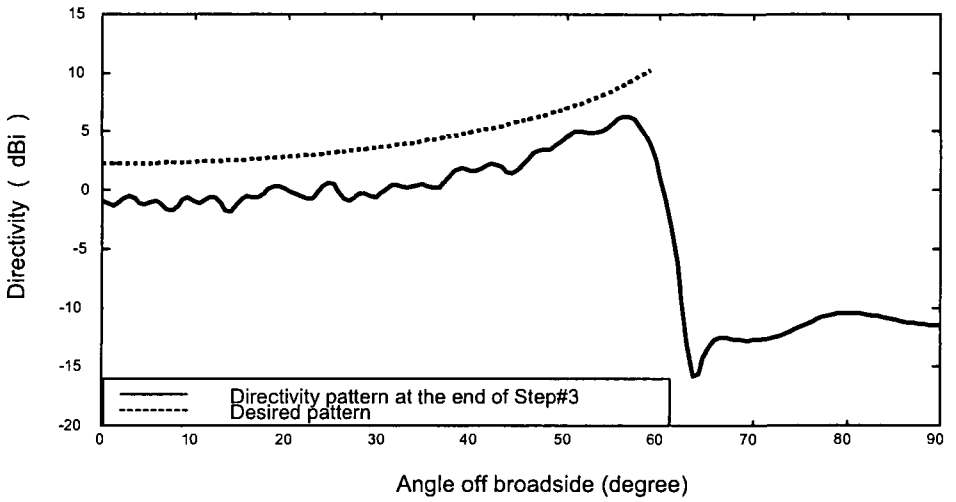

Fig.4.4-2 (b) : Directivity pattern at the end of Step#3 compared with desired pattern.

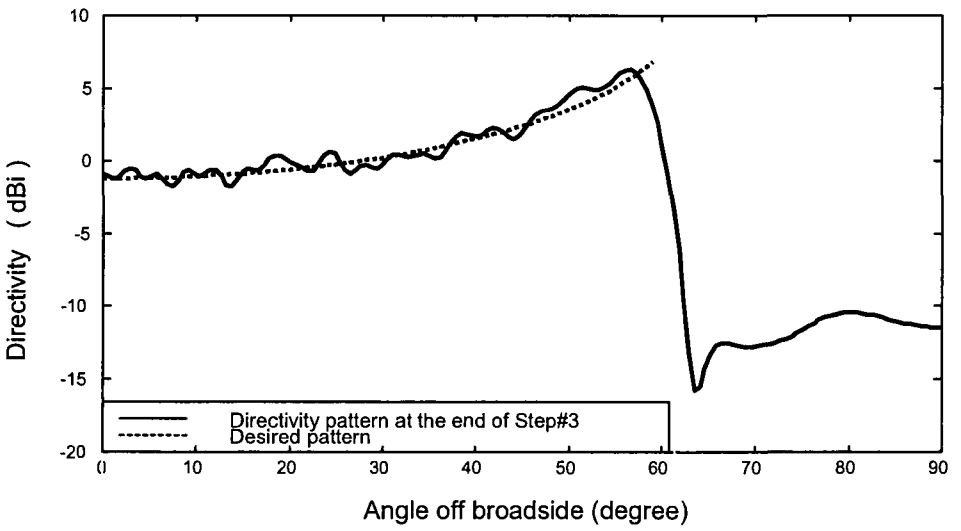

Fig.4.4.2 (c) : Directivity pattern at the end of Step#3 compared to the desired pattern shifted down by 3.5dB

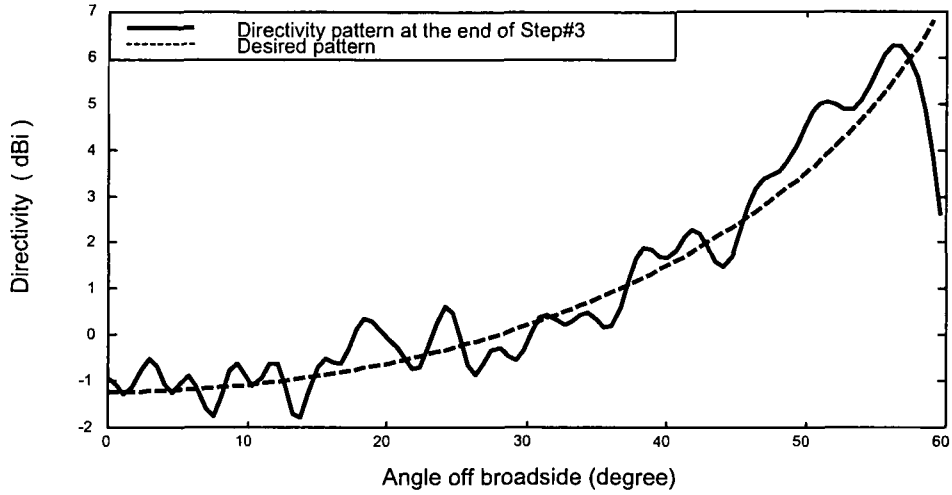

Fig.4.4-2 (d) : Directivity Pattern at the End of Step#3 Compared to the Desired Pattern (Shifted Down by 3.5dB) Over the Angular Range $0^0 < \theta < 59.1^0$

4.5 STEP#4 – FINAL OPTIMIZATION OF THE VECTOR RADIATION PATTERN OF THE RLSA ANTENNA

4.5.1. Vector Radiation Pattern of the RLSA Antenna

In the synthesis procedure steps used thus far we have assumed isotropic radiation elements. We now take into account the fact that the radiating elements are slot pairs, so that the vector patterns can be determined. We use the analysis described in Section 3.6. In the realisation of an RLSA antenna the slot lengths would be different for each slot-pair so as to alter the coupling to the radial waveguide fields to achieve the excitations we are synthesising here. However, whereas the coupling to a slot is sensitive to small changes in its length, the radiation patterns of a slot-pair is not. Thus during the present synthesis stage, when we are still in the process of determining what the excitations need to be, we can assume all slots to be of the same length when computing the vector radiation patterns of the RLSA antenna. The co-polarised radiation

pattern of the RLSA antenna whose element locations and excitation are those in Table 4.4.1 (obtained in Step#3) is then that shown in Fig.4.5-1. The directivity is determined in the manner outlined at the end of Section 4.3.1, using the appropriate vector pattern results of course.

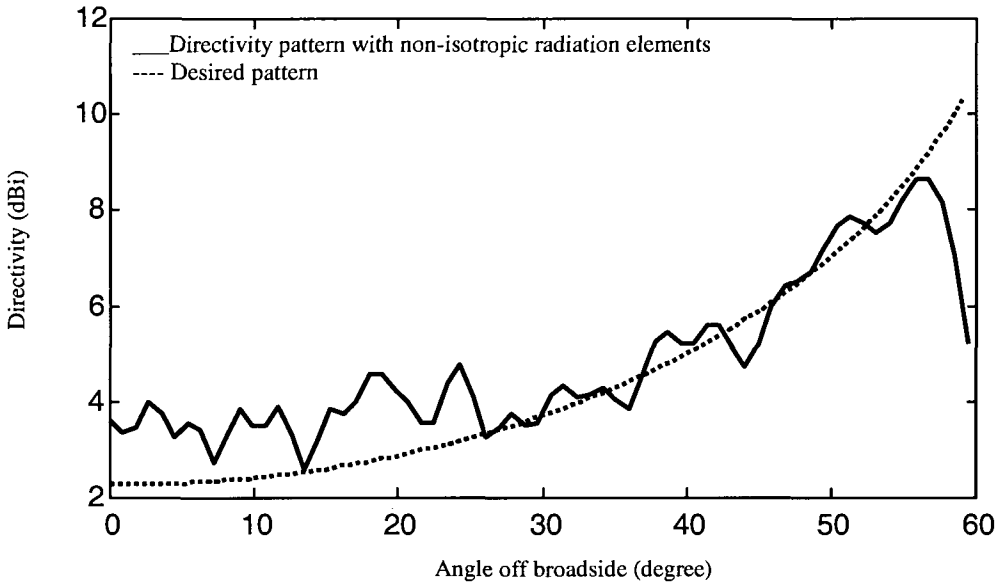

Fig.4.5-1 : Pattern from Step#3 with Non-Isotropic Radiating Elements

4.5.2 Final RLSA Antenna Vector Pattern Optimization

We can see from Fig.4.5-1 that, with the actual radiating elements (slot-pairs) taken into account when computing the radiation pattern, the pattern is not as good as that obtained using isotropic elements. The actual pattern is higher than the desired one around boresight, and lower than it in the vicinity of the EOC. The reason is of course that all previous optimisation stages were performed assuming isotropic elements. In order to have the RLSA antenna have a pattern that is closer to the desired pattern in practice, we adjust the excitations one final time (this time including the effects of the slot-pair element pattern shown in Fig.4.5-2.

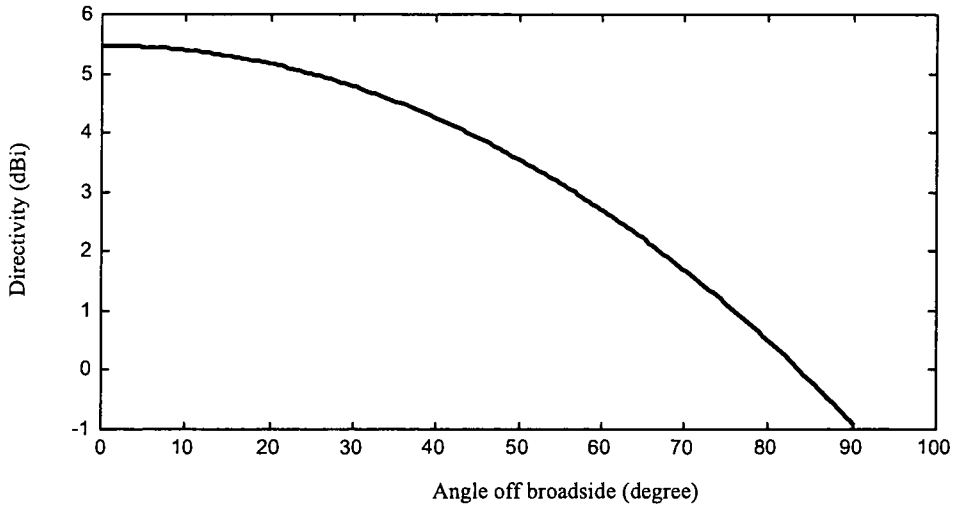

Fig.4.5-2 : Directive Pattern for a Radiating Slot-Pair Element

We retain the values of S_m from Step#3 at those locations where θ is small, but increase the values of S_m at the locations where θ is large. We also retain the values of S_m at those sample points beyond the shaped region (in this particular example the points S_{17} and S_{18}) because they won't significantly contribute to changes in the shaped region. With this new set of S_m values we repeat all the sub-steps from Section 4.2.4 through Section 4.5.1 - finding the continuous aperture distribution, performing the sampling, computing the pattern assuming isotropic elements. Thereafter we determine the vector radiation pattern of the RLSA antenna again, examine how we have done, and then repeat things once more if necessary. During each of the above-mentioned repeats of the sub-steps we keep the locations of all slots fixed[11]. Fig.4.5-3 shows a plot of the adjusted S_m and the desired S_m . Table 4.5.1 gives the final aperture excitations obtained from the adjusted S_m. Fig.4.5-4 (a) shows the RLSA antenna pattern

[11] At the locations found during the first application of the sub-step in Section 4.4.1.

assuming isotropic elements (it is merely the array factor) using the final aperture distribution. Fig.4.5-4(b) and Fig.4.5-4 (c) give the co-polarised RLSA antenna directivity pattern using the same final aperture distribution, but using the vector pattern expressions for the RLSA antenna.

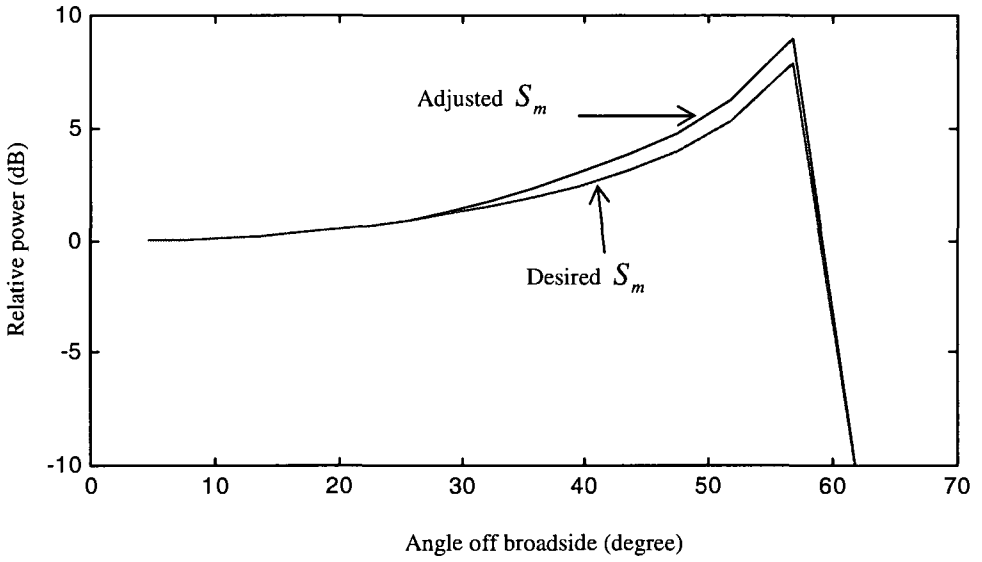

Fig.4.5-3 Adjusted S_m and Desired S_m

Table 4.5.1 Optimized Aperture Excitation

Ring Number	*Radius of Ring (m)*	*Excitation of Ring*		*Optimized Excitation*	
		Phase	*Amplitude*	*Phase*	*Amplitude*
1	0.0154	138.9567	0.5541	-48.0304	0.5904
2	0.0220	-29.7700	0.7859	120.5843	0.8763
3	0.0279	159.5110	0.5971	-69.6712	0.7185
4	0.0355	24.4564	0.2794	72.9075	0.3684
5	0.0434	-88.5799	0.2444	-167.5939	0.2766
6	0.0513	128.8932	0.4646	-33.6171	0.4911
7	0.0592	-35.6591	0.5189	128.8314	0.5821
8	0.0671	157.6910	0.5841	-65.0702	0.6758
9	0.0750	5.3848	0.5122	89.6808	0.6103
10	0.0829	-161.8282	0.3916	-103.9336	0.4940
11	0.0908	68.9771	0.4171	29.8528	0.4820
12	0.0987	-70.5713	0.4195	169.2622	0.4669
13	0.1066	137.7082	0.5747	-42.3936	0.6347
14	0.1145	2.5892	0.6387	93.0860	0.7039
15	0.1224	-159.6444	0.5257	-107.3187	0.6135
16	0.1303	62.1832	0.8417	30.2565	0.9022
17	0.1382	-37.5856	0.9999	131.4764	1.0000
18	0.1461	-133.9189	0.8433	-132.8332	0.8060
19	0.1539	118.4785	0.3884	-26.4631	0.3644

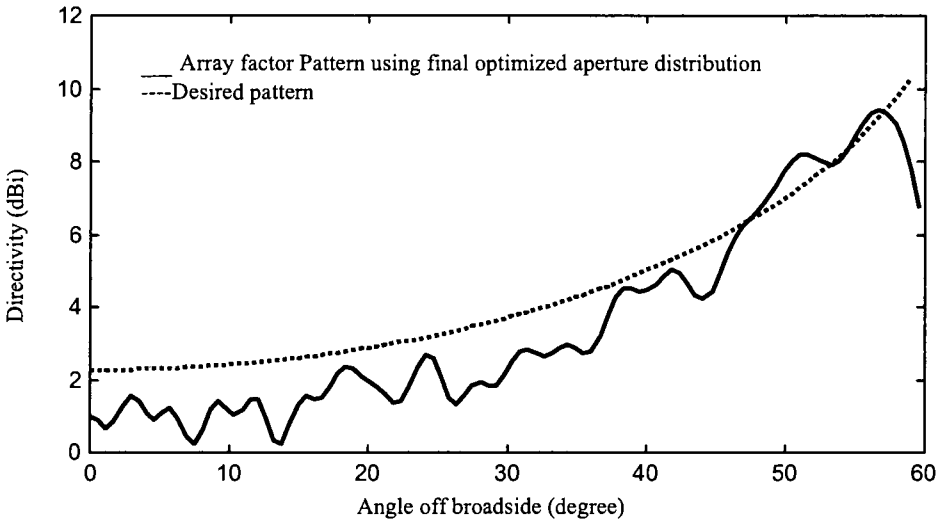

Fig.4.5-4 (a) : Array Factor Directivity Pattern Using Final Optimized Aperture Distribution

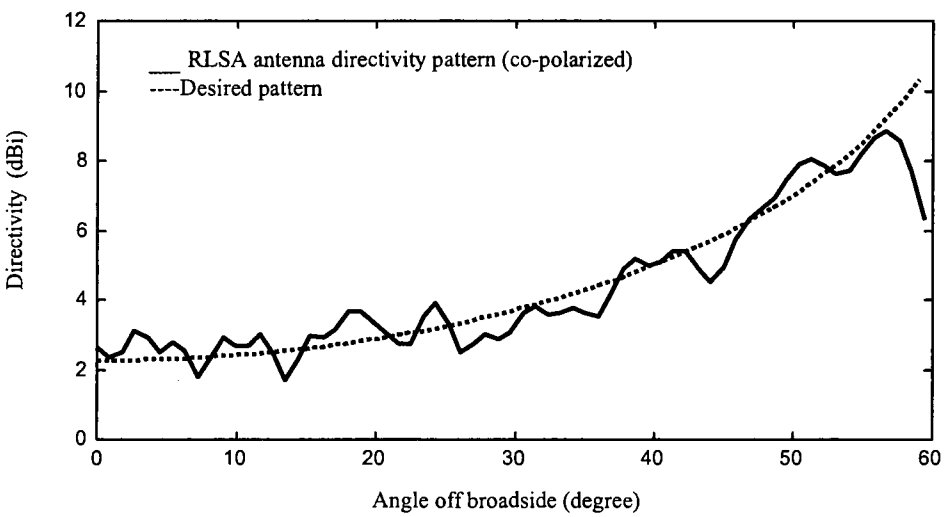

Fig.4.5-4 (b) : RLSA Antenna Directivity Pattern Using Final Optimized Aperture Distribution

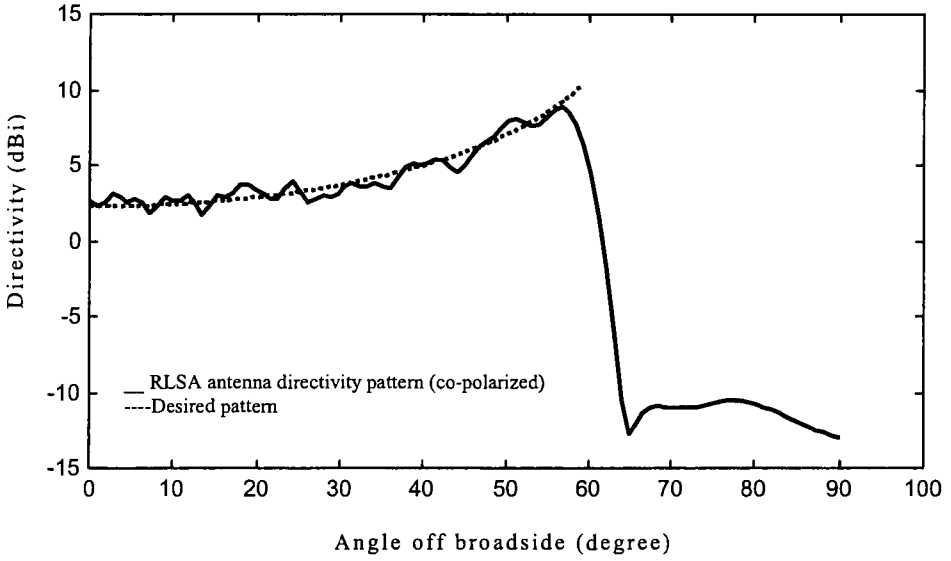

Fig.4.5-4 (c) : RLSA Antenna Directivity Pattern Using Final Optimized Aperture Distribution

4.6 FURTHER EXAMPLES

4.6.1 High Directivity Radiation Pattern with Sidelobe Control Example

In this example we are considering the case of a high directivity radiation pattern with sidelobe control. The requirement for the directivity is about 30 dBi, with sidelobes -25 dB below the main lobe, for a centre frequency of 5 GHz. An aperture radius of 5 wavelength is chosen.

For sidelobe control, in the first step the sidelobe values should be set a little lower than the specification since after sampling if the number of the circle M is not big enough the sidelobes of the radiation pattern will be higher than those of the continuous aperture distribution. We found the innermost three values of sidelobes in the starting pattern are higher then -30 dB, the peak values are all less than -30 dB after the third sidelobes. So for the desired sidelobe -25 dB, just

the first three peaks need to be shaped. We can set $S_m = -30dB$ for m=1,2,3. Table 4.6.1 shows the root positions and peak (sidelobe) positions of the starting pattern and desired peak values. To control the sidelobes $\bar{n} - 1 = 3$ is chosen. The root values for the desired pattern are also shown in Table 4.6.1 as they are after Step#1. Fig.4.6-1 gives the continuous aperture distribution. The pattern from this continuous aperture distribution is shown in Fig.4.6-2. In Step#2 we select a sampling $M = 10$ and 9 rings. After applying the sampling process as per Step#2, and performing the optimizations as per Step#3 and Step#4, we obtain the slot-pair excitations and radial positions as shown in Fig. 4.6-3. The associated radiation pattern of the synthesized RLSA antenna is shown in Fig.4.6-4

Table 4.6-1: Desired Values, Starting Pattern Peak Values And Peak Locations

Number of peak n	Starting pattern γ_{1n}	Peak locations Up	Starting peak values G	Desired peak values S	Roots for desired pattern
1	1.2197	1.635	-17.57	-30	1.5494
2	2.2331	2.679	-23.81	-30	2.1983
3	3.2383	3.699	-27.9571	-30	3.1300

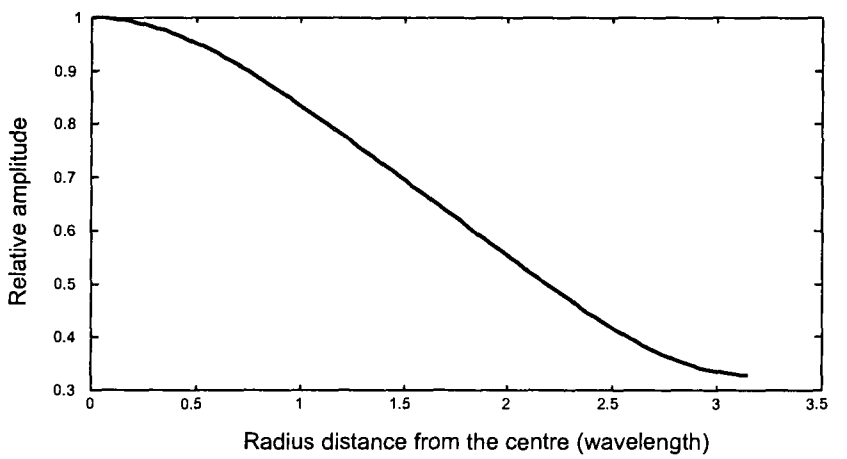

Fig. 4.6-1 Continuous Aperture Distribution for HD Pattern with Sidelobe Control

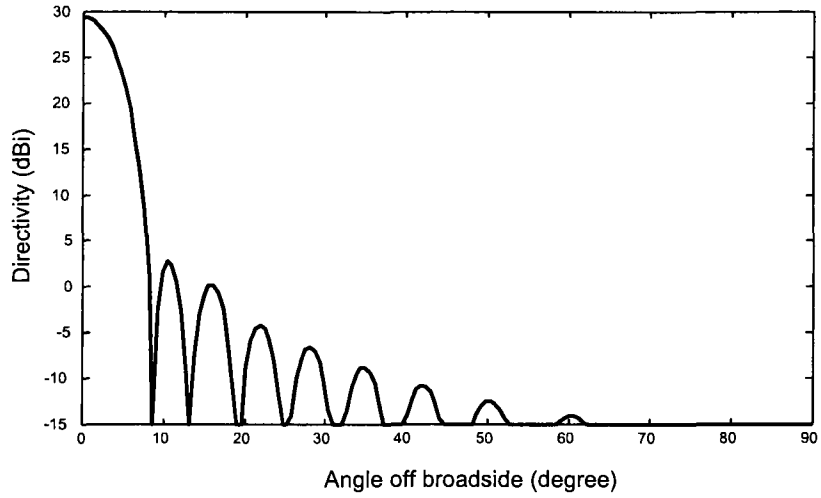

Fig. 4.6-2 Array Factor Pattern with Continuous Aperture Dstribution for High-Directivity Pattern

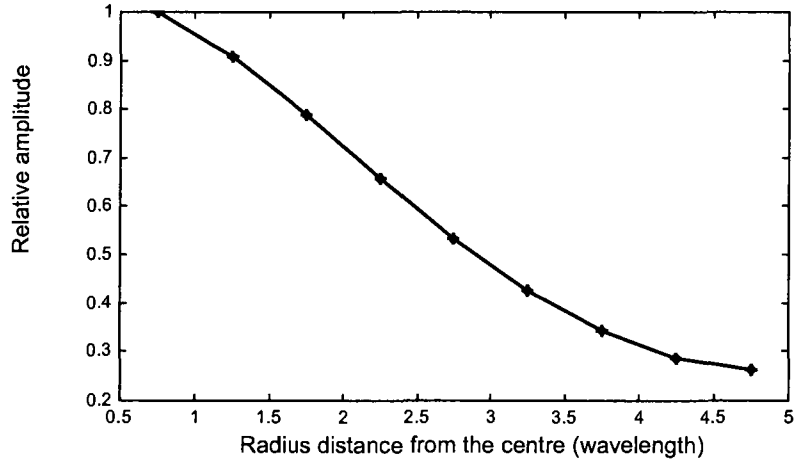

Fig. 4.6-3 Aperture Distribution for HD Pattern with Sidelobe Control

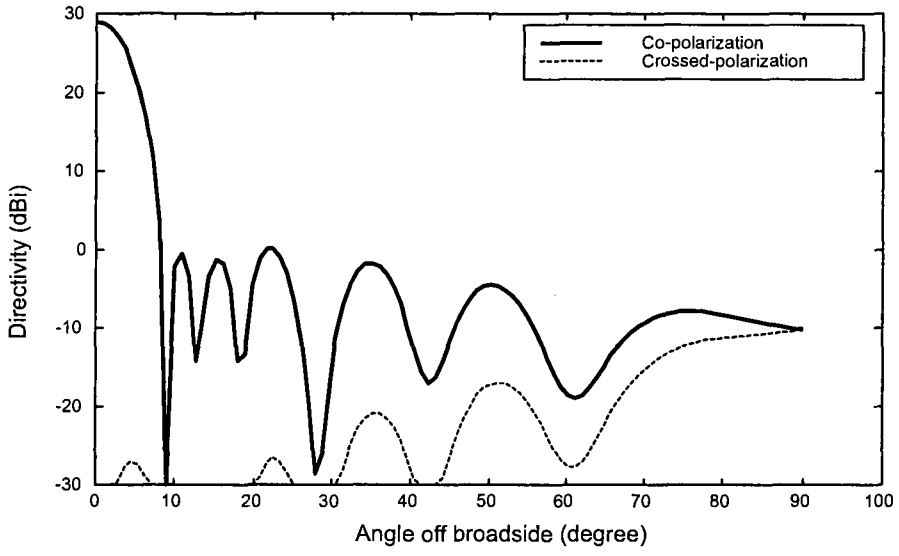

Fig.4.6-4 High Directivity Radiation Pattern with Sidelobe Control

4.6.2 Flat-Topped Radiation Pattern Example

As another example, we synthesized a flat-topped radiation pattern at centre frequency of 5GHz, and radius of 5 wavelength. In Step#1 we used $\bar{n}-1=5$ for which the two innermost sidelobes are at 0 dB and the next three at the -25 dB level. After 20 iterations we obtained the pattern of Fig.4.6-5 with real root values, and then we used complex root values to fill the first two nulls. The small initial values for these imaginary components of the two innermost pairs of roots were $\upsilon_1 = 0.01$ and $\upsilon_2 = 0.01$. After 5 iterations the complex root values are obtained for the pattern with smallest ripples; these are listed in the column #8 of Table 4.6-2. With these root values a continuous aperture distribution can be calculated which is shown in Fig.4.6-6, which gives the shaped pattern shown in Fig.4.6-7. We selected a sampling with $M=10$ and 9 rings. After adjusting the locations and the element excitations via the procedures in Step#3 and Step#4 we obtained a pattern shown in Fig.4.6-8. It clearly is not quite flat-topped. Adjusted values

S_m were therefore used as shown in column#6 of Table 4.6-2. The pattern with adjusted values S_m and continuous aperture distribution is now that shown in Fig.4.6-9. Following the re-application of Step#2 through Step#4, we obtain the flat-topped pattern shown in Fig.4.6-10 whose aperture distribution and element radius locations are given in Fig.4.6-11 and Fig.4.6-12.

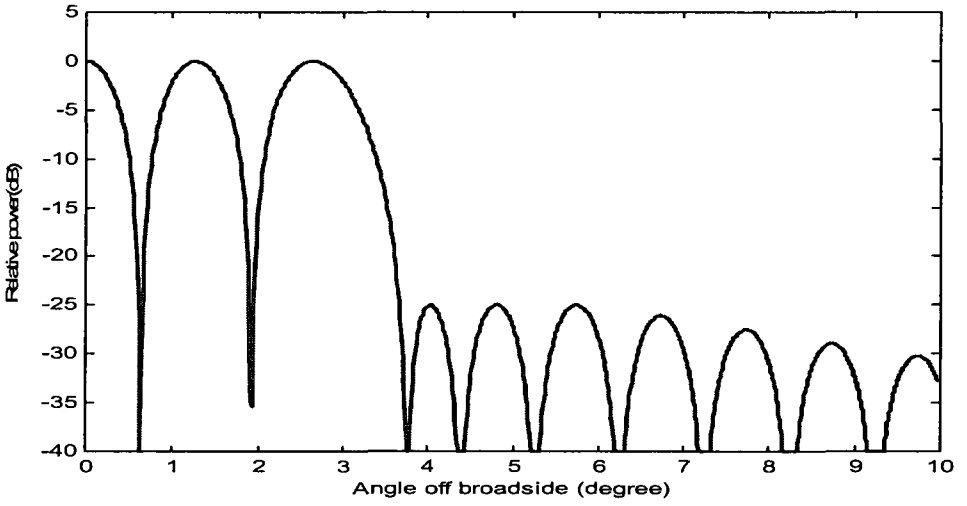

Fig. 4.6-5 : Shaped Pattern with Nulls

Table 4.6-2: Desired Values, Starting Pattern Peak Values And Peak Locations

Number of peak n	γ_{1n}	*Peak locations* Up	*Starting peak values* G	*Desired peak values* S	*Adjusted peak values* S_m	*Real Root values for the pattern in Fig.4.6-5*	*Complex roots*	
							u_n	v_n
1	1.2197	1.635	-17.57	0	0	1.3156	0.5922	0.5402
2	2.2331	2.679	-23.81	0	2	2.7673	1.7442	0.5240
3	3.2383	3.699	-27.957	-25	-35	4.3429	3.6537	0
4	4.2411	4.710	-31.082	-25	-35	5.0023	4.3221	0
5	5.2427	5.517	-33.595	-25	-35	5.8205	5.2229	0

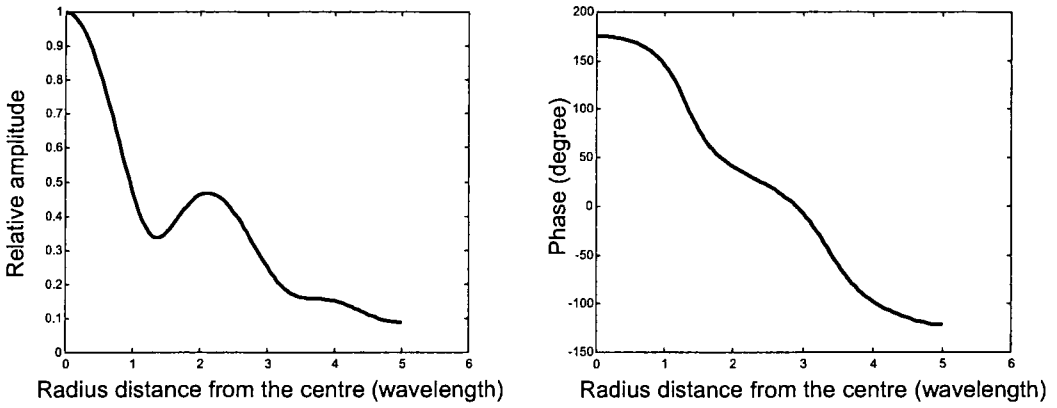

Fig. 4.6-6 : Continuous Aperture Distribution for Flat-Topped Beam

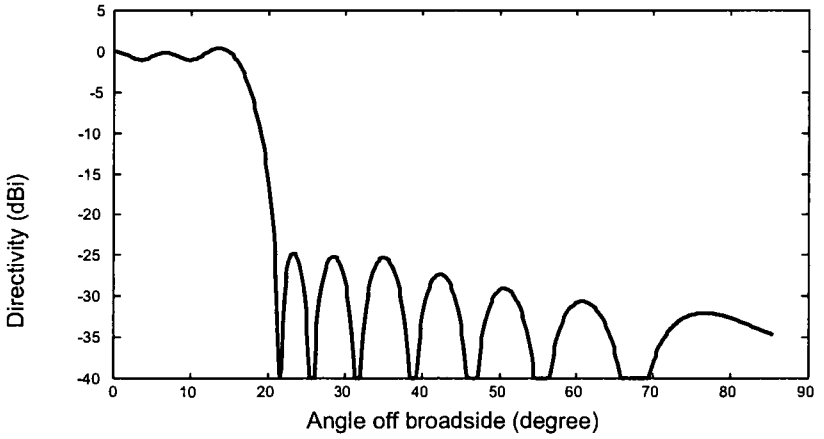

Fig.4.6-7 : Array factor pattern with continuous aperture distribution

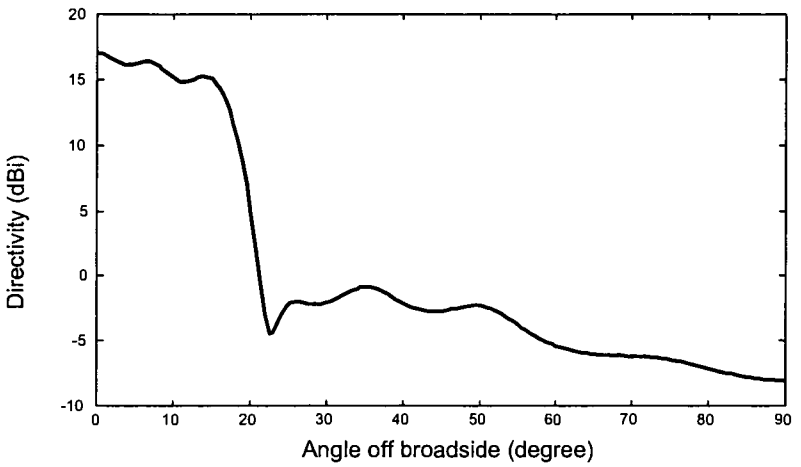

Fig.4.6-8 : Array Factor Pattern After Sampling with 9 Circles

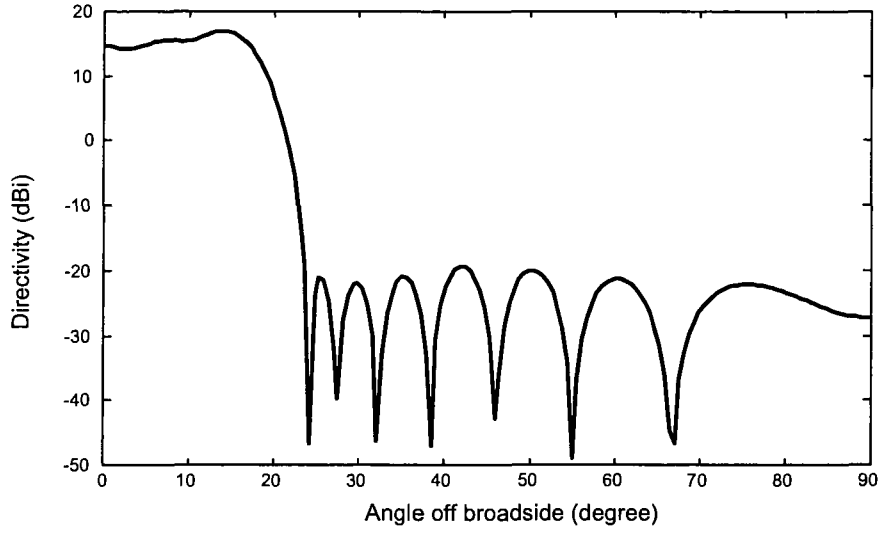

Fig.4.6-9 : Array Factor Pattern with Modified Desired Values and Continuous Aperture Distribution

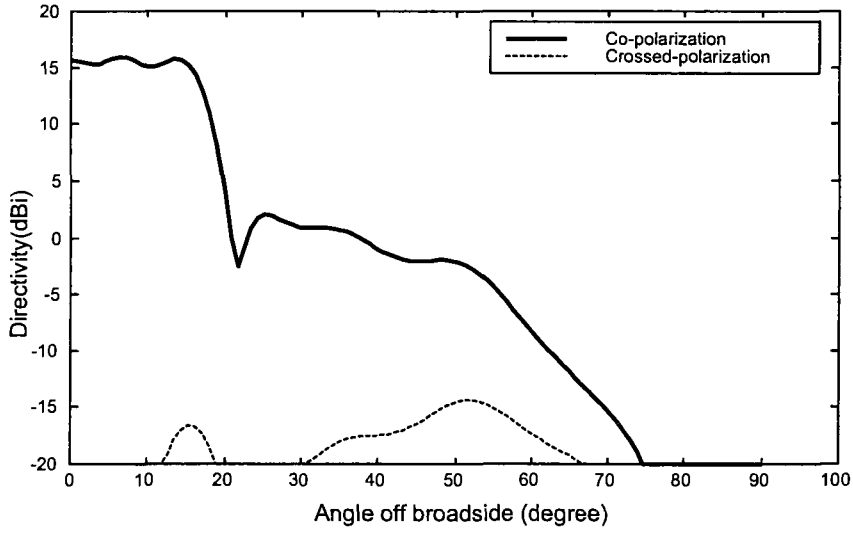

Fig.4.6-10 : Directivity Pattern of Flat-Topped Pattern

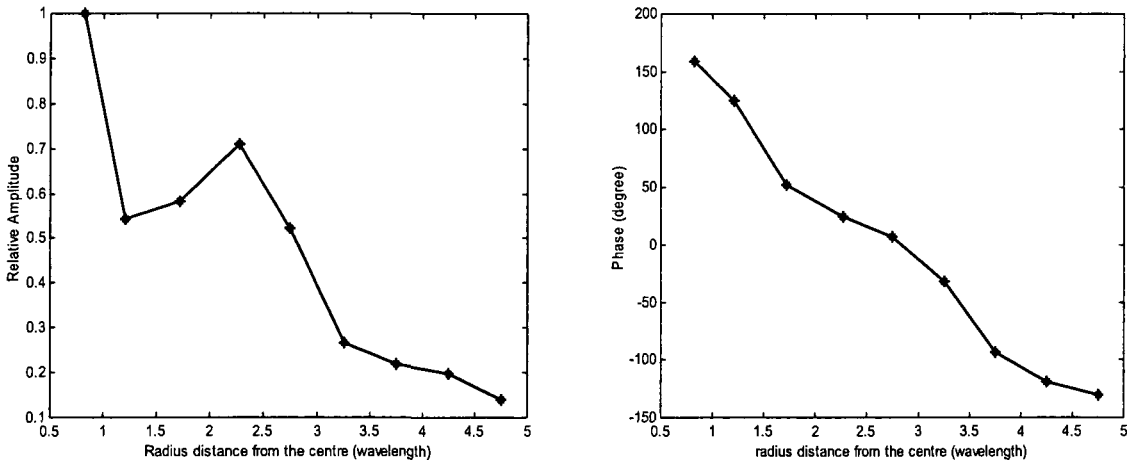

Fig. 4.6-11 : Optimized Aperture Distribution of Flat-Topped Pattern

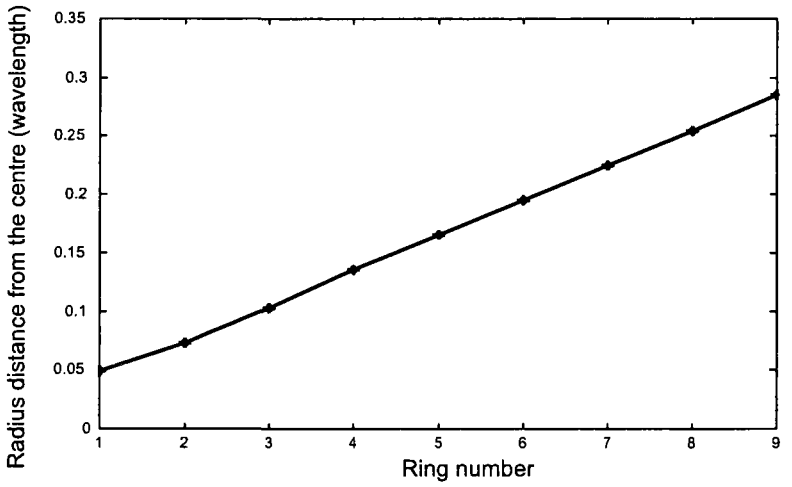

Fig.4.6-12 : Optimized Slot Pair Radius Locations of RLSA Antenna with Flat-Topped Pattern

4.7 CONCLUSIONS

In this chapter we have developed a hybrid synthesis technique that is suited to the RLSA antenna that has non-uniformly spaced, and differently oriented, radiating elements. No pattern synthesis method has yet been provided in the literature for such a situation. The synthesis

technique consists of four steps. In the *first step* the method of Elliott & Stern [1] is used to synthesize a continuous distribution for a circular aperture that provides a radiation pattern that closely approximates the desired pattern. This also enables us to determine the minimum aperture size that is required to obtain the desired radiation pattern. The *second step* uses sampling to obtain an array of discrete isotropic radiating elements located on a radial grid (that is, elements located on a set of concentric circles or rings). It selects the number of rings by examining the resulting radiation pattern. In the *third step* the ring radii and the radiating element excitations are iteratively altered through repeated use of a least-squares optimisation algorithm (which attempts to minimise the averaged difference between the actual and desired patterns) to obtain an improved pattern for the discrete array. In the *fourth step* the slot-pair patterns are included to obtain the full vector radiation patterns of the associated RLSA antenna, which is then used as a guide for the repeated application of certain sub-steps in order to arrive at a radiation pattern that is a sufficiently close approximation to the desired ideal pattern.

The method was illustrated through its application to the synthesis of a specific isoflux pattern problem. This was followed by application of the synthesis technique to the case of a high-directivity pattern with sidelobe control, and to the case of a flat-topped beam antenna.

4.8 REFERENCES FOR CHAPTER 4

[1] R.S. Eilliott and G.J. Stern, "Shaped patterns from a continuous planar aperture distribution", IEE Proceedings, Vol.135, Pt.H, No. 6, Dec.1988.

[2] R. S. Elliott, *Antenna Theory and Design* (Prentice-Hall, 1981).

[3] S. G. Hay, D. G. Bateman, T. S. Bird and F. R. Cooray, "Simple Ka-band earth-coverage antennas for LEO satellites", *IEEE AP-S Int. Symp. Digest,* vol.1, pp. 708-711, 1999.

[4] M. Takahashi, Y. Nakagawa and M. Abe, "Low sidelobes for radial line slot antennas", *Electron. and Commun. in Japan,* part 1, vol. 80, no. 7, pp. 70-76, 1997.

CHAPTER 5

Radial Line Slot Antennas with Isoflux Radiation Patterns

5.1 INTRODUCTION

We pointed out in Chapter 1 that the RLSA antenna has low losses, a relatively simple structure that has a low profile, and can be easily configured to produce circular polarization. It is thus an attractive candidate as an isoflux TT&C antenna for satellite applications. As far as we were able to establish, an effective pattern synthesis technique was not available for RLSA antennas. Such a method was therefore developed in Chapter 4, and illustrated for three different examples : an isoflux radiation pattern, a flat-topped pattern and a high directivity sidelobe-constrained pattern. In Section 5.2 through Section 5.4 we now apply the synthesis method of Chapter 4 to three additional isoflux antennas in order to determine what is achievable; we use an operating frequency of 5 GHz for all three cases. This will allow us, in Section 5.5, to establish what minimum radius is required for an isoflux RLSA antenna with a particular EOC angle. Section 5.6 concludes the chapter.

\

5.2 ISOFLUX RADIATION PATTERN WITH AN EOC ANGLE OF 30°

In this example the aperture radius is 7.66λ and the EOC angle is 30°. The desired pattern obtained from the considerations in Section 1.1 is shown in Fig. 5.2-1

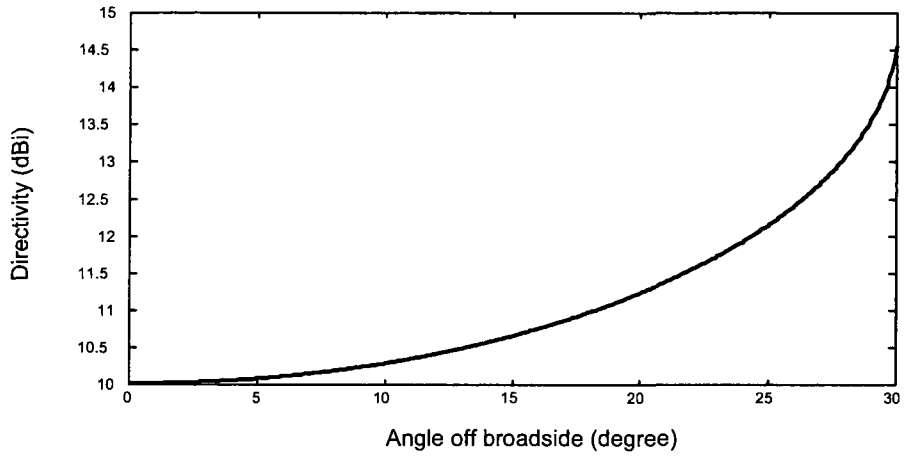

Fig.5.2-1 : Desired Pattern for Isoflux Antenna with EOC of 30°

The complex roots values found from Step#1 are given in Table 5.2-1. The resulting continuous aperture distribution is shown in Fig.5.2-2, the pattern assuming isotropic elements is given in Fig.5.2-3. Using the sampling procedure of Step#2 we determine that we need 15 rings of elements over the aperture, taking account of the fact that there is a central blockage region with $r_c = 0.24\ \lambda$, as discussed in Section 4.3.2. The adjusted aperture distribution and element locations obtained from Step#3 are given in Table 5.2-2 and plotted in Fig. 5.2-4 and Fig. 5.2-5, respectively. The final vector radiation pattern of the RLSA antenna is given in Fig.5.2-6. The pattern is lower than the desired one because there is some energy radiated outside of the FOV. if we choose more peaks to control the sidelobe level outside FOV in Step#1, or increase the aperture radius, the directivity will be increased.

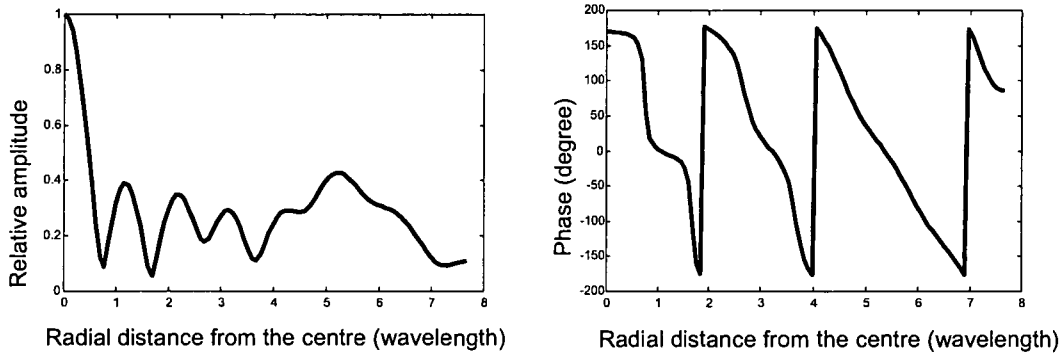

Fig. 5.2-2 : Continuous Aperture Distribution for Isoflux Pattern (EOC Angle 30°)

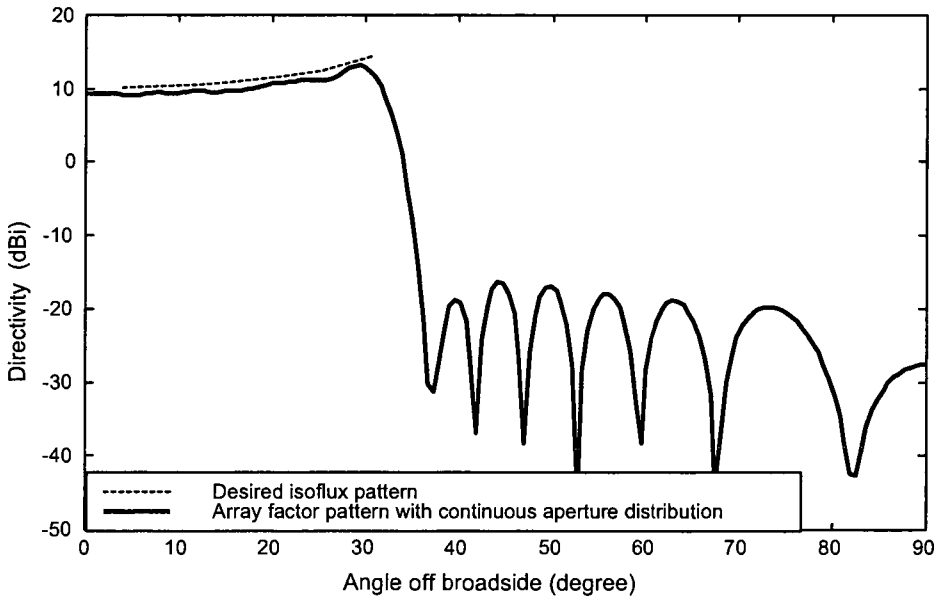

Fig 5.2-3 : Array Factor Pattern of Continuous Aperture Distribution with Radius of 7.66λ and EOC of 30°

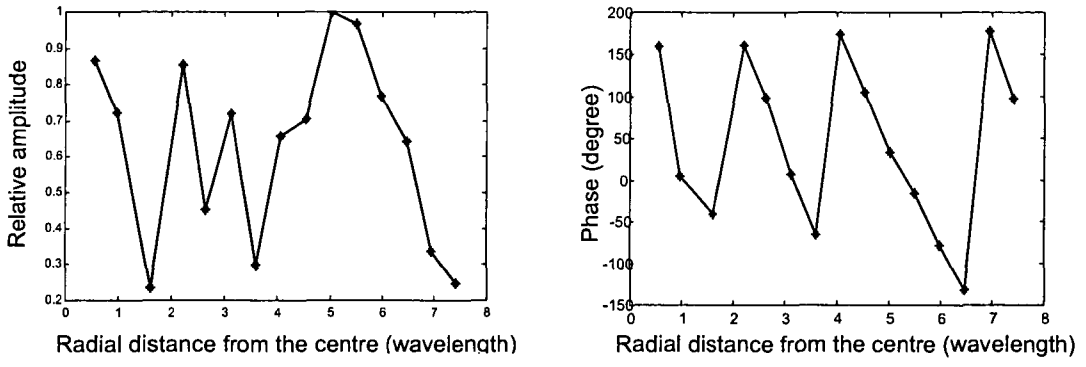

Fig.5.2-4 : Optimized Ring Excitation Amplitudes and Phases of RLSA Antenna

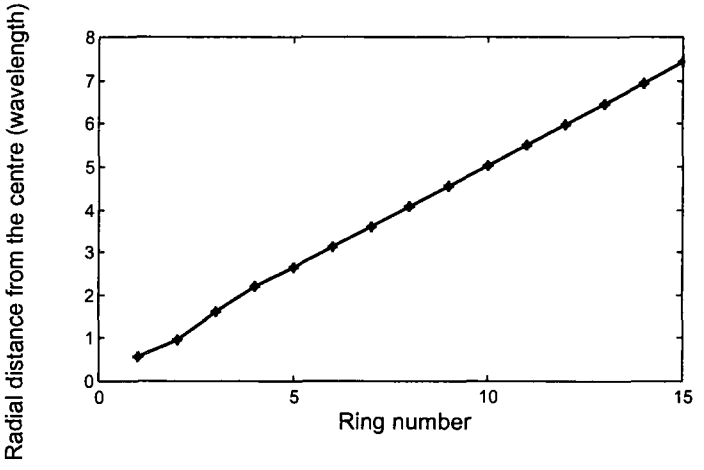

Fig.5.2-5 Optimized Ring Radii

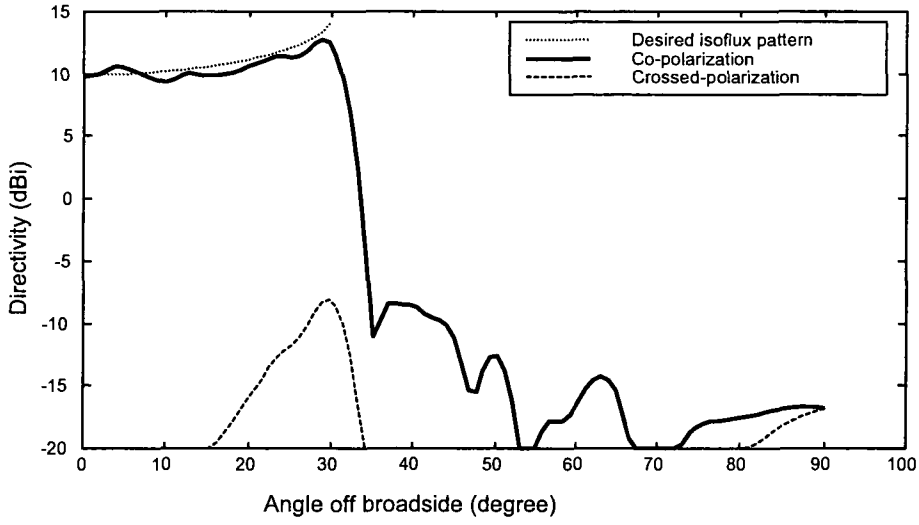

Fig.5.2-6 : Directivity Pattern of RLSA Antenna with 7.66 λ and EOC of 30°

Table 5.2-1 : Complex Roots for Desired Pattern

Root number (n)	u_n	v_n
1	0.5226	0.7942
2	1.5718	0.7934
3	2.6349	0.8030
4	3.6942	0.8592
5	4.6106	0.8492
6	5.6423	0.8096
7	6.7315	0.6164
8	9.2788	0
9	9.1715	0

Table 5.2-2 : Optimized Ring Radii and Excitations

Number of ring	*Radius of ring (wavelength)*	*Excitation of ring*	
		Phase	Amplitude
1	0.5536	159.4482	0.8667
2	0.9575	4.8274	0.7234
3	1.6008	-40.4691	0.2367
4	2.2142	161.1985	0.8551
5	2.6331	97.9967	0.4525
6	3.1119	7.9945	0.7190
7	3.5906	-64.7968	0.2986
8	4.0694	174.2259	0.6586
9	4.5481	105.5752	0.7068
10	5.0269	33.9362	1.0000
11	5.5056	-15.6315	0.9685
12	5.9844	-79.0696	0.7674
13	6.4631	-131.9745	0.6444
14	6.9419	177.5450	0.3354
15	7.4206	96.9467	0.2491

5.3 ISOFLUX RADIATION PATTERN WITH EOC ANGLE OF 60°

We next synthesize an isoflux radiation pattern with an EOC angle of 60 °, whose desired pattern is that in Fig.5.3-1.

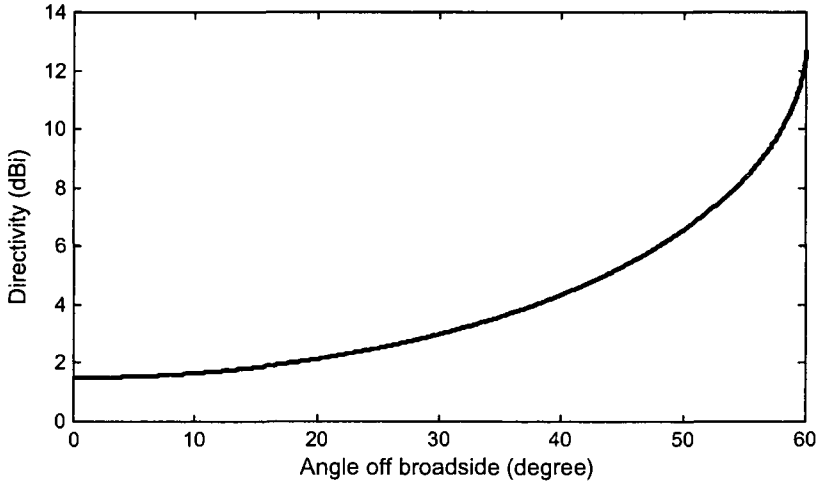

Fig.5.3-1 : Desired Pattern of Antenna for LEO with EOC of 60°

Using considerations similar to that stated in Section 4.2[12], we deduce that the outermost peak of the starting pattern in Step#1 must be located around 68°, there is no peak outside 68°. This at once means we need an aperture radius of 4.15λ or more; we will try to use the smallest radius. When shaping the starting pattern so that it changes into the desired one, all the peak locations will shift to slightly smaller angles, and so after shaping the last peak location will move to around 60 °. Table 5.3-1 shows the required complex root values from Step#1, Fig.5.3-2 shows the associated continuous aperture distribution, and its array factor pattern (that is, assuming isotropic elements) is given Fig.5.3-3. In Step#2 we determined that for proper sampling of the continuous aperture distribution we need M =11. Thus we in fact use 10 circles, the innermost one being eliminated for reasons stated in Section 4.3.2. Application of Step #3 and Step#4 yields the discrete excitation amplitudes and phases provided in Fig.5.3-4 and the ring radii in Fig.5.3-5. The final vector radiation pattern of the RLSA antenna is that in Fig.5.3-6, and Table 5.3-2 lists the optimized element locations and aperture distributions.

From Fig. 5.3.6, we can see, the EOC is indeed around 60°. But the pattern is much lower than the desired one because there is no peak outside FOV in the starting pattern, sidelobes can not be controlled, so more energy radiated outside FOV. We can increase directivity by increasing the aperture radius. More peaks will appear outside FOV for a bigger radius aperture, and these peaks can be used to control the sidelobe level.

[12] For the isoflux pattern synthesis done in that section in order to expand the details of the synthesis approach.

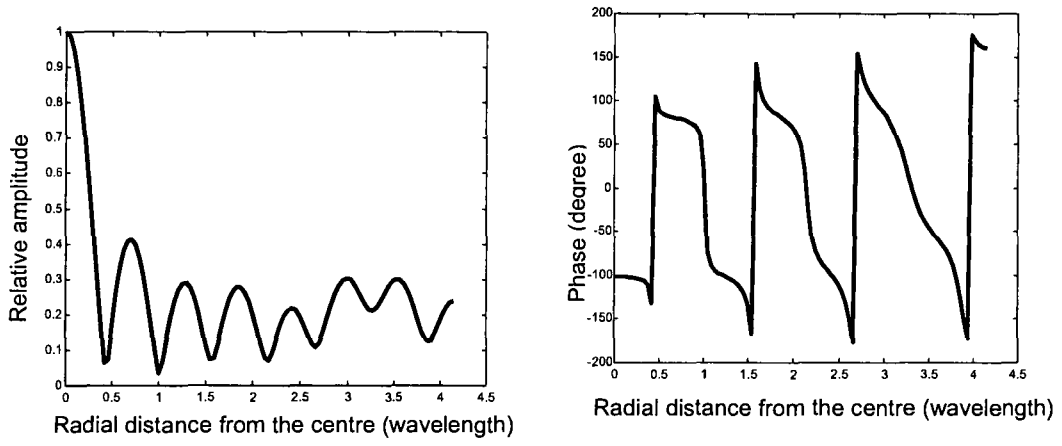

Fig.5.3-2 : Continuous Aperture Distribution with Radius of 4.15 λ and EOC Angle of 60°

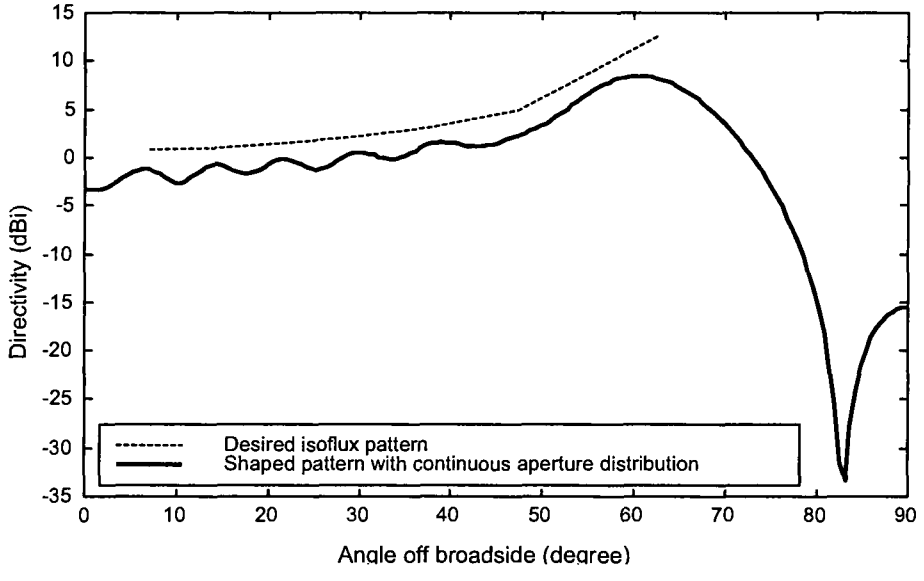

Fig 5.3-3 : Array Factor Pattern of Continuous Aperture Distribution with Radius of 4.15 λ and EOC of 60°

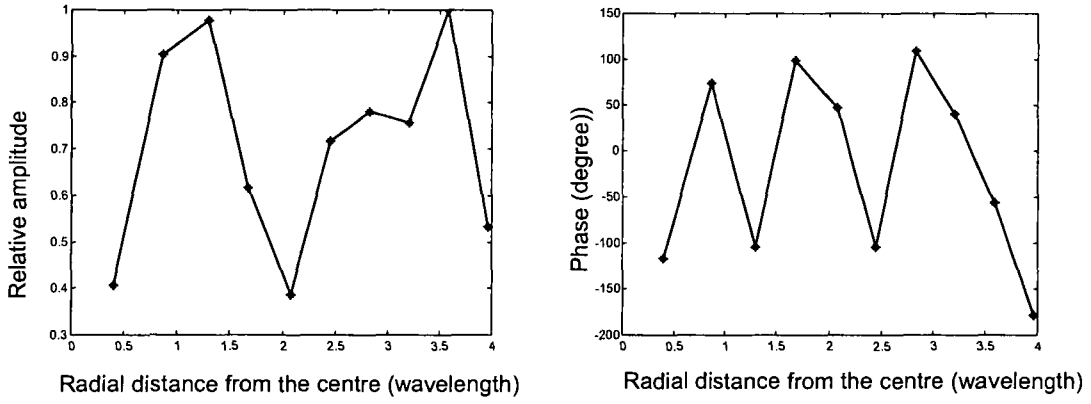

Fig.5.3-4 : Optimized Ring Excitation Amplitudes and Phases of RLSA Antenna

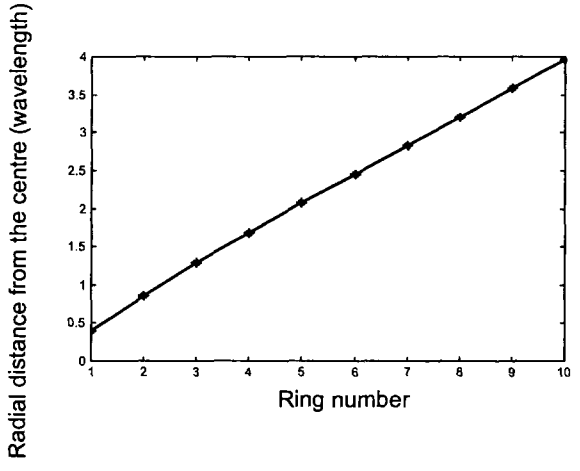

Fig.5.3-5 : Optimized Slot Pair Radius Locations of RLSA Antenna with EOC of 60°

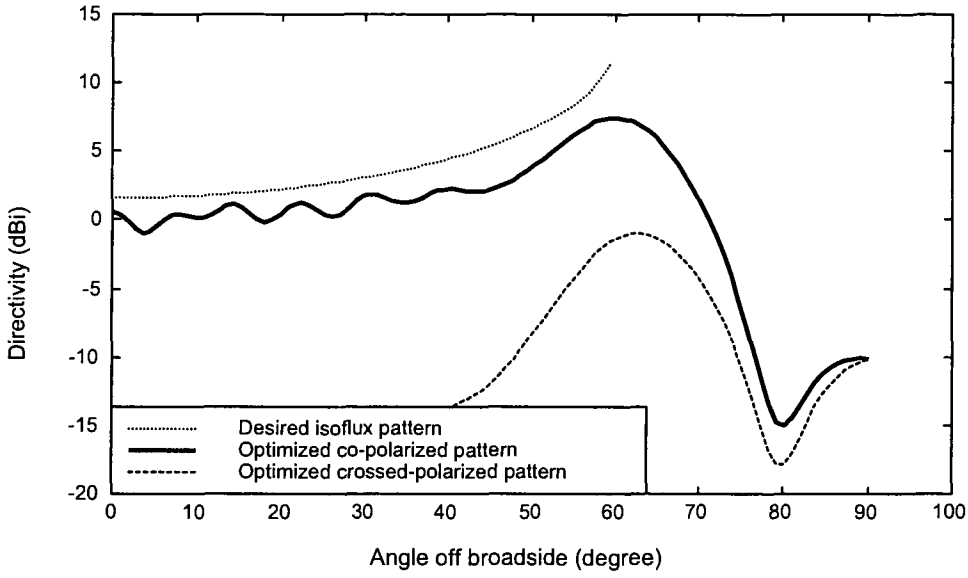

Fig.5.3-6 Directivity Pattern of the RLSA with Radius of 4.15λ and EOC Angle of 60°

Table 5.3-1 : Complex Roots for Desired Pattern

Root number (n)	u_n	υ_n
1	0.5006	0.5137
2	1.5265	0.4884
3	2.5480	0.5126
4	3.5724	0.4892
5	4.6135	0.5145
6	5.6566	0.5881
7	6.3877	0.5493

Table 5.3-2 : Optimized Ring Radii and Excitations

Number of ring	*Radius of ring (wavelength)*	*Excitation of ring*	
		Phase	Amplitude
1	0.3950	-116.4095	0.4063
2	0.8607	74.4791	0.9038
3	1.2910	-104.0970	0.9777
4	1.6741	98.8349	0.6157
5	2.0750	47.6562	0.3854
6	2.4523	-104.4621	0.7161
7	2.8295	109.4121	0.7805
8	3.2068	40.0531	0.7549
9	3.5841	-56.3314	1.0000
10	3.9614	-177.9337	0.5324

5.4 ISOFLUX RADIATION PATTERN WITH EOC ANGLE OF 65°

We finally synthesize an isoflux radiation pattern with and EOC angle of 65°, whose ideal shape is that in Fig.5.4-1. This is a relatively "severe" EOC angle.

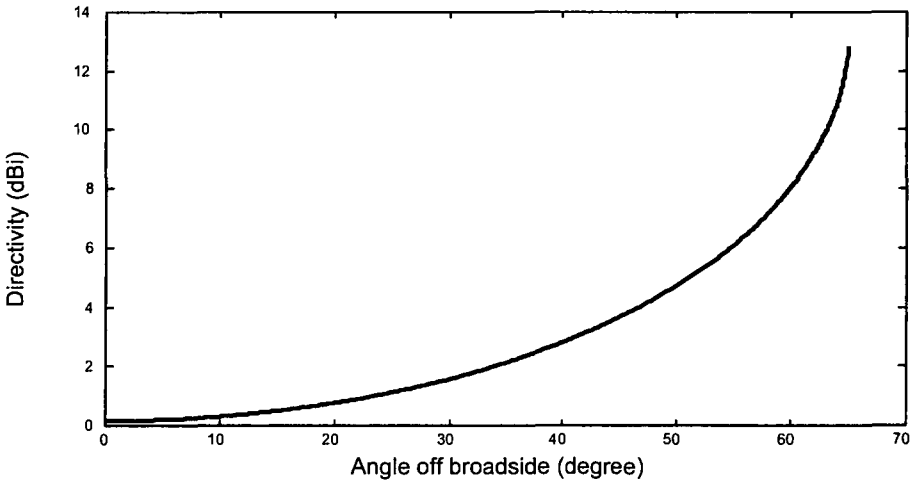

Fig.5.4-1 : Desired Isoflux Radiation Pattern with an EOC Angle of 65°

Examination of the starting pattern in Step#1 reveals that the location of the outermost peak location for the starting pattern must be at about 70.47°; this means that the minimum aperture radius is 5.65λ. After root perturbation the outermost peak location in the FOV shifts inwards to

around 65°. Table 5.4-1 shows the complex root values. Fig.5.4-2 shows the associated continuous aperture distribution, whose array factor is that in Fig.5.4-3. The sampling process of Step#2 directs that 12 rings of elements should be used over the aperture. Fig.5.4-4 plots the ring excitation amplitudes and phases, while Fig.5.4-5 does the same for the ring radii. The final vector radiation patterns of the RLSA antenna is given in Fig.5.4-6. The data for the above figures is listed in Table 5.4-2. The plot in Fig.5.4-6 in fact shows a mask that was provided to us by a supplier of isoflux antennas for small scientific satellites. It is clear that the RLSA antenna pattern moves significantly outside the mask for angles larger than about 40°. However, if we increase the aperture radius to 15λ and repeat the synthesis procedure we obtain the continuous distribution results shown in Fig.5.4-7 and Fig.5.4-8. Proceeding with the sampling of Step#2 we find that 29 rings of elements are required. Fig. 5.4-9 and Fig.5.4-10 gives the optimized ring radii and excitations for the discrete distribution of the RLSA antenna, whose vector radiation patterns are shown in Fig.5.4-11. It is clear that use of a larger aperture allows the designer to more closely match the desired isoflux pattern (and even allows control of the pattern fall-off rate beyond the FOV). The reason is that the larger aperture has more complex zeros (*viz.* degrees of freedom) that can be used in the shaping process.

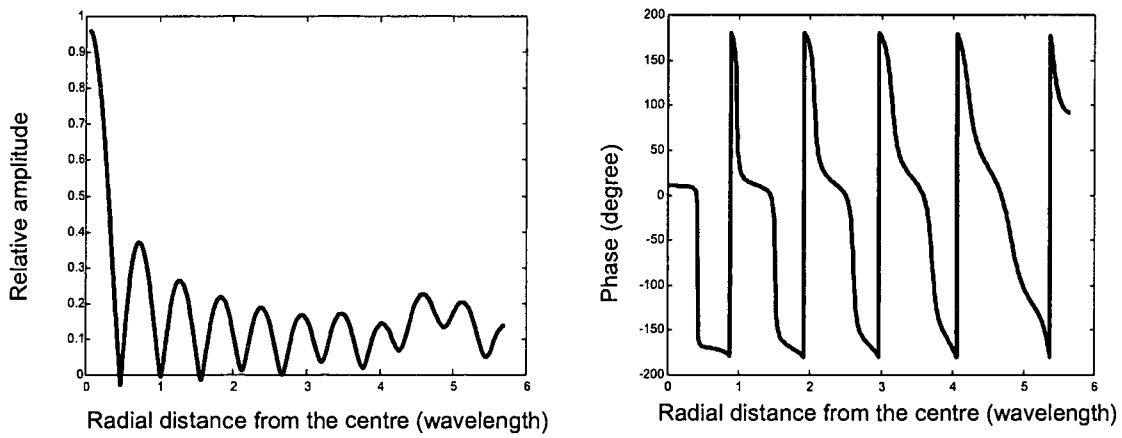

Fig.5.4-2 : Continuous Aperture Distribution with Radius of 5.65 λ and EOC Angle of 65°

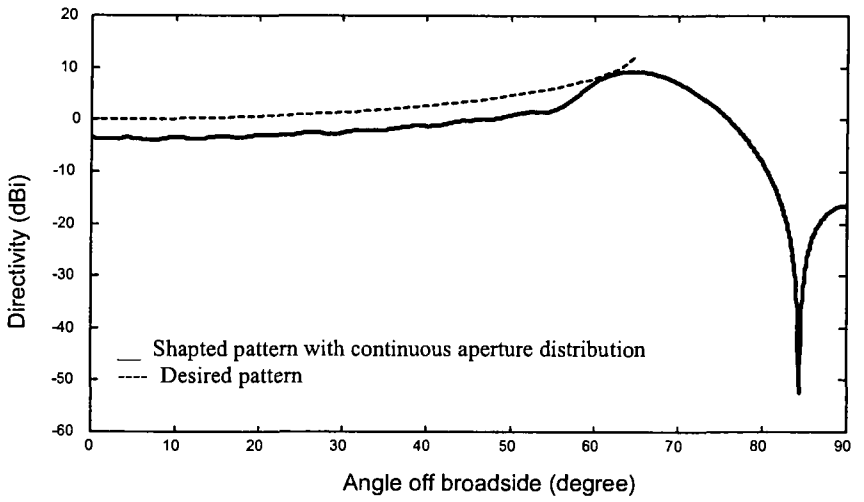

Fig 5.4-3 : Array Factor of Continuous Aperture Distribution with Radius of 5.65 λ and EOC Angle of 65°

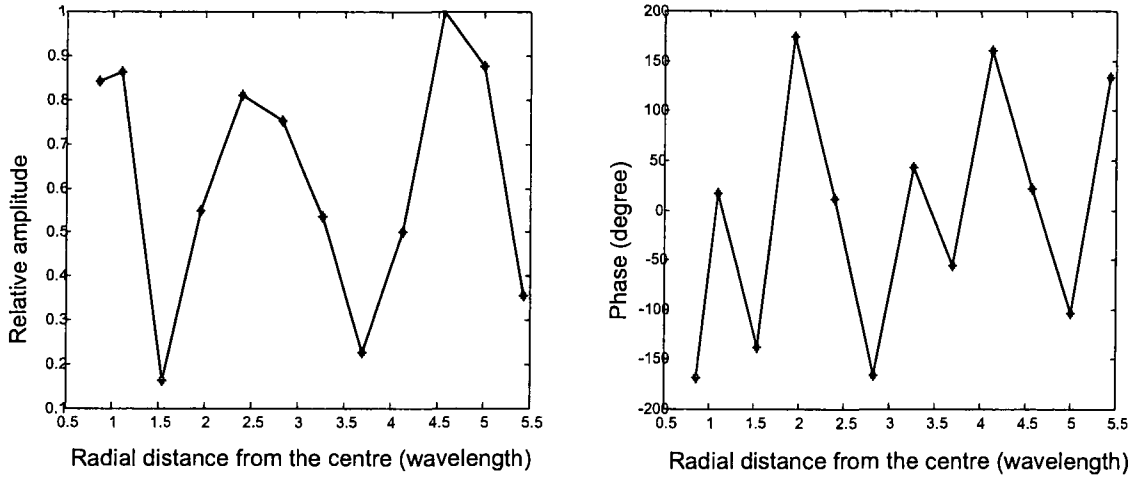

Fig.5.4-4 : Optimized Ring Radii and Excitations of the RLSA Antenna with Radius 5.65 λ and EOC Angle of 65°

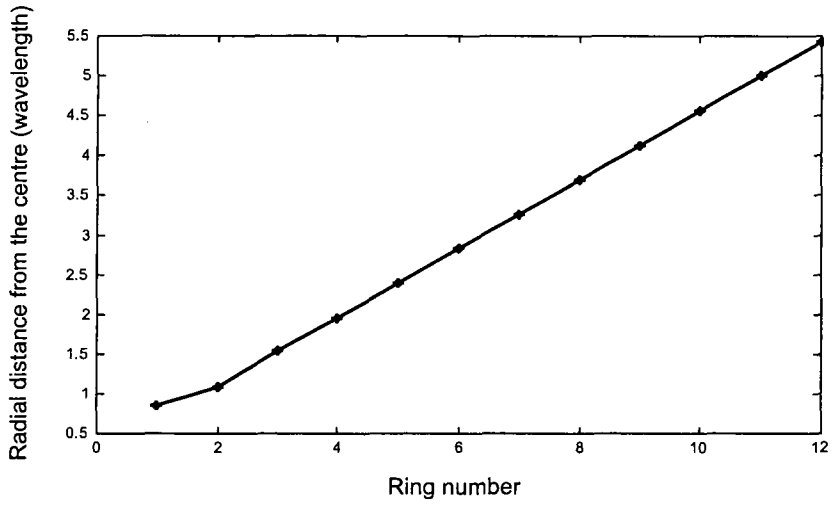

Fig.5.4-5 : Optimized Ring Radii Locations of the RLSA Antenna with 5.65 λ and EOC Angle of 65°

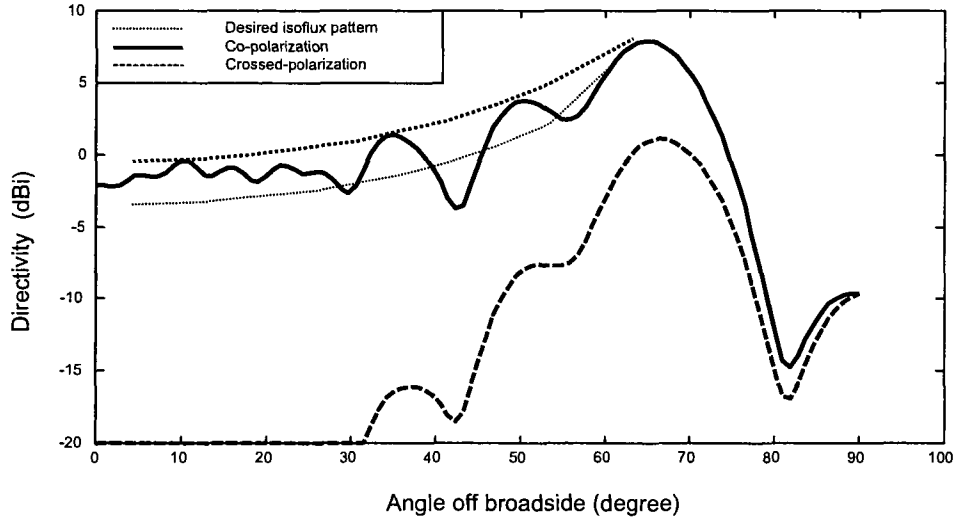

Fig.5.4-6 : Directivity Patterns of the RLSA Antenna with a Radius of 5.65 λ and EOC Angle of 65°

Table 5.4-1 : Complex Roots for Desired Pattern

Root number (n)	u_n	v_n
1	0.4754	0.6845
2	1.4715	0.6317
3	2.4950	0.6329
4	3.4826	0.6466
5	4.4722	0.6347
6	5.4782	0.6086
7	6.4697	0.6186
8	7.4409	0.5953
9	8.4040	0.5590
10	9.3232	0.4018

Table 5.4-2 : Optimized Ring Radii and Excitations

Number of ring	*Radius of ring (wavelength)*	*Excitation of ring*	
		Phase	*Amplitude*
1	0.8556		0.8419
2	1.0933		0.8635
3	1.5347		0.1632
4	1.9558		0.5488
5	2.3904		0.8095
6	2.8250		0.7532
7	3.2596		0.5352
8	3.6942		0.2262
9	4.1288		0.5018
10	4.5635		1.0000
11	4.9981		0.8768
12	5.4327		0.3556

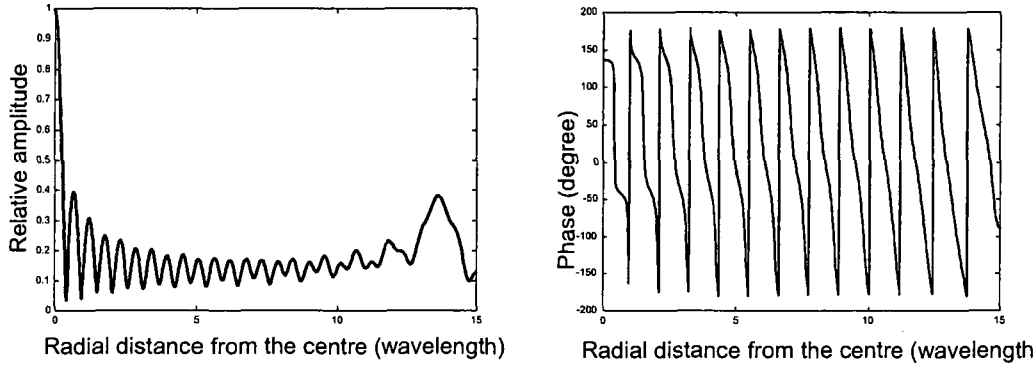

Fig 5.4-7 : Continuous Aperture Distribution with Radius of 15 λ and EOC Angle of 65°

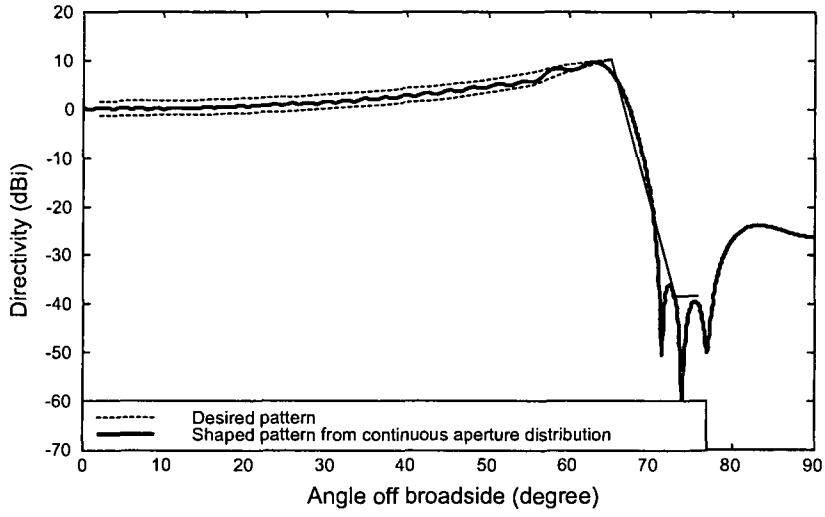

Fig 5.4-8 : Array Factor of Continuous Aperture Distribution with Radius of 15 λ and EOC Angle of 65°

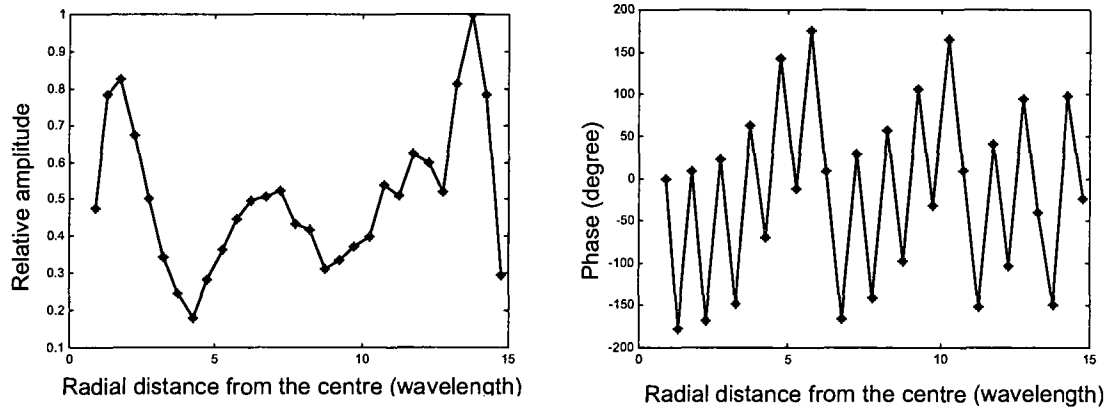

Fig.5.4-9 : Optimized Ring Excitations for RLSA Antenna with Radius 15 λ and EOC Angle of 65°

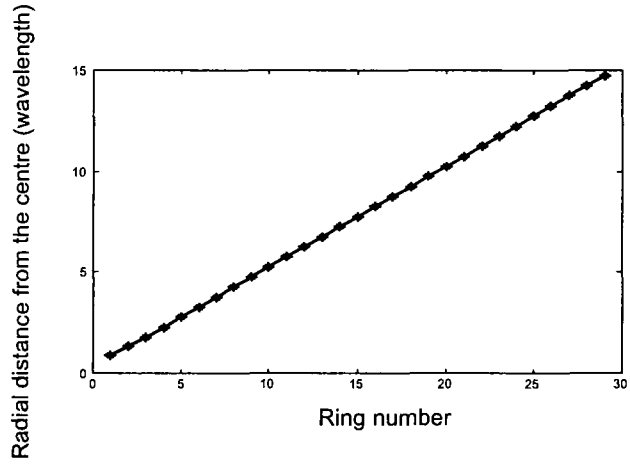

Fig. 5.4-10 : Optimized Ring Radii for RLSA Antenna with Radius 15 λ and EOC Angle of 65°

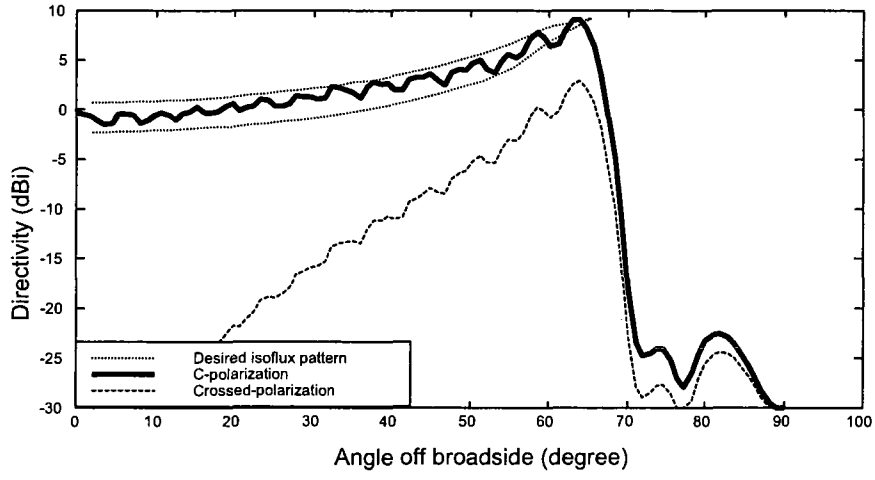

Fig.5.4-11 : Directivity Pattern of RLSA Antenna with Radius 15 λ and EOC Angle of 65°

5.5 MINIMUM APERTURE RADIUS FOR AN ISOFLUX RADIATION PATTERN WITH A SPECIFIC EOC ANGLE

Recall that in Section 5.4 we determined that the smallest aperture radius one could use to obtain an isoflux pattern with an EOC angle of 65° was 5.65λ. This provided the pattern shown in Fig.5.4-6; it is less than ideal but clearly we are able to control the pattern such that the maximum point is at 65°. If we require additional fine control of the pattern within the FOV (while still maintaining the maximum at 65°) we needed to increase the aperture radius above the minimum value, as evidenced in Fig. 5.4-8. Further application of the synthesis procedure to isoflux antennas with other EOC angles enables us to present the plot in Fig. 5.5-1 (whose data is in Table 5.5-1). It gives the minimum aperture radius required for a given EOC angle. This is determined from the continuous aperture distribution, and so will in fact apply to any type of isoflux antenna that has a planar aperture.

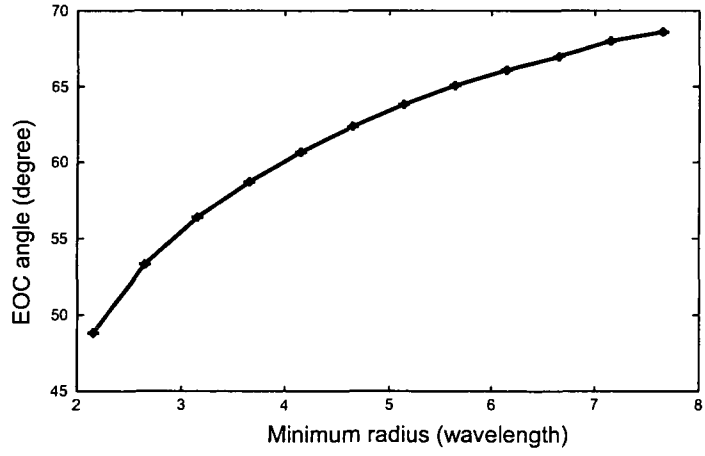

Fig.5.5-1 : EOC Angle versus Minimum Aperture Radius

Table 5.5-1 : EOC Angle Versus Minimum Aperture Radius

EOC angle (degree)	*Minimum aperture radius (λ)*
48.78	2.15
53.28	2.65
56.34	3.15
58.68	3.65
60.66	4.15
62.37	4.65
63.81	5.15
65.07	5.65
66.15	6.15
67.00	6.65
68.04	7.15
68.58	7.65

5.6 CONCLUSIONS

We have applied the synthesis method developed in Chapter 4 to several isoflux antenna pattern examples. In Sections 5.2 through 5.4 we have presented a selection of these to show the effectiveness of the procedure, and have discovered that how close one can shape the RLSA antenna pattern to the desired pattern both inside and outside the FOV depends on the aperture radius of the antenna. Reasons for this have been provided. This enabled us, in Section 5.5, to provide some general data on the minimum radius required for an RLSA antenna with an isoflux pattern as a function of the particular EOC angle.

CHAPTER 6

General Conclusions

The principal contributions of this thesis are as follows:

- We have developed a hybrid synthesis technique that is suited to the RLSA antenna that has differently oriented radiating elements located on irregularly-spaced rings. No effective pattern synthesis method has yet been provided in the literature for RLSA antennas. Although "brute force" pattern synthesis methods can always be used (that is, come up with some objective function and use a general optimization algorithm to minimize it), it is widely commented on in the antenna literature that such an approach is undesirable. The reason is that one is never sure if the best (truly optimal) pattern has in fact been obtained; and when the desired pattern is not achieved the method does not allow a designer to determine why this is so. The synthesis approach developed in this thesis provides the designer with a physical understanding *en route*. This enabled us in Section 5.5, for instance, to state in general terms what the limitations are on the minimum radius of a given isoflux antenna.

- We have devised a low profile isoflux antenna that overcomes the coverage restrictions of other antennas used for such purposes. In other words, we have demonstrated that the RLSA configuration is a candidate for such an antenna, at least from the point of view that it is low-profile and is able to achieve a close-to-ideal isoflux pattern. The fact that

such an antenna can be made entirely of metal makes it attractive in space applications, where such antennas are used for TT&C antennas, and as high speed downlink antennas on small scientific satellites. It was also demonstrated that an RLSA antenna for large EOC angles may require a radius of as much as 15λ ; this may be unacceptably large at the lower microwave frequencies. However, we showed that this limitation applies to any low-profile planar aperture type isoflux antenna.

- As part of the synthesis procedure we required detailed expressions for the far-zone fields of a complete RLSA antenna. In order to achieve this we derived general expressions for the radiation patterns of slot-pairs of arbitrary orientation. We thereafter showed how, since each slot-pair has the same orientation with respect to the radial line on which it lies, it is possible to write an expression for the pattern of the complete RLSA antenna as the product of an (albeit unconventional) array factor and a reference slot-pair pattern.

- Although not a key contribution we have presented a quantitative analysis which clearly demonstrates what the fields inside the radial waveguide are for both non-rotating and rotating modes. While perhaps not new, such a concise explanation does not appear to be available elsewhere in the literature.